

MODELING AND CONTROL OF PRE-CHAMBER INITIATED TURBULENT JET
IGNITION COMBUSTION SYSTEMS

By

Ruitao Song

A DISSERTATION

Submitted to
Michigan State University
in partial fulfillment of the requirements
for the degree of

Mechanical Engineering – Doctor of Philosophy

2018

ABSTRACT

MODELING AND CONTROL OF PRE-CHAMBER INITIATED TURBULENT JET IGNITION COMBUSTION SYSTEMS

By

Ruitao Song

Turbulent jet ignition (TJI) combustion is a promising concept for achieving high thermal efficiency and low NO_x (nitrogen oxides) emissions. A control-oriented TJI combustion model with satisfactory accuracy and low computational effort is usually a necessity for optimizing the TJI combustion system and developing the associated model-based TJI control strategies. A control-oriented TJI combustion model was first developed for a rapid compression machine (RCM) configured for TJI combustion. A one-zone gas exchange model is developed to simulate the gas exchange process in both pre- and main-combustion chambers. The combustion process is modeled by a two-zone combustion model, where the ratio of the burned and unburned gases flowing between the two combustion chambers is variable. To simulate the influence of the turbulent jets to the rate of combustion in the main-combustion chamber, a new parameter-varying Wiebe function is proposed and used for mass fraction burned (MFB) calculation in the main-combustion chamber. The developed model is calibrated using the Least-Squares fitting and optimization procedure.

The RCM model was then extended to a TJI engine model. The combustion process is modeled by a similar two-zone combustion model based on the newly proposed parameter-varying Wiebe function. The gas exchange process is simulated by one-zone model considering piston movement and intake and exhaust processes. Since the engine uses liquid fuel, a pre-chamber air-fuel mixing and vaporization model is developed. And correspondingly, the pre-chamber uses a chemical kinetics based model for combustion rate calculation. The model was validated using the experimental data from a single cylinder TJI engine under different operational conditions, and the simulation results show a good agreement with the experimental data.

For control design, a nonlinear state-space engine model with cycle-to-cycle dynamics is developed based on the previous crank-angle-resolved (CAR) TJI engine model. The state-space

model successfully linked the combustion processes in the two chambers using the parameter-varying Wiebe function. The validated CAR model is used to calibrate and validate the state-space engine model. The simulation results of the two engine models show a good agreement with each other. Thereafter, a linear-quadratic tracking controller is developed for combustion phasing control. Simulation results are presented and a baseline controller has been implemented on the research engine.

Combustion phasing control is very important for internal combustion engines to achieve high thermal efficiency with low engine-out emissions. Traditional open-loop map-based control becomes less favorable in terms of calibration effort, robustness to engine aging, and especially control accuracy for TJI engines due to the increased number of control variables over conventional spark-ignition engines. In this research, a model-based feedforward controller is developed for the TJI engine, and a feedback controller is also designed based on the linear quadratic tracking control with output covariance constraint. Since the TJI main-chamber combustion is influenced by the pre-chamber one, the proposed controller optimizes the control variables in both combustion chambers. The proposed feedforward and feedback controllers show significant performance improvement over a group of baseline controllers through a series of dynamometer engine tests.

Copyright by
RUITAO SONG
2018

ACKNOWLEDGEMENTS

This dissertation would not have been possible without the help of so many people. I would like to express my sincere appreciation to those who provided me guidance, support, encouragement, and also brought a lot of fun to my research and life.

I would like to express my deepest gratitude to my advisor, Dr. Guoming Zhu. It is my fortune and great privilege to do my research work under his continued support and excellent guidance. His comprehensive knowledge of control theory and automotive application inspired me to keep pursuing and enriching my knowledge and experience. His systematic guidance encouraged me to improve the way of thinking and exploring. Besides, he also gave me generous encouragement for my future career and life, which is a lifetime of wealth!

I would like to express my appreciation to my committee members: Dr. Harold Schock, Dr. Hassan Khalil, and Dr. Ranjan Mukherjee, for their discussions and insight comments during my dissertation work. Their wonderful graduate courses also provided me valuable knowledge and firm foundation for my research work, and brought me to the world of engine and control.

I would also like to say thanks to the graduate students and research assistants in our lab, who helped me set up the engine bench and run the experiments, even day and night: Kevin Moran, Tom Stuecken, Ravi Teja Vedula, Jie Yang, Tao Zeng, Yifan Men, Yingxu Wang, Chengsheng Miao, Huan Li, Christine Li, Tianyi He, Shen Qu.

Lastly, I am overly grateful for my family's continued support and warm hearted solicitude that makes me full of courage to strive for the future.

TABLE OF CONTENTS

LIST OF TABLES	viii
LIST OF FIGURES	ix
CHAPTER 1 INTRODUCTION	1
1.1 Motivation	1
1.2 Research Overview	3
1.2.1 Modeling of TJI combustion in a rapid compression machine	3
1.2.2 Combustion modeling for the Dual-Mode TJI engine	3
1.2.3 Optimal combustion phasing control for the Dual-Mode TJI engine	4
1.3 Dissertation Contributions	4
CHAPTER 2 MODELING OF TURBULENT JET IGNITION COMBUSTION IN A RAPID COMPRESSION MACHINE	6
2.1 Introduction	6
2.2 System Description	8
2.3 Turbulent Jet Ignition Combustion Model	10
2.3.1 Gas exchange model	10
2.3.2 Two-zone combustion model	12
2.3.3 Mass fraction burned model	16
2.4 Model Calibration	18
2.5 Model Validation and Simulation Results	21
2.6 Conclusion	28
CHAPTER 3 A CONTROL-ORIENTED COMBUSTION MODEL FOR A TURBU- LENT JET IGNITION ENGINE USING LIQUID FUEL	30
3.1 Introduction	30
3.2 TJI Combustion Model Architecture	31
3.2.1 Target engine description	31
3.2.2 Engine events and combustion model architecture	32
3.3 Gas Exchange Model	33
3.4 Fuel Mixing and Vaporization Model	36
3.5 Two-zone Combustion Model	38
3.5.1 Pre-chamber combustion rate calculation	42
3.5.2 Main-chamber combustion rate calculation	43
3.6 Model Calibration and Validation	45
3.7 Conclusions	54
CHAPTER 4 OPTIMAL COMBUSTION PHASING MODELING AND CONTROL OF A TURBULENT JET IGNITION ENGINE	55
4.1 Introduction	55
4.2 Target Engine Description and Specifications	57

4.3	Nonlinear State-Space TJI Engine Model	58
4.3.1	Main-chamber state-space model	58
4.3.2	Pre-chamber state-space model	62
4.3.3	CA50 calculation	65
4.4	Controller Development	66
4.4.1	Feedforward control	67
4.4.2	Output covariance constraint control	69
4.4.3	Baseline controllers	73
4.5	Experimental Validation	74
4.5.1	Model validation	74
4.5.2	Controller validation	76
4.6	Conclusions	80
CHAPTER 5 CONCLUSIONS AND FUTURE WORK		82
5.1	Conclusions	82
5.2	Recommendations for Future Work	83
APPENDICES		85
APPENDIX A	NONLINEAR STATE-SPACE MODEL	86
APPENDIX B	ENGINE MODEL PARAMETERS	88
BIBLIOGRAPHY		89

LIST OF TABLES

Table 2.1: RCM specifications.	8
Table 2.2: Experimental set-up.	19
Table 2.3: Calibration results for cases 1 and 2.	21
Table 2.4: Simulation parameters.	22
Table 2.5: Calibration results for cases 4-6.	28
Table 3.1: TJI Engine Specifications	32
Table 3.2: Calibration Parameters	48
Table 4.1: PI controller parameters	74
Table B.1: Parameters for Combustion Phase Model	88

LIST OF FIGURES

Figure 2.1: Rapid compression machine	6
Figure 2.2: Working process of the RCM	9
Figure 2.3: Two-zone combustion model.	12
Figure 2.4: The value of αb in the two cases.	15
Figure 2.5: Inverse thermodynamic calculation results.	20
Figure 2.6: MFB obtained from inverse thermodynamic calculation and Least-Squares fitting result.	20
Figure 2.7: Experimental and calculated pressure traces for experimental case 1.	23
Figure 2.8: Experimental and calculated pressure traces for experimental case 2.	23
Figure 2.9: Experimental and calculated pressure traces for experimental case 3.	24
Figure 2.10: Experimental and calculated net heat release rates.	25
Figure 2.11: Chemical energy release rate calculation.	25
Figure 2.12: The calculated value of αb during combustion.	26
Figure 2.13: Experimental and calculated pressure traces for experimental case 4.	27
Figure 2.14: Experimental and calculated pressure traces for experimental case 5.	27
Figure 2.15: Experimental and calculated pressure traces for experimental case 6.	28
Figure 2.16: Experimental and calculated Burn1050 in the main-combustion chamber.	29
Figure 2.17: Experimental and calculated Burn5090 in the main-combustion chamber.	29
Figure 3.1: TJI engine architecture	31
Figure 3.2: Key events over an engine cycle for TJI engine modeling. IVO: intake valve opening; IVC: intake valve closing; EVO: exhaust valve opening; EVC: exhaust valve closing; SPK: spark timing; and INJ: pre-chamber fuel and air injection.	32

Figure 3.3: Pre-chamber fuel vaporization model.	37
Figure 3.4: Two-zone combustion model. αb : area fraction for burned gas	38
Figure 3.5: The value of αb in the two cases.	41
Figure 3.6: TJI engine at MSU.	46
Figure 3.7: Experiment matrix.	47
Figure 3.8: Pressure traces obtained at 1500 rpm.	49
Figure 3.9: Heat release rates in two chambers.	50
Figure 3.10: The value of αb and other related parameters during simulation.	51
Figure 3.11: Pre-chamber pressure traces and main-chamber heat release rates for different pre-chamber λ	51
Figure 3.12: Main-chamber burn duration with the same main-chamber properties and different pre-chamber λ	52
Figure 3.13: IMEP comparison between simulation and experimental results.	53
Figure 3.14: Spk-CA50 comparison between simulation and experimental results.	53
Figure 3.15: Pre-chamber first peak pressures and their crank positions.	53
Figure 4.1: TJI engine architecture	57
Figure 4.2: State-space TJI engine model architecture.	59
Figure 4.3: Control system architecture.	67
Figure 4.4: Experimental matrix.	75
Figure 4.5: State-space engine model validation.	75
Figure 4.6: Comparison between experimental and calculated CA50 under different operational conditions.	77
Figure 4.7: Comparison between experimental and calculated CA50 when pre-chamber fuel is changed.	77
Figure 4.8: Test bench structure.	78

Figure 4.9: Experimental results with controller on and off.	78
Figure 4.10: Experimental results of OCC and PI controllers.	79
Figure 4.11: Experimental results of OCC controllers with and without using pre-chamber fuel.	80
Figure 4.12: Experimental results of OCC controllers under different conditions.	81
Figure 4.13: Standard deviation of CA50 with different controllers.	81

CHAPTER 1

INTRODUCTION

1.1 Motivation

A major focus in light-duty vehicle development is to improve the thermal efficiency of direct-injection spark ignition (DISI) engines and reduce exhaust emissions using various strategies such as high compression ratio, charge dilution, tumble enhancement, high ignition energy, and late intake valve closure timing (Miller or Atkinson cycles). Most passenger cars utilize less than 10% of their maximum engine power during daily commute, according to [1]. This fact highlights the importance of improving engine part-load efficiency. According to a recent benchmarking study conducted by the US EPA, the current production engines carry a part-load brake thermal efficiency ranging from 30 to 35% [2]. An exception to this range are the Mazda's 2.0L engine that showed a peak brake efficiency of 37% under part-load conditions and Toyota's 1.3L Atkinson cycle engine of compression ratio 13.5 with a brake efficiency of 38%. Reese [3] made a "propulsion system efficiency" analysis based on 2015 US EPA certification data to estimate the net improvements required in the engine, transmission, and driveline efficiencies to meet US 2025 GHG regulations. According to this analysis, a further 30% reduction in fuel consumption is required for gasoline engines if all this improvement is to originate solely from engine development [3, 4]. If a thermal efficiency of 35% is considered as the current industry standard, this analysis would indicate a brake thermal efficiency of 50% ($=35\%/0.7$) to meet the 2025 regulations.

New combustion technologies were proposed and studied during the past few decades. Some of these technologies have already been brought to production, such as engine downsizing [5] and Atkinson cycle based engines for many hybrid electric vehicles. Lean burn technologies, like the homogeneous charge compression ignition (HCCI) combustion [6, 7], also attract significant research interest due to their excellent fuel economy and extremely low emissions. The turbulent jet ignition (TJI) combustion system is another promising combustion technology that has the

potential to be widely used in the next generation IC engines.

HCCI combustion has been widely investigated in past decades, and demonstrated the potential of providing higher fuel thermal efficiency and lower emissions than those of the conventional spark ignition (SI) combustion. The un-throttled HCCI combustion significantly reduces the pumping loss, and the lean HCCI combustion results in relatively low in-cylinder flame temperature and has the advantage of significantly reducing the level of NO_x emissions. However, since the HCCI combustion is not suitable for all engine operational conditions, especially under high load and speed conditions, mode transition between SI for high load and speed operations and HCCI combustion for low or mediate load and speed conditions is required. The combustion mode transition control, along with the combustion phase control, are two of the key challenges for the HCCI combustion technology [7, 8]. Whereas, the TJI combustion is able to cover the entire speed and load range of a typical SI engine and the start of combustion can be easily controlled by adjusting the pre-chamber spark timing in the TJI system. Note that as the engine load increases, the achievable lean limit decreases.

Turbulent jet ignition is a pre-chamber initiated two-chamber combustion system [9]. The TJI system mainly consists of three key components: a small pre-chamber, a multi-orifice nozzle, and a large main chamber. A spark-ignited reactive mixture in the pre-chamber flows through the nozzle orifices and results in multiple, chemically active, turbulent jets that emerge into the main chamber. TJI combustion system is able to greatly reduce the NO_x emissions while maintains a comparatively low HC and CO emissions, especially when the relative air-fuel ratio (AFR), λ , is greater than 1.4. According to the early research[10], stable combustion can be achieved for the TJI system when λ is up to 1.8 with extremely low NO_x emissions. Furthermore, the lean burn TJI combustion has been recorded to have an 18% improvement in fuel consumption, comparing to the conventional stoichiometric SI combustion [11].

The TJI combustion system introduces additional freedoms for combustion control. For instance, pre- and main-chamber AFRs, pre-chamber fuel injection and ignition timing. This makes it difficult to utilize the traditional single variable feedback and look-up table based control, and it

often requires real-time optimization, especially under the transient operations. Therefore, model-based control is required to handle multiple-input and multiple-output TJI combustion system.

1.2 Research Overview

1.2.1 Modeling of TJI combustion in a rapid compression machine

A control-oriented TJI combustion model with satisfactory accuracy and low computational effort is usually a necessity for optimizing the TJI combustion system and developing the associated model-based TJI control strategies. This research presents a control-oriented TJI combustion model developed for a rapid compression machine (RCM) configured for TJI combustion. An one-zone gas exchange model is developed to simulate the gas exchange process in both pre- and main-combustion chambers. The combustion process is modeled by a two-zone combustion model, where the ratio of the burned and unburned gases flowing between the two combustion chambers is variable. To simulate the influence of the turbulent jets to the rate of combustion in the main-combustion chamber, a new parameter-varying Wiebe function is proposed and used for mass fraction burned (MFB) calculation in the main-combustion chamber. The developed model is calibrated using the Least-Squares fitting and optimization procedures. Experimental data sets with different AFR in both combustion chambers and different pre-combustion chamber orifice areas are used to calibrate and validate the model. The simulation results show a good agreement with the experimental data for all the experimental data sets. This indicates that the developed combustion model is accurate for developing and validating TJI combustion control strategies.

1.2.2 Combustion modeling for the Dual-Mode TJI engine

For engines equipped with the turbulent jet ignition (TJI) system, the interaction between the pre- and main-combustion chambers should be considered in the control-oriented model for developing control strategies that optimize the overall thermal efficiency in real-time. Therefore, a two-zone combustion model based on the newly proposed parameter-varying Wiebe function is proposed. Since the engine uses the liquid fuel, a pre-chamber air-fuel mixing and vaporization model is also

developed. The model was validated using the experimental data from a single cylinder TJI engine under different operational conditions, and the simulation results show a good agreement with the experimental data.

1.2.3 Optimal combustion phasing control for the Dual-Mode TJI engine

Combustion phasing control is very important for internal combustion engines to achieve high thermal efficiency with low engine-out emissions. Traditional open-loop map-based control becomes less favorable in terms of calibration effort, robustness to engine aging, and especially control accuracy for turbulent jet ignition (TJI) engines due to the increased number of control variables over conventional spark-ignition engines. In this research, a model-based feedforward controller is developed for a TJI engine. A feedback controller is designed based on the linear quadratic tracking control with output covariance constraint. Since the TJI main-chamber combustion is influenced by the pre-chamber one, the proposed controller optimizes the control variables in both combustion chambers. The proposed feedforward and feedback controllers show a significant performance improvement over a group of baseline controllers through a series of dynamometer engine tests.

1.3 Dissertation Contributions

The dissertation has the following major contributions:

- A newly proposed parameter-varying Wiebe combustion model is used to link the combustion processes in both pre- and main-combustion chambers. The developed model can be calibrated using a simple and systematic calibration procedure based on the experimental data.
- The air-fuel mixture in the two combustion chambers are modeled using two zones (burned and unburned) to simulate the complicated gas exchange process between the two chambers.
- Different from many other TJI engines, liquid gasoline is used as the fuel for both the pre- and main-chambers. Since liquid gasoline is hard to be fully vaporized inside the small

pre-chamber before combustion starts, an air-fuel mixing and fuel vaporization model is proposed for the pre-chamber in this research.

- The development of a state-space TJI engine model for model-based control and design of a combustion phasing controller, consisting of feedforward and feedback control, for the TJI engine based on the unique TJI combustion characteristics.

CHAPTER 2

MODELING OF TURBULENT JET IGNITION COMBUSTION IN A RAPID COMPRESSION MACHINE

2.1 Introduction

The TJI combustion system was proposed almost a century ago. In 1918, Harry R. Ricardo first developed and patented the engine using a TJI system[12]. In 1970s, more research efforts were devoted to the development of new TJI systems. Honda developed the compound vortex controlled combustion (CVCC) system [13] that is considered the most significant development in Ottocycle engines with the TJI system. It was able to meet the 1975 emission standards without a catalytic converter.

A typical TJI system consists of a main-combustion chamber and a small pre-combustion chamber. Its volume is a few percent of that of the main-combustion chamber. The two combustion chambers are connected through a few small orifices. The air-fuel mixture is lean in the main-combustion chamber and relatively rich (or close to stoichiometric) in the pre-combustion chamber to make spark ignition (SI) easy. Consequently, the TJI system usually needs two fuel delivering systems for the two combustion chambers. The combustion process is initiated by a spark inside the pre-combustion chamber. Then, the turbulent jets of the reacting products from the pre-

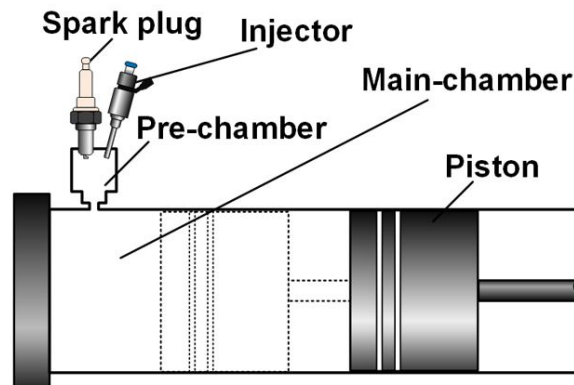


Figure 2.1: Rapid compression machine

combustion chamber flow into the main-combustion chamber and ignite the air-fuel mixture in the main-combustion chamber.

The TJI combustion possesses many advantages over other combustion technologies. One of the approaches to reduce the NO_x (nitrogen oxides) emissions is to operate the engine at very lean conditions with its relative air-to-fuel ratio (AFR) greater than 1 since the resulting relatively low temperature combustion leads to a significant reduction of NO_x formation. Note that significant NO_x emission reduction can only be achieved at the extremely lean condition for conventional SI engines[14]. Extremely lean operation of conventional SI engines will lead to poor combustion stability with high occurrence of misfire due to the narrow fuel flammability limits. Lean mixture also has very slow laminar flame speed that often leads to incomplete combustion. As a result, lean operation in conventional SI engines significantly increases the HC (hydrocarbon) and CO (carbon monoxide) emissions. However, in the TJI combustion system, the mixture in the main-combustion chamber is ignited by the hot turbulent jet that contains much higher energy than what a spark plug can provide[15]. As a result, lean air-fuel mixture can be ignited and burned at a very fast rate with high combustion stability. Therefore, TJI combustion system is able to greatly reduce the NO_x emissions while maintain a comparatively low HC and CO emissions, especially when the relative AFR, λ , is greater than 1.4. According to the previous research, stable combustion can be achieved for the TJI system when λ is up to 1.8[10], approaching elimination of NO_x emissions.

The spark timing, rate of combustion and other combustion parameters in the TJI system need to be optimized by the control strategies to achieve the best fuel efficiency with reduced emissions. To develop and validate the TJI combustion control strategies, a control-oriented TJI combustion model is also required. Toulson [16] modeled a TJI engine using the computational fluid dynamics (CFD) method. Ghorbani [17] modeled a transient turbulent jet by the probability density function (PDF) method. These investigations provide insight to better understand the TJI combustion. However, these models are too detailed to be used for model-based control. Model-based combustion control requires a simple combustion model capable of capturing the TJI system dynamics with good accuracy, low computational and calibration efforts [18].

In this chapter, a control-oriented TJI combustion model is developed for a rapid compression machine (RCM) equipped with a TJI system. The gas exchange process in the combustion chambers before combustion is simulated by a one-zone gas exchange model. It is based on the assumption that the air and fuel are uniformly mixed in both combustion chambers. After ignition, both combustion chambers are divided into burned and unburned zones. The ratio between the burned and unburned gases flowing through the orifices connecting the two combustion chambers are adjusted due to the tiny pre-combustion chamber to improve the model accuracy. To link the two combustion processes in both combustion chambers, a new parameter-varying Wiebe function is proposed and used for the main-combustion chamber mass fraction burned (MFB) calculation. The newly proposed Wiebe function allows the combustion rate in the main-combustion chamber to vary based on the characteristics of turbulent jets from the pre-combustion chamber, which is one of the key features of the TJI combustion.

2.2 System Description

Fig. 2.1 shows the basic architecture of the RCM equipped with a TJI system modeled in this chapter. There is an auxiliary fuel system injecting the methane into the pre-combustion chamber. The two combustion chambers are connected by a small orifice. The detailed parameters of the system are listed in Table 2.1.

Table 2.1: RCM specifications.

Parameter	Value
bore	50.8 <i>mm</i>
stroke	20.2 <i>cm</i>
compression ratio	8.5:1
pre-combustion chamber volume	2.3 <i>cm</i> ³
pre-combustion chamber orifice diameter	1.5-3.0 <i>mm</i>

Here, methane was used as the fuel for all the experiments. Two Kistler piezoelectric pressure sensors were installed into the two combustion chambers for pressure measurements. During the experiment, the combustion chamber wall was heated to 80°C. The combustion chambers were

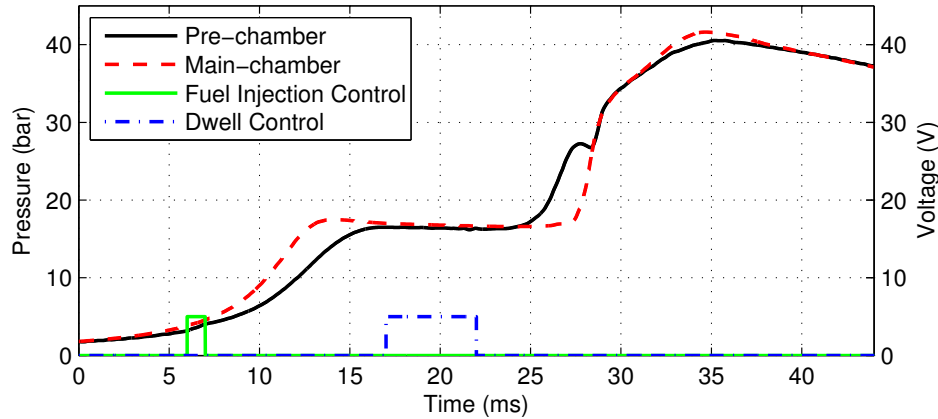


Figure 2.2: Working process of the RCM

firstly evacuated by a vacuum pump and then filled with air-fuel mixture with a known AFR. Then, the piston rapidly compressed the mixture in both combustion chambers. At the same time, a charge of fuel was injected into the pre-combustion chamber; see Fig. 2.2. At the end of compression, the piston kept still; and therefore, the volume in the main-combustion chamber remained constant. At the falling edge of the dwell control signal, the spark is initiated through the spark plug inside the pre-combustion chamber and then the reacting products from the pre-combustion chamber were injected into the main-combustion chamber and ignited the air-fuel mixture. Fig. 2.2 shows the control signals and the typical pressure traces measured during the experiment.

In order to have a good mixing, the fuel was injected during the compression. The fuel flow mixes with the gas flowing through the orifice from the main-combustion chamber during the injection, leading to a better mixing. Moreover, to allow enough time for the mixing process after fuel injection, the injection timing was set at the beginning of the compression. In this way, we are able to make sure that the air-fuel mixture in the pre-combustion chamber is close to uniformly mixed.

2.3 Turbulent Jet Ignition Combustion Model

2.3.1 Gas exchange model

During compression, methane is injected into the pre-combustion chamber. The mass flow rate of the injected methane can be calculated by the one-dimensional compressible flow equation [1].

$$\dot{m}_{inj} = C_{d1} A_{v1} \frac{P_{inj}}{\sqrt{RT_{inj}}} \psi \left(\frac{P_{pre}}{P_{inj}} \right), P_{inj} > P_{pre} \quad (2.1)$$

where

$$\psi(x) = \begin{cases} \sqrt{\kappa \left(\frac{2}{\kappa+1} \right)^{\frac{(\kappa+1)}{(\kappa-1)}}} & x < \left(\frac{2}{\kappa+1} \right)^{\frac{\kappa}{(\kappa-1)}} \\ x^{\frac{1}{\kappa}} \sqrt{\frac{2\kappa}{\kappa-1} \left(1 - x^{\frac{(\kappa-1)}{\kappa}} \right)} & x \geq \left(\frac{2}{\kappa+1} \right)^{\frac{\kappa}{(\kappa-1)}} \end{cases} \quad (2.2)$$

Note that the coefficient C_{d1} is experimentally determined; A_{v1} is the orifice area of the fuel injector; κ is the ratio of specific heats; R is the gas constant; P_{inj} and T_{inj} are the upstream pressure and temperature, respectively; and P_{pre} is the pressure in the pre-combustion chamber.

The gas exchange process between the two combustion chambers is modeled similarly. However, the pressure in the pre-combustion chamber can be either greater or less than that in the main-combustion chamber. The mass flow rate between the two combustion chambers is calculated by the following equation.

$$\dot{m}_{tur} = \begin{cases} C_{d2} A_{v2} \frac{P_{pre}}{\sqrt{RT_{pre}}} \psi \left(\frac{P_{main}}{P_{pre}} \right) & P_{pre} \geq P_{main} \\ -C_{d2} A_{v2} \frac{P_{main}}{\sqrt{RT_{main}}} \psi \left(\frac{P_{pre}}{P_{main}} \right) & P_{pre} < P_{main} \end{cases} \quad (2.3)$$

where C_{d2} and A_{v2} are the discharge coefficient and the area of the orifice connecting the two combustion chambers. The subscripts *pre* and *main* denote the pre-combustion and main-combustion chamber properties, respectively.

Before ignition, the pre-combustion chamber is considered as a control volume with mass and energy exchange. The mass and energy conservation equations are used to describe such a control volume.

$$\begin{aligned}\frac{dm_{pre}}{dt} &= \dot{m}_{inj} - \dot{m}_{tur} \\ \frac{dU_{pre}}{dt} &= \dot{H}_{inj} - \dot{H}_{tur} - \dot{Q}_{ht}\end{aligned}\quad (2.4)$$

where m_{pre} and U_{pre} are the mass and internal energy of the gas in the pre-combustion chamber, respectively; \dot{Q}_{ht} is the heat transfer rate through the chamber wall; and H is the enthalpy flow. The subscript *inj* and *tur* represent the properties of the gas from the fuel injector and through the orifice connecting the two combustion chambers, respectively.

Assuming that the gas can be considered as an ideal gas, the two equations can be coupled by the ideal gas law below.

$$P_{pre} \cdot V_{pre} = m_{pre} \cdot R \cdot T_{pre} \quad (2.5)$$

where V_{pre} is the pre-combustion chamber volume. Substituting Eqn. (2.5) into Eqn. (2.4), the following two equations are obtained to calculate the gas pressure and temperature.

$$\begin{aligned}\frac{dP_{pre}}{dt} &= \frac{R}{V_{pre}c_v} [c_p\dot{m}_{inj}T_{inj} - c_p\dot{m}_{tur}T_{tur} - \dot{Q}_{ht}] \\ \frac{dT_{pre}}{dt} &= \frac{T_{pre}R}{P_{pre}V_{pre}c_v} [c_p\dot{m}_{inj}T_{inj} - c_p\dot{m}_{tur}T_{tur} \\ &\quad - c_v(\dot{m}_{inj} - \dot{m}_{tur})T_{pre} - \dot{Q}_{ht}]\end{aligned}\quad (2.6)$$

where c_p and c_v are the specific heat at constant pressure and constant volume, respectively, and

$$T_{tur} = \begin{cases} T_{pre} & \dot{m}_{tur} > 0 \\ T_{main} & \dot{m}_{tur} \leq 0 \end{cases} \quad (2.7)$$

The pre-combustion chamber volume is only around 2-4% of the main-combustion chamber clearance volume. Therefore, the gas flowing between the two combustion chambers can be

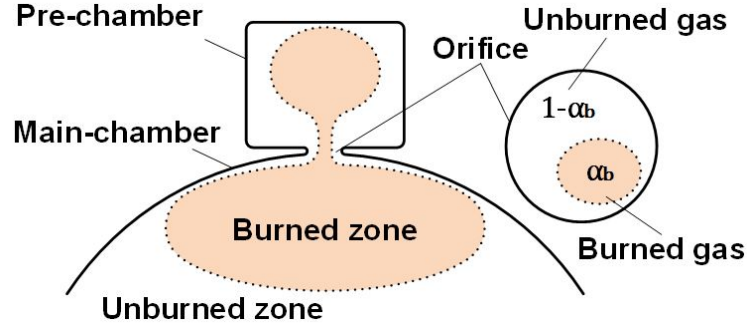


Figure 2.3: Two-zone combustion model.

neglected for the main-combustion chamber model. The pressure and temperature in the main-combustion chamber can be solved using the energy and mass conservation equations. These equations can be found in many other articles about engine modeling[6, 18] and thus will not be shown here.

2.3.2 Two-zone combustion model

After ignition, the pre-combustion chamber is divided into two zones to improve the model accuracy. Both the burned and unburned zones can be regarded as control volumes. Besides the mass, enthalpy, and work exchange between the two control volumes, there are also mass and enthalpy exchange through the orifice to the main-combustion chamber; see Fig. 2.3. The burned and unburned gases in the pre-combustion (or main-combustion) chamber are assumed to enter the burned zone and unburned zone in the main-combustion (or pre-combustion) chamber, respectively. Before the ignition of the main-combustion chamber, all the gas from the main-combustion chamber is considered as unburned gas. The energy balance equation of the burned zone is shown in Eqn. (2.8). To make the equations concise, the variables in the following equations in this subsection are for the pre-combustion chamber, if not specified.

$$\begin{aligned}
 c_v \frac{d(m_b T_b)}{dt} + P \frac{dV_b}{dt} + x_b \dot{Q}_{ht} = \\
 \dot{Q}_{ch} + \frac{m_u}{1-x_b} \frac{dx_b}{dt} c_p T_u - \dot{m}_{tur-b} c_p T_b
 \end{aligned} \tag{2.8}$$

The energy balance equation of the unburned zone is represented by

$$c_v \frac{d(m_u T_u)}{dt} + P \frac{dV_u}{dt} + (1 - x_b) \dot{Q}_{ht} = - \frac{m_u}{1 - x_b} \frac{dx_b}{dt} c_p T_u - \dot{m}_{tur-u} c_p T_u \quad (2.9)$$

The masses of both burned and unburned zones are obtained based on the following mass conservation law.

$$\begin{aligned} \frac{dm_b}{dt} &= -\dot{m}_{tur-b} + \frac{m_u}{1 - x_b} \frac{dx_b}{dt} \\ \frac{dm_u}{dt} &= -\dot{m}_{tur-u} - \frac{m_u}{1 - x_b} \frac{dx_b}{dt} \end{aligned} \quad (2.10)$$

The subscripts b and u represent burned zone and unburned zone. Q_{ht} is the heat transfer to the chamber wall. Q_{ch} is the chemical energy released by combustion. x_b is the MFB. m_{tur-b} and m_{tur-u} represent the burned gas and unburned gas flowing through the orifice. Correspondingly, the area of the orifice is also divided into two parts. One for the burned gas and the other for the unburned gas. Fig. 2.3 shows the basic idea of the two-zone combustion model. When the pressure in the pre-combustion chamber is greater than that in the main-combustion chamber, the two mass flow rates are calculated by

$$\begin{aligned} \dot{m}_{tur-b} &= \alpha_b C_{d2} A_{v2} \frac{P_{pre}}{\sqrt{RT_b}} \psi \left(\frac{P_{main}}{P_{pre}} \right) \\ \dot{m}_{tur-u} &= (1 - \alpha_b) C_{d2} A_{v2} \frac{P_{pre}}{\sqrt{RT_u}} \psi \left(\frac{P_{main}}{P_{pre}} \right) \end{aligned} \quad (2.11)$$

Similar result can be obtained when the pressure in the main-combustion chamber is greater than that in the pre-combustion chamber.

The coefficient α_b in Eqn. (2.11) is chosen as a function of the volume fraction of the burned gas v_b . Assuming that the burned and unburned gases were always well mixed, α_b would be always equal to v_b . However, in reality, this is not the case. α_b is combustion chamber structure dependent. For our TJI system, the spark plug is located at the top of the pre-combustion chamber; see Fig. 1. In this case, the combustion is initiated at the top of the pre-combustion chamber.

Since the orifice is at the bottom, it is hard for the burned gas to escape from the pre-combustion chamber at the early stage of the combustion. As a result, the fraction of the burned gas flowing through the orifice to the main-combustion chamber is much smaller than the burned gas fraction inside the pre-combustion chamber. This is why α_b is smaller than v_b in the pre-combustion chamber when $P_{pre} > P_{main}$. Note that α_b will be determined using experimental data. When $P_{pre} < P_{main}$, the gas in the main-combustion chamber flows through the orifice and α_b will be determined by the burned gas fraction in the main-combustion chamber. Since the combustion in the main-combustion chamber is initiated by the turbulent jet (close to orifice), the orifice is surrounded by the gas with high concentration of burned gas. Therefore, α_b is larger than v_b in the main-combustion chamber. And again, the actual value will be determined by the experimental data. This is the main reason why two-zone combustion model is used. The value of α_b can be expressed by Eqn. (2.12).

$$\alpha_b = \begin{cases} f_1(v_{b-pre}, c_{pre}) & P_{pre} > P_{main} \\ f_2(v_{b-main}, c_{main}) & P_{pre} < P_{main} \end{cases} \quad (2.12)$$

To simplify the calibration process, the two functions, f_1 and f_2 , are approximated by second-degree Bézier curves [19]. Besides the control points (0,0) and (1,1), $(c_{pre}, 1 - c_{pre})$ was added for f_1 and $(c_{main}, 1 - c_{main})$ for f_2 as the third control points; see Fig. 2.4. The parameters c_{pre} and c_{main} are experimentally determined. The Bézier curve guarantees $\alpha_b \in [0, 1]$ as long as $c_{pre} \in [0, 1]$ and $c_{main} \in [0, 1]$. By changing c_{pre} and c_{main} , the ratio of the burned and unburned gases flowing through the orifice can be adjusted to better match the actual physical process and thus to improve the model accuracy.

Applying the principle of mass conservation, the instant fuel mass in the pre-combustion chamber can be obtained by

$$\frac{dm_{pre-fuel}}{dt} = -\frac{m_{pre-fuel}}{1-x_b} \frac{dx_b}{dt} - \dot{m}_{tur-u} \left(\frac{1}{\lambda(A/F)_s + 1} \right) \quad (2.13)$$

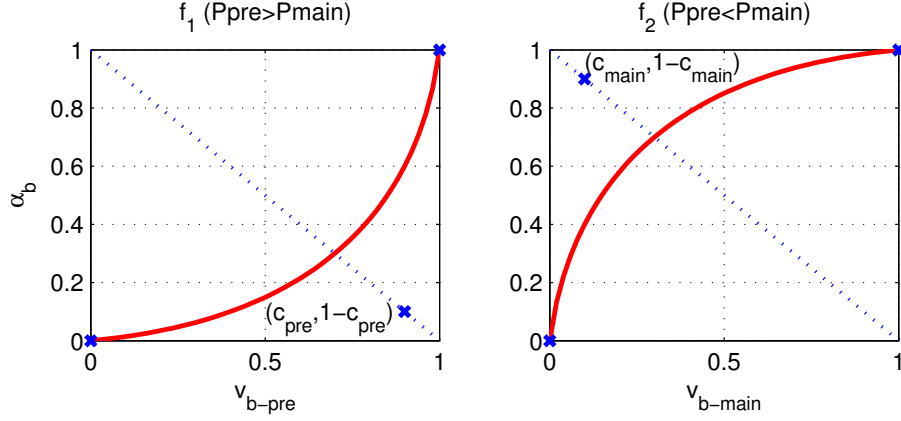


Figure 2.4: The value of α_b in the two cases.

where λ is the relative AFR, and $(A/F)_s$ is the stoichiometric AFR. Note that only the fuel from the unburned zone is considered.

From Eqn. (2.11) and Eqn. (2.13), it can be observed that the total amount of fuel burned inside the pre-combustion chamber is highly influenced by α_b .

The rate of chemical energy release (CER) is obtained by the following relationship.

$$\dot{Q}_{ch} = \eta_{pre} Q_{LHV} \frac{m_{pre-fuel}}{1-x_b} \frac{dx_b}{dt} \quad (2.14)$$

where the combustion efficiency η_{pre} is experimentally determined, and Q_{LHV} is the lower heating value of the fuel.

The rate of heat transfer to the combustion chamber wall can be modeled by the following equation[20].

$$\dot{Q}_{ht} = A_{pre} h_c (T_{pre} - T_w) \quad (2.15)$$

where A_{pre} is the pre-combustion chamber surface area; T_w is the mean wall temperature; and h_c is the heat-transfer coefficient calibrated by the experiment.

After the ignition in the pre-combustion chamber, the combustion in the main-combustion chamber will not be initiated until the generation of the turbulent jet from the pre-combustion chamber. Before the ignition of the main-combustion chamber, the mass flow from the burned

zone of the pre-combustion chamber to the main-combustion chamber is neglected. The amount of the fuel in the main-combustion chamber is calculated by

$$\frac{dm_{main-fuel}}{dt} = \dot{m}_{tur-u} \left(\frac{1}{\lambda_{pre}(A/F)_s + 1} \right) \quad (2.16)$$

where $m_{main-fuel}$ is the fuel mass in the main-combustion chamber.

After ignition in the main-combustion chamber, the burned zone is created. Different from the two-zone combustion model in a conventional SI engine, the combustion model of the main-combustion chamber needs to consider the gas flowing through the orifice into the pre-combustion chamber. The mass and energy conservation equations for burned and unburned zones are very similar to those of the pre-combustion chamber model presented in this subsection and is omitted here. The major difference is that the total volume of the main-combustion chamber is varying.

2.3.3 Mass fraction burned model

The MFB in the pre-combustion chamber is obtained from the Wiebe function [21].

$$x_b = 1 - \exp \left[-a \left(\frac{t - t_{ign}}{\Delta t_d} \right)^{m+1} \right] \quad (2.17)$$

The coefficients, a and m , are chosen to be 6.908 and 2, respectively; t_{ign} is the start of ignition; and Δt_d is the burn duration that is calibrated by AFR before ignition.

At the early stage of the combustion in the main-combustion chamber, the rate of combustion is determined by not only the gas properties in the main-combustion chamber but also the turbulent jet from the pre-combustion chamber. This is due to the fact that the turbulent jets create multiple and distributed ignition sites, which increases the overall flame front area in the main-combustion chamber. Moreover, these turbulent jets increase the turbulence intensity in the main-combustion chamber and thus the flame front propagation speed. After the turbulent jet disappears, the rate of combustion reduces gradually to a relatively low level and its characteristics are mainly determined by the gas properties only in the main-combustion chamber. Here, the term 'intensity' of the turbulent jet is used to describe the resulting increment of the combustion rate in the main-combustion

chamber due to the turbulent jet. Since the intensity of the turbulent jet is determined by the combustion processes in both combustion chambers, estimating the rate of combustion before ignition is difficult and requires significant calibration effort. Therefore, adjusting the rate of combustion according to the turbulent jet intensity during the combustion process is preferred for the TJI combustion model. The conventional single-Wiebe function is not suitable for our combustion model. Multi-Wiebe function is a possible approach for modeling the MFB. However, it requires to determine all associated parameters before ignition occurs. Therefore, a new parameter-varying Wiebe function is proposed and used in this chapter; see Eqn. (2.18).

$$\begin{cases} x'_b(t) = 1 - \exp \left\{ -a \left[\frac{t - t_{ign_b}(t)}{\Delta t_d} \right]^{m+1} \right\} \\ t_{ign_b}(t) = t_0 - \int_{t_0}^t [b(t) - 1] dt \end{cases} \quad (2.18)$$

where t_0 and Δt_d are determined by the spark timing and the AFR in the main-combustion chamber. The coefficient a and m are chosen to be 6.908 and 2, respectively.

If a , m , and Δt_d are the same in Eqn. (2.17) and Eqn. (2.18), it can be proved that for any given $t_{ign_b} = t_{ign}$

$$\frac{dx'_b}{dt} = \frac{dx_b}{dt} \cdot b(t). \quad (2.19)$$

In other word, the combustion rate calculated by the new Wiebe function is $b(t)$ times larger than that calculated by the conventional Wiebe function. Therefore, the intensity of the turbulent jet can be mathematically expressed by $b(t)$. The combustion model is able to adjust the rate of combustion by making $b(t)$ as a function of some characteristics of the turbulent jet. Moreover, $b(t)$ can be changed at any time during the combustion process. As long as $b(t)$ is greater than 0, the combustion rate is greater than 0 and $x'_b(t)$ equals to 1 as t goes to infinity. From the available experimental results, it is found that the rate of combustion in the main-combustion chamber is highly related to the mass flow rate of the turbulent jets from the pre-combustion chamber. As a result, it is assumed that the intensity of the turbulent jet can be linked to its mass flow rate.

Although this assumption provides a good match between the modeled and available experimental results, it is important to find an accurate method to calculate the intensity of the turbulent jet in the future when more experimental data are available. Since the influence of the turbulent jet to the combustion in the main-combustion chamber is also delayed, $b(t)$ is modeled to be proportional to the flow rate of the turbulent jet with a first order dynamics; see Eqn. (2.20). An offset is used such that $b(t) = 1$ when the flow rate of the turbulent jet is zero.

$$\begin{aligned}
 b(t) &= \beta \cdot [(\dot{m}_{tur}^+ * f_l)(t)] + 1 \\
 (\dot{m}_{tur}^+ * f_l)(t) &= \int_0^t \dot{m}_{tur}^+(\tau) f_l(t - \tau) d\tau
 \end{aligned}
 \tag{2.20}$$

where ”*” is the convolution operator and \dot{m}_{tur}^+ and f_l are defined as follows

$$\begin{aligned}
 \dot{m}_{tur}^+ &= \begin{cases} \dot{m}_{tur} & \dot{m}_{tur} \geq 0 \\ 0 & \dot{m}_{tur} < 0 \end{cases} \\
 f_l(t) &= \omega_c e^{-\omega_c t} u(t)
 \end{aligned}
 \tag{2.21}$$

Note that $u(t)$ denotes unit step. The convolution of \dot{m}_{tur}^+ with the exponential decay function f_l represents the first order dynamics and is used to emulate the time delay. To be more specific, f_l is the time response of a low-pass filter with cutoff frequency ω_c . The parameters β and w_c are experimentally determined. When $\dot{m}_{tur} \leq 0$, we have $b(t) = 1$ which means that the combustion rate will not be altered if there is no turbulent jet from the pre-combustion chamber.

2.4 Model Calibration

The combustion model was calibrated using the experimental data collected from the RCM at Michigan State University described in the System Description section. The model is firstly calibrated using two experimental data sets and validated using another data set. Then, to further validated the model, more data sets with different pre-combustion chamber orifice sizes are used. The experimental set-ups for the first three cases can be found in Table 2.2, where cases 1 and 2 are used for model calibration and case 3 for model validation.

Table 2.2: Experimental set-up.

Parameter	Case					
	1	2	3	4	5	6
orifice diameter (mm)	1.5	1.5	1.5	2.0	2.0	2.5
main-chamber AFR	1.83	2.10	1.83	1.5	1.25	1.5
pre-chamber fuel addition (mg)	0.66	0.89	0.89	0	0	0
pre-chamber AFR (calculated)	0.98	0.90	0.85	1.5	1.25	1.5

The first step is to calibrate the heat transfer model. To do this, the net heat release (NHR) rate in the main-combustion chamber needs to be calculated from an inverse thermodynamic calculation [18, 22] based on the experimental pressure data. However, this calculation cannot be completed without knowing the mass flow rate between the two combustion chambers. Fortunately, the mass flow between the two combustion chambers mainly influence the combustion process in the pre-combustion chamber. Its effect to the main-combustion chamber is limited. For calibration purpose, the mass flow can be neglected when calculating the NHR rate in the main-combustion chamber. The result of the inverse calculation is shown in the upper plot of Fig. 2.5. The NHR rate is the sum of the CER rate and the heat transfer rate from the cylinder wall. The heat transfer model can be calibrated assuming that the heat transfer rate is dominant where the NHR rate is negative. The calculated heat transfer rate is shown in the bottom plot of Fig. 2.5.

The next step is to calibrate Δt_d for the main-combustion chamber. After the heat transfer model is calibrated, the CER rate can be obtained by subtracting the heat transfer rate from the NHR rate, shown as the dotted line in Fig. 2.5. This allows one to calculate the MFB of the main-combustion chamber, which is the solid line in Fig. 2.6. According to the later stage of the MFB curve (shown in Fig. 2.6), the parameter, Δt_d , in the Wiebe function can be determined by a linear Least-Squares fitting procedure[23]. The dotted line in Fig. 2.6 is the curve fitting result. The parameter $b(t)$ is set to be 1 during this calibration procedure.

Because the heat transfer coefficient h_c of the pre-combustion chamber is assumed to be equal

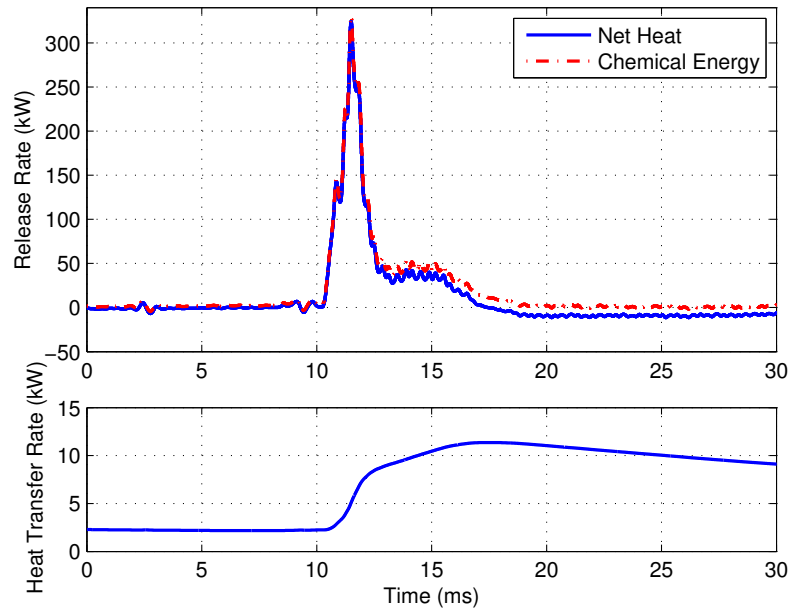


Figure 2.5: Inverse thermodynamic calculation results.

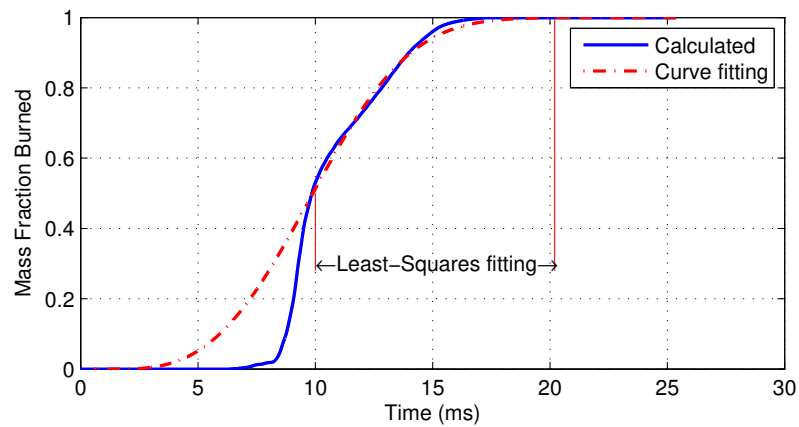


Figure 2.6: MFB obtained from inverse thermodynamic calculation and Least-Squares fitting result.

to that of the main-combustion chamber. The heat transfer rate to the pre-combustion chamber wall is determined. This allows one to calibrate the other unknown parameters in Table 2.3 using a nonlinear Least-Squares optimization procedure. Among these parameters, c_{pre} , c_{main} , ω_c and β in Eqn. (2.12) and Eqn. (2.20) remain constant for all the first three experimental cases. The results of the linear Least-Squares fitting and nonlinear Least-Squares optimization procedures are shown in Table 2.3.

The nonlinear Least-Squares optimization problem is solved by the nonlinear Least-Squares solver in Matlab using the Trust-Region-Reflective algorithm. This algorithm minimizes the following function.

$$\sum_{i=1}^n (P_{pre-i} - \hat{P}_{pre-i})^2 + \sum_{i=1}^n (P_{main-i} - \hat{P}_{main-i})^2 \quad (2.22)$$

where n is the total number of the data points; P_{pre-i} and P_{main-i} are the experimental pressure points; \hat{P}_{pre-i} and \hat{P}_{main-i} represent the modeled pressure points; i is the data index.

Table 2.3: Calibration results for cases 1 and 2.

Parameter		Case 1	Case 2
	c_{pre}	0.655	0.655
	c_{main}	0.01	0.01
	ω_c	3263	3263
	β	1.72	1.72
pre-chamber	Δt_d (ms)	4.17	3.94
	η_{pre}	0.941	0.884
main-chamber	Δt_d (ms)	19.3	28.6
	η_{main}	0.912	0.975

2.5 Model Validation and Simulation Results

After the calibration procedure, the model is then validated by the third experimental data set listed in Table 2.2. The simulation parameters for the third experimental case are determined based on the following simple assumptions. Since the AFR in the main-combustion chamber of the third case is the same as the first one, Δt_d and η_{main} of the main-combustion chamber are assumed

the same as the first case. In the pre-combustion chamber, the other combustion parameters are assumed to vary linearly with the AFR for the three experimental cases, because their AFRs in the pre-combustion chamber are within a relatively small range. Based on the calculated AFRs in Table 2.2, the coefficients, Δt_d and η_{pre} of the pre-combustion chamber are calculated and listed in Table 2.4. The parameters, c_{pre} , c_{main} , ω_c and β , remain the same. Figs. 2.7-2.9 show the comparison between the modeled and experimental pressure traces in two combustion chambers for the three experimental cases. The calculated pressure traces for the first two cases match the experimental pressure traces very well, since their parameters are obtained by the calibration procedure. Although the combustion parameters for the third case are calculated based on the very simple assumptions discussed above, the agreement between the modeled and measured pressure traces is satisfactory. The relative errors on the pressure traces are always below 10%. The errors mainly occur after 31 ms in Fig. 2.9. These errors are mainly caused by the simple assumptions used for determining the simulation parameters for case 3. In reality, the combustion process in the main-combustion chamber does not only depend on the parameters in the main-combustion chamber. The relationship between the combustion parameters and the AFR in the pre-combustion chamber is also not exactly linear. Once more experimental data are available, further calibration can be done and model accuracy can be improved.

Table 2.4: Simulation parameters.

Parameter	Case 3
c_{pre}	0.655
c_{main}	0.01
ω_c	3263
β	1.72
pre-chamber	
Δt_d (ms)	3.80
η_{pre}	0.848
main-chamber	
Δt_d (ms)	19.3
η_{main}	0.912

One of the main differences between TJI combustion and conventional SI combustion is that the turbulent jet increases the rate of combustion in TJI combustion. The experimental and calculated

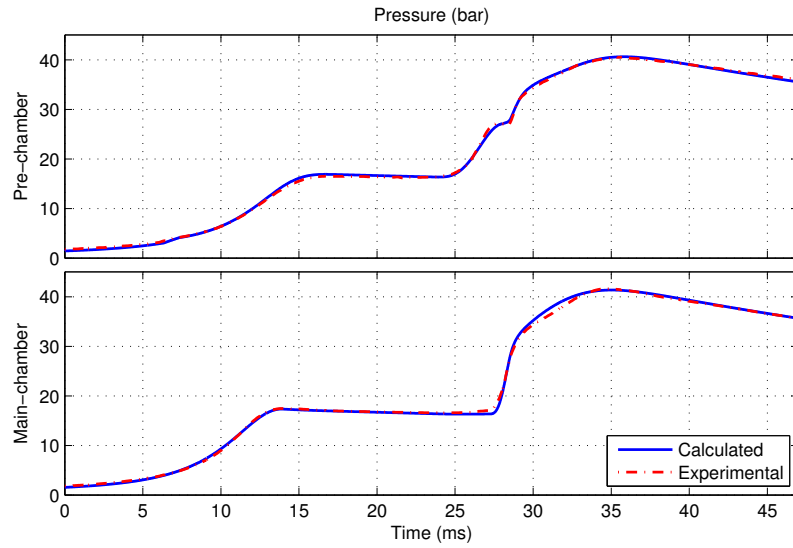


Figure 2.7: Experimental and calculated pressure traces for experimental case 1.

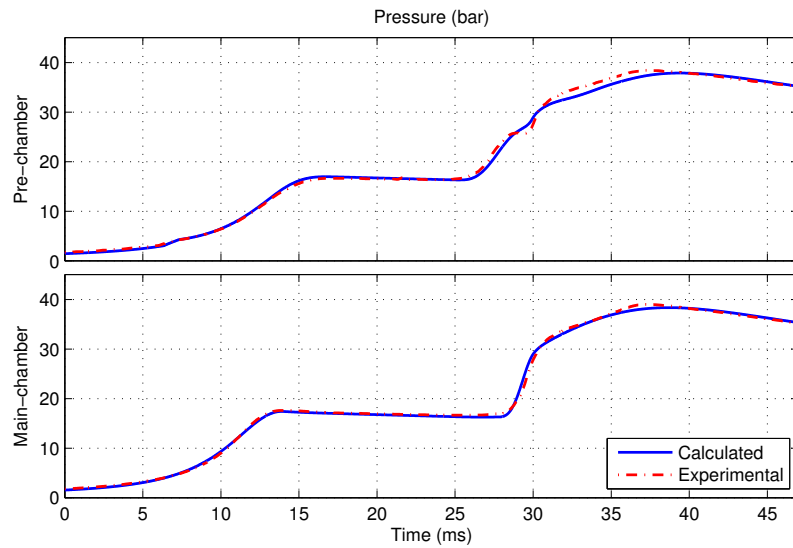


Figure 2.8: Experimental and calculated pressure traces for experimental case 2.

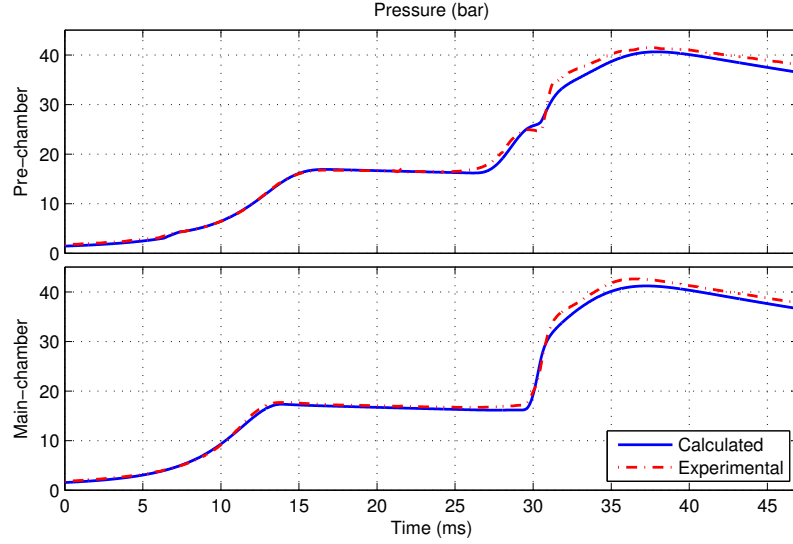


Figure 2.9: Experimental and calculated pressure traces for experimental case 3.

NHR rates are compared in Fig. 2.10. We can find a pick on the NHR rate curve at the early stage of the combustion, which is caused by the turbulent jet. As an example, Fig. 2.11 shows how the model simulates the rate of combustion according to the mass flow rate of the turbulent jet. The top plot of Fig. 2.11 shows the mass flow rate through the orifice connecting the two combustion chambers. The curve in the middle plot of Fig. 2.11 is $b(t)$ in Eqn. (2.20). The bottom plot of Fig. 2.11 is the calculated CER rate. According to the simulation results, the MFB model with the parameter-varying Wiebe function successfully links the combustion processes in two combustion chambers.

The value of the coefficient α_b during the simulation is shown in Fig. 2.12, where the dashed line is the value of α_b calculated by assuming P_{pre} is greater than P_{main} and the dash-dotted line is the value of α_b calculated by assuming P_{pre} is less than P_{main} . The actual value of α_b used for combustion calculation, that is shown by the solid line, is on the dashed line at beginning because the pre-combustion chamber is ignited first. After the switch line (see Fig. 2.12), the main-combustion chamber pressure becomes larger than that of the pre-combustion chamber, α_b jumps from the dashed line to the dash-dotted line.

To further validate the model, twelve more experimental data sets were used. The orifice

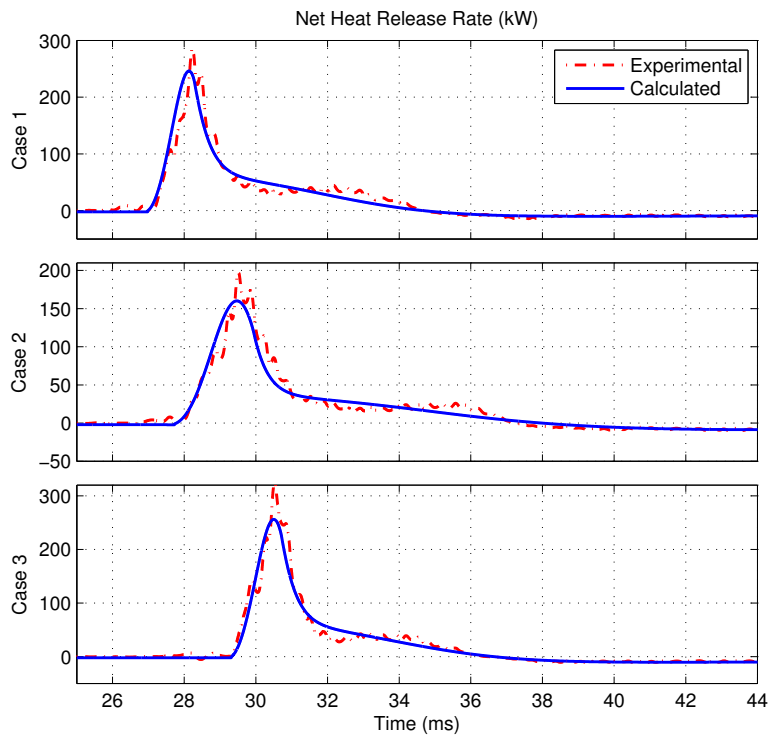


Figure 2.10: Experimental and calculated net heat release rates.

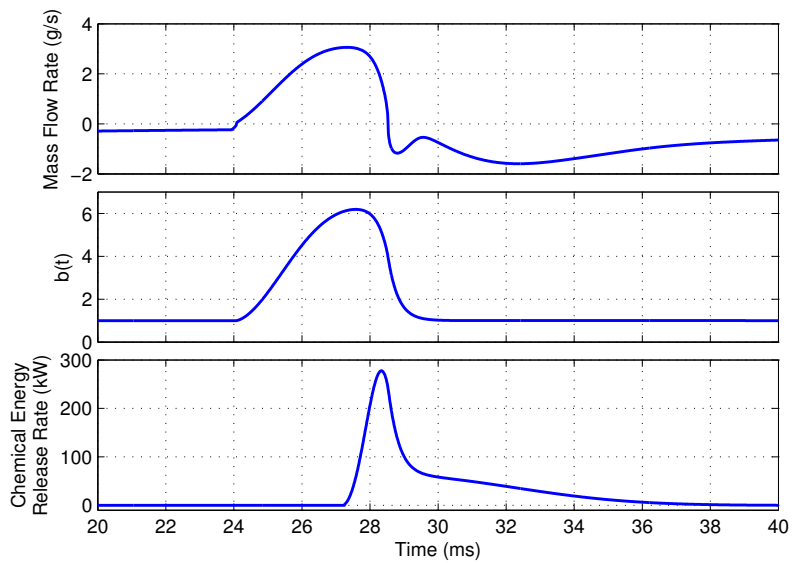


Figure 2.11: Chemical energy release rate calculation.

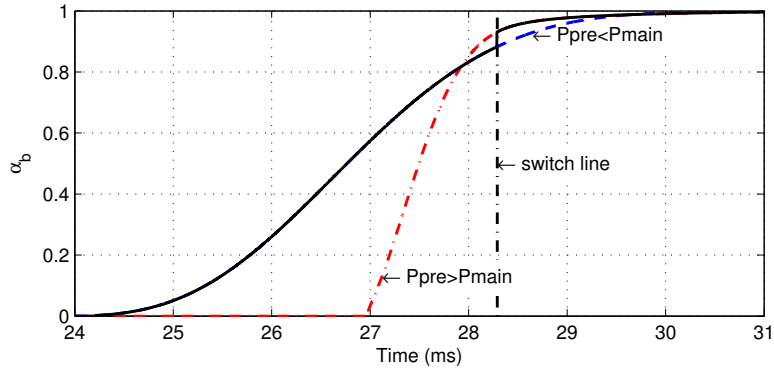


Figure 2.12: The calculated value of αb during combustion.

diameter varied from 2.0 mm to 3.0 mm. The relative AFRs in the two combustion chambers varied from 0.9 to 1.5. To simplify the presentation, the pressure traces were plotted only for the first three cases; see Figs. 13-15. The experimental set-ups for the three cases are shown in Table. 2, as cases 4-6. The associated calibration results can be found in Table. 5. For the other cases, the calculated 10-50% burn duration (Burn1050) and 50-90% burn duration (Burn5090) of the main-combustion chamber were compared with the experimental values; see Fig. 16-17. Due to large variations of orifice areas and AFRs of these data sets, the model parameters need to be re-calibrated. However, β and w_c were kept unchanged for the cases with the same orifice sizes, like cases 4 and 5. It was also found that c_{pre} and c_{main} were very similar for all the experimental cases. This indicates that these two parameters are mainly associated with the combustion chamber structure. In Table. 5, the pre-combustion chamber burn durations are quite different from the previous experimental cases 1-3. This is due to the difference in the orifice area.

To conclude, the proposed model is able to fit the experimental data sets with large ranges of AFRs in both combustion chambers and different pre-combustion chamber orifice areas. This indicates that the developed combustion model has the potential to be used for the development of TJI engine model.

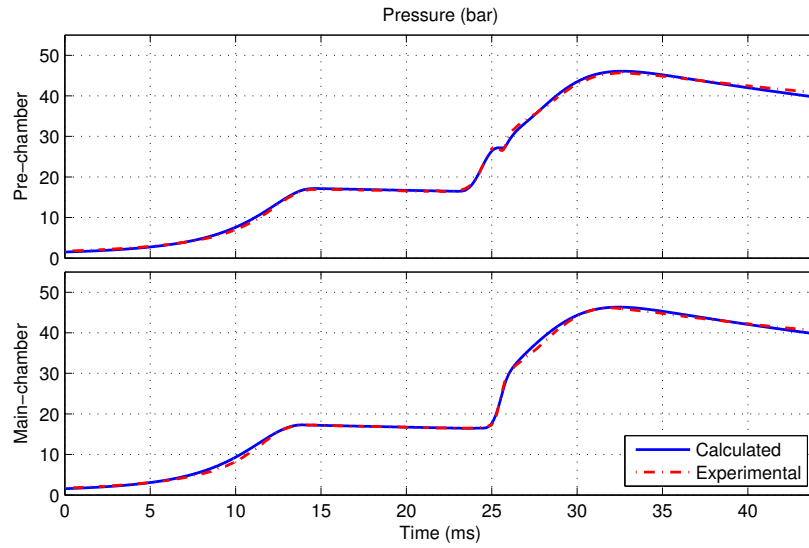


Figure 2.13: Experimental and calculated pressure traces for experimental case 4.

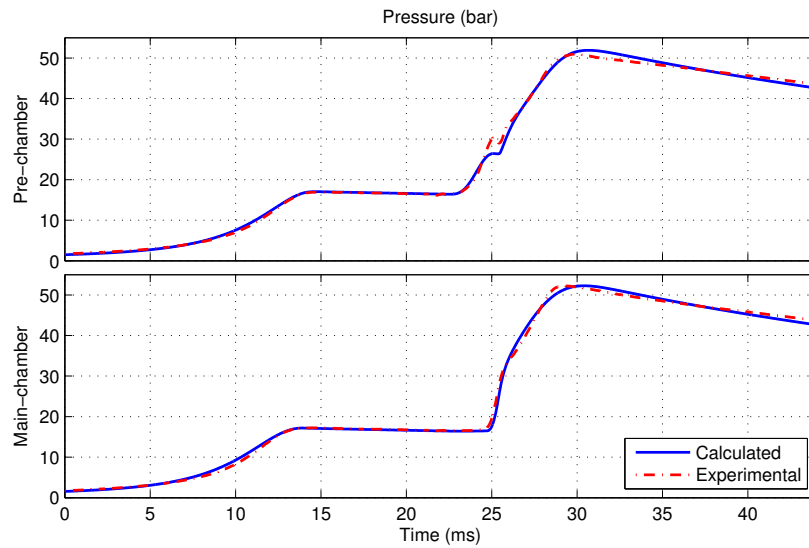


Figure 2.14: Experimental and calculated pressure traces for experimental case 5.

Table 2.5: Calibration results for cases 4-6.

Parameter		Case 4	Case 5	Case 6
	c_{pre}	0.651	0.651	0.651
	c_{main}	0	0	0
	ω_c	3829	3829	5064
	β	0.824	0.824	0.764
pre-chamber	Δt_d (ms)	1.97	2.28	1.79
	η_{pre}	0.980	0.939	0.901
main-chamber	Δt_d (ms)	16.5	11.2	14.0
	η_{main}	0.927	0.905	0.932

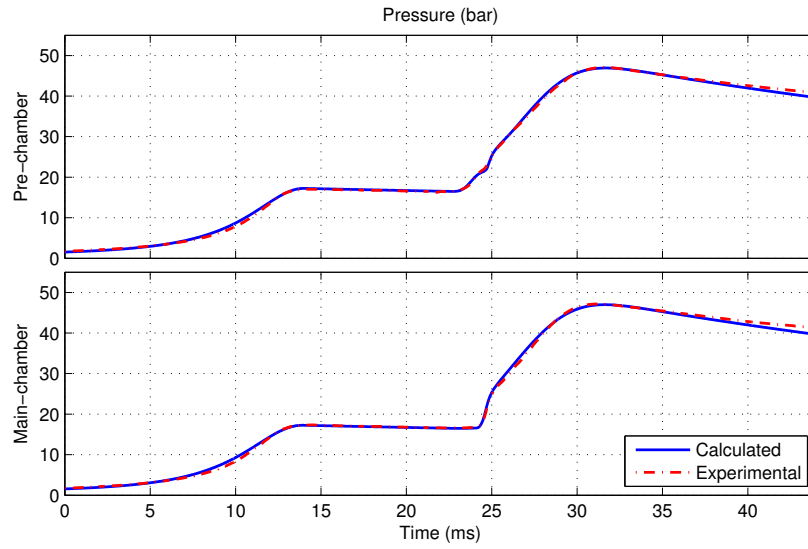


Figure 2.15: Experimental and calculated pressure traces for experimental case 6.

2.6 Conclusion

This chapter presents a control-oriented TJI combustion model for the RCM (rapid compression machine) at Michigan State University. A newly proposed parameter-varying Wiebe combustion model is used to link the combustion processes in both pre- and main-combustion chambers. The developed model can be calibrated using a simple and systematic calibration procedure based on the experimental data. The model validation process shows a good agreement between the modeled and experimental pressure traces, which indicates that the developed model is capable of accurately capturing the TJI combustion dynamics. The validation results also indicate that the

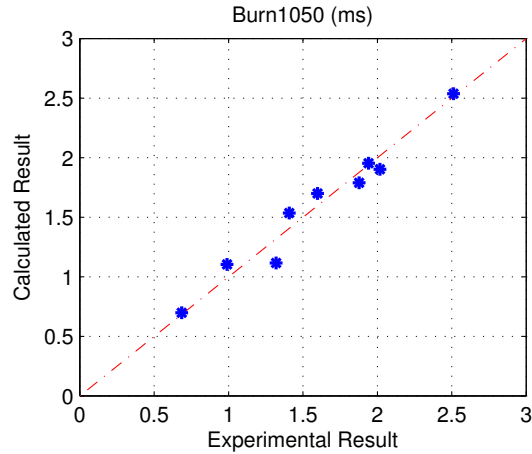


Figure 2.16: Experimental and calculated Burn1050 in the main-combustion chamber.

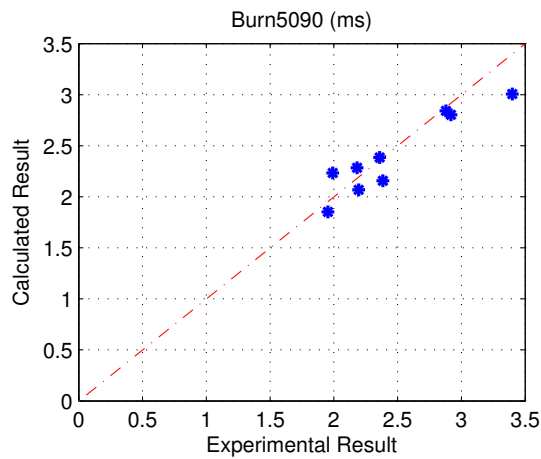


Figure 2.17: Experimental and calculated Burn5090 in the main-combustion chamber.

model is able to predict the combustion process that is not used to calibrate the model parameters. This shows that the developed model has the potential to be used for studying TJI combustion engines and developing the associated control strategies. Although only methane is used as the fuel in this chapter, this model can be extended to other gaseous fuels with new calibrations. However, for the liquid fuel, the model structure may need to be changed, especially a gas-fuel mixing model will be required. The next step is to extend the modeling work for TJI engines using gaseous fuel. Note that in this case the piston dynamics and gas exchange (intake and exhaust) models need to be added. If the liquid fuel is used, an gas-fuel mixing model will also be required.

CHAPTER 3

A CONTROL-ORIENTED COMBUSTION MODEL FOR A TURBULENT JET IGNITION ENGINE USING LIQUID FUEL

3.1 Introduction

The TJI combustion system introduces additional freedoms for combustion control. For instance, pre- and main-chamber AFRs, pre-chamber fuel injection and ignition timing. This makes it difficult to utilize the traditional single variable feedback and look-up table based control, and it often requires real-time optimization, especially during the transient operations. Therefore, model-based control is required to handle multiple-input and multiple-output TJI combustion system. Development of the control-oriented TJI combustion model serves two purposes. One is to quantitatively understand the influence of control parameters to TJI combustion performance and the other is to develop the physics-based TJI combustion model for model-based control.

The engine model developed in this article is for a single cylinder engine equipped with a TJI system. Different from many other TJI engines, liquid gasoline is used as the fuel for both the pre- and main-chambers. Since liquid gasoline is hard to be fully vaporized inside the small pre-chamber before combustion starts, an air-fuel mixing and fuel vaporization model is proposed for the pre-chamber in this article. In order to simulate the combustion performance variations due to the interactions between the two combustion chambers, a parameter-varying Wiebe function is used to model the main-chamber burn rate. The air-fuel mixture in the two combustion chambers are modeled using two zones (burned and unburned) to simulate the complicated gas exchange process between the two chambers.

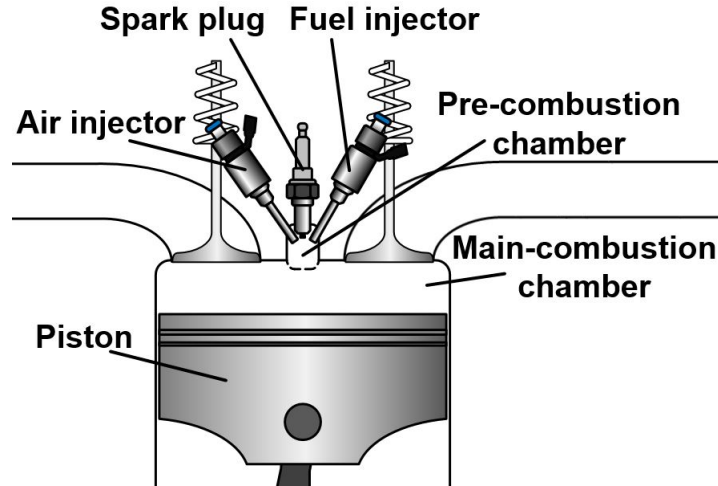


Figure 3.1: TJI engine architecture

3.2 TJI Combustion Model Architecture

3.2.1 Target engine description

Fig. 3.1 shows the basic architecture of the single cylinder TJI engine modeled in this article. The engine specifications are listed in Table 3.1. In order to have a good mixing inside the pre-chamber, most of TJI engines use gaseous fuel in the pre-chamber, which is not practical for liquid fuel engines due to the required dual-fuel systems, leading to inconvenience, high system complexity and cost. Therefore, liquid gasoline is used in both chambers for the TJI engine at Michigan State University. Due to the small volume of the pre-chamber and the comparatively long fuel penetration, a large amount of fuel will be sprayed directly onto the pre-chamber wall. To control the AFR and improve the air-fuel mixing in the pre-chamber, an air injector, located in the opposite side of the fuel injector, is used. When the fuel injector is turned on, the pressurized air is also injected against fuel jets to reduce the amount of fuel impingement on the pre-chamber wall. The spark plug is mounted at the top of the pre-chamber. The two combustion chambers are connected through six orifices. The size of each orifice is listed in Table 3.1.

Table 3.1: TJI Engine Specifications

Parameter	Value
Bore	95 mm
Stroke	100 mm
Con-rod	190 mm
Compression ratio	11.5:1
Pre-chamber volume	2.7 cm ³
Pre-chamber orifice diameter	1.5 mm
Intake/exhaust valve lifts	8.3 mm/8.3 mm

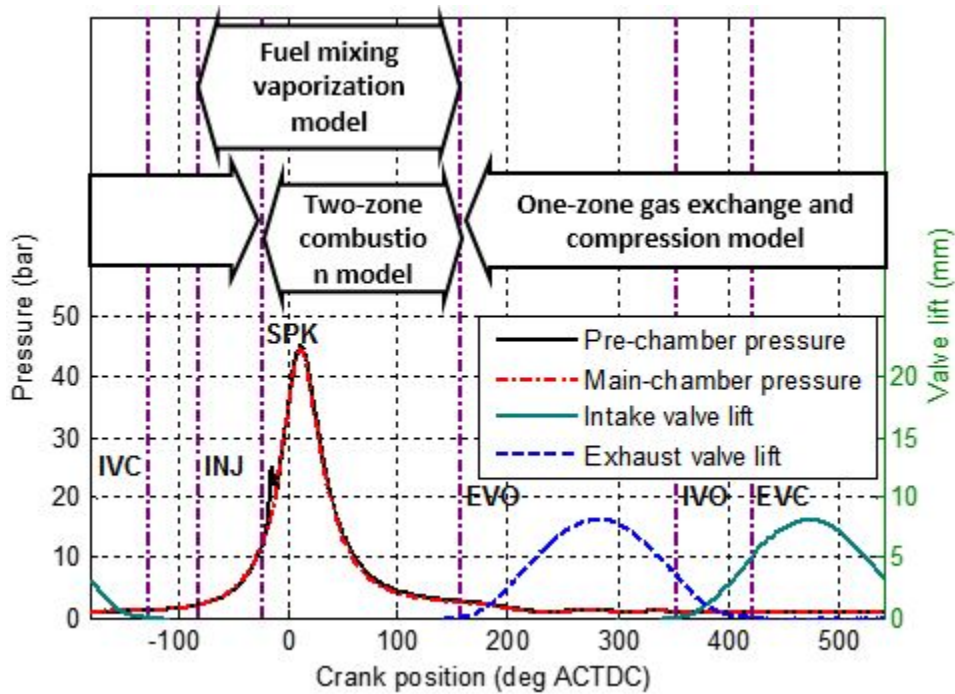


Figure 3.2: Key events over an engine cycle for TJI engine modeling. IVO: intake valve opening; IVC: intake valve closing; EVO: exhaust valve opening; EVC: exhaust valve closing; SPK: spark timing; and INJ: pre-chamber fuel and air injection.

3.2.2 Engine events and combustion model architecture

Fig. 3.2 illustrates the engine events and the corresponding modeling methods over one engine cycle. For the current TJI engine configuration, the intake and exhaust valve timings are fixed but the proposed model is also suitable for engines with variable valve timing. During the intake stroke, fresh air and fuel flow (through port-fuel-injection) into the main-chamber and mix with the

residual gas inside the main-chamber. It is assumed that the air, fuel and residual gas are uniformly mixed. Therefore, the gas inside the main-chamber is considered as one single zone, and one-zone gas exchange model is used to calculate the gas properties in the main-chamber. After intake valve closing (IVC), the piston compresses the gas inside the main-chamber and thus the pressure in the main-chamber increases. The pressure difference between the two combustion chambers pushes the gas from the main-chamber into the pre-chamber. The pressure in the pre-chamber increases and follows the main-chamber pressure. During this process, the gas inside the pre-chamber is also considered as a single zone. To control the AFR and residual gas contents inside the pre-chamber, additional fuel and air are injected into the pre-chamber during the compression stroke, where air injection is also used during the fuel injection to reduce the fuel wall-wetting effect in the pre-chamber. The fuel and air injection (INJ) timings are shown in Fig. 3.2. After INJ, the fuel mixing and vaporization model calculates the vaporized fuel amount inside the pre-chamber based on the amount of injected fuel and the fuel vaporization rate on the pre-chamber wall. When the piston moves close to the combustion top dead center (CTDC), the spark plug discharges and ignites the mixture inside the pre-chamber. Then, the reacting products in the pre-chamber are pushed out and ignite the mixture in the main-chamber. After the ignition in the pre-chamber, the gas inside the combustion chambers is divided into two zones, burned and unburned zones. In the pre-chamber, the fuel vaporization model calculates the fuel masses vaporized from the pre-chamber wall for both zones. A single step reaction based model is used to calculate the combustion rate inside the burned zone in the pre-chamber. In the main-chamber, the combustion rate is calculated by the parameter-varying Wiebe function. The modeling details are discussed in the next section.

3.3 Gas Exchange Model

During the exhaust, intake and compression strokes before ignition, the engine is modeled by the one-zone model. The following assumptions are made:

1. Fuel and air are uniformly premixed in the intake manifold.
2. The gas inside the pre- or main-chamber is homogeneous, and thus can be considered as one

zone. However, the properties of the gas in one chamber can be different from that in the other chamber.

During the intake stroke, the mass flow rate of the intake fresh charge can be calculated by the one-dimensional compressible flow equation [1].

$$\dot{m}_{int} = C_{d,int} A_{v,int} \frac{P_{int}}{\sqrt{RT_{int}}} \psi \left(\frac{P_{main}}{P_{int}} \right) \quad (3.1)$$

where

$$\psi(x) = \begin{cases} \sqrt{\kappa \left(\frac{2}{\kappa+1} \right)^{\frac{(\kappa+1)}{(\kappa-1)}}} & x < \left(\frac{2}{\kappa+1} \right)^{\frac{\kappa}{(\kappa-1)}} \\ x^{\frac{1}{\kappa}} \sqrt{\frac{2\kappa}{\kappa-1} \left(1 - x^{\frac{(\kappa-1)}{\kappa}} \right)} & x \geq \left(\frac{2}{\kappa+1} \right)^{\frac{\kappa}{(\kappa-1)}} \end{cases} \quad (3.2)$$

Note that $A_{v,int}$ is the intake valve reference area; the discharge coefficient $C_{d,int}$ is experimentally determined; κ is the ratio of specific heats; R is the gas constant; P_{int} and T_{int} are the upstream pressure and temperature in the intake manifold, respectively; and P_{main} is the main-chamber pressure .

During the exhaust stroke, the mass flow rate of the gas flowing through the exhaust valve, \dot{m}_{exh} , can be calculated similarly.

The gas exchange process between the two combustion chambers is also modeled in the similar way. However, the pressure in the pre-chamber can be either greater or less than that in the main-chamber. Therefore, the following equation is used to calculate the mass flow rate between the two combustion chambers.

$$\dot{m}_{tur} = \begin{cases} C_{d,tur} A_{v,tur} \frac{P_{pre}}{\sqrt{RT_{pre}}} \psi \left(\frac{P_{main}}{P_{pre}} \right) & P_{pre} \geq P_{main} \\ -C_{d,tur} A_{v,tur} \frac{P_{main}}{\sqrt{RT_{main}}} \psi \left(\frac{P_{pre}}{P_{main}} \right) & P_{pre} < P_{main} \end{cases} \quad (3.3)$$

where $C_{d,tur}$ and $A_{v,tur}$ are the discharge coefficient and the area of the orifice connecting the two combustion chambers; respectively. Note that the subscripts *pre* and *main* denote the pre- and main-chamber properties, respectively.

Before ignition, the main-chamber is considered as a control volume with mass and energy exchange. The following mass and energy conservation equations describe such a control volume.

$$\begin{aligned}\frac{dm_{main}}{dt} &= \dot{m}_{int} - \dot{m}_{exh} + \dot{m}_{inj} - \dot{m}_{tur} \\ \frac{d(m_{main}u_{main})}{dt} &= \dot{m}_{int}h_{int} - \dot{m}_{exh}h_{exh} \\ &+ \dot{m}_{tur}h_{tur} - \dot{Q}_{ht}^{main} - \frac{dW}{dt}\end{aligned}\quad (3.4)$$

where m_{main} and u_{main} are the mass and internal energy of the gas in the main-chamber, respectively; \dot{Q}_{ht}^{main} is the heat transfer rate through the chamber wall; and $\dot{m}h$ is the enthalpy flow. The work of the pressure force, W , is calculated by:

$$\frac{dW}{dt} = P_{main} \frac{dV_{main}}{dt} \quad (3.5)$$

where V_{main} is the main-chamber volume. The Woschni correlation model [20] is used to calculate the quantity of heat transfer.

$$\begin{aligned}\dot{Q}_{ht}^{main} &= A_w^{main} h_c (T_{main} - T_w) \\ h_c &= qB^{-0.2} P^{0.8} (C_1 \bar{V}_p)^{0.8} T_{main}^{-0.55}\end{aligned}\quad (3.6)$$

where \bar{V}_p is the mean piston velocity and $C_1 = 2.28$; B is the cylinder bore; A_c is the main-chamber wall area; and coefficient q is a calibration parameter.

The mass and energy conservation equations for the pre-chamber can be expressed as:

$$\begin{aligned}\frac{dm_{pre}}{dt} &= \dot{m}_{inj} - \dot{m}_{tur} \\ \frac{d(m_{pre}u_{pre})}{dt} &= \dot{m}_{inj}h_{inj} - \dot{m}_{tur}h_{tur} - \dot{Q}_{ht}^{pre}\end{aligned}\quad (3.7)$$

where m_{pre} and u_{pre} are the mass and internal energy of the gas in the pre-chamber, respectively; \dot{Q}_{ht}^{pre} is the heat transfer rate through the pre-chamber wall. The subscripts *inj* and *tur* represent the properties of the gas from the fuel and air injectors and through the orifice connecting the two combustion chambers, respectively.

Assuming that the gas can be considered to be ideal, the above equations can be coupled using the ideal gas law as follows.

$$P \cdot V = m \cdot R \cdot T \quad (3.8)$$

Finally, the pressures and temperatures in both of the two combustion chambers can be obtained by substituting Eqn. (3.8) into Eqns. (3.4) and (3.7).

3.4 Fuel Mixing and Vaporization Model

As discussed in the last section, although an air injector is used in the pre-chamber, it is difficult to completely prevent the injected liquid gasoline from shooting onto the chamber wall. Therefore, a fuel mixing and vaporization model is developed based on the following assumptions:

1. The injected fuel can be divided into two parts: vaporized and liquid fuel. The vaporized fuel uniformly mixes with the gas in the pre-chamber immediately after injection.
2. The injected liquid fuel forms a fuel film on the chamber wall, and the area fraction of the fuel film contacting with the burned (or unburned) zone is the same as the volume fraction of the burned (or unburned) zone.
3. The fuel film surface temperature contacting the gas mixture is assumed to be the same as the gas temperature. The actual temperature should be lower, but this modeling error can be absorbed by the coefficient h_m in Eqn. (3.11).

The amounts of vaporized and liquid fuel are simply calculated by the following equations based on the total fuel injected into the pre-chamber.

$$\begin{aligned}\dot{m}_{f,wall}^{pre} &= k \cdot \dot{m}_{f,inj}^{pre} \\ \dot{m}_{f,mix}^{pre} &= (1 - k) \cdot \dot{m}_{f,inj}^{pre}\end{aligned}\tag{3.9}$$

where $\dot{m}_{f,inj}^{pre}$ is the pre-chamber fuel injection rate and the superscript *pre* represents the pre-chamber properties; $\dot{m}_{f,wall}^{pre}$ is the rate of the fuel deposited on the pre-chamber wall; and $\dot{m}_{f,mix}^{pre}$ is the rate of the injected fuel that directly vaporises and mixes with the gas inside the pre-chamber.

The fuel deposited on the pre-chamber wall forms a thin fuel film and continue vaporizing, see Fig. 3.3. The mass of the fuel film can be calculated by

$$\dot{m}_{f,film}^{pre} = \dot{m}_{f,wall}^{pre} - \dot{m}_{f,evap}^{pre}\tag{3.10}$$

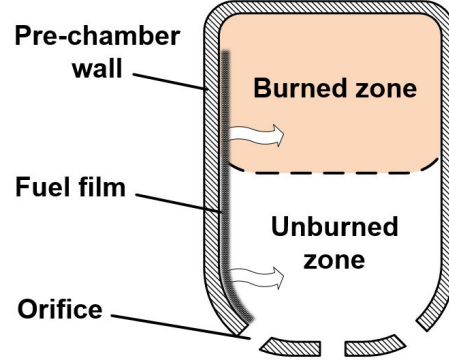


Figure 3.3: Pre-chamber fuel vaporization model.

where $m_{f, \text{film}}^{\text{pre}}$ is the mass of the fuel film on the chamber wall; and $\dot{m}_{f, \text{evap}}^{\text{pre}}$ is the fuel vaporization rate from the fuel film. It is calculated based on the net molar diffusion flux of the fuel, N_f .

According to Fick's law:

$$N_f = \frac{\dot{m}_{f, \text{evap}}^{\text{pre}}}{M_f A_f} = h_m (c_{f, \text{film}} - c_{f, \infty}) \quad (3.11)$$

where h_m is the mass transfer coefficient; M_f is the average molecular weight of the fuel; A_f is the surface area of fuel film exposed to the pre-chamber gas; and $c_{f, \text{film}}$ and $c_{f, \infty}$ are the fuel vapor concentrations near the fuel film surface and in the pre-chamber gas, respectively. Since $c_{f, \text{film}} \gg c_{f, \infty}$, $c_{f, \infty}$ is set to zero and $c_{f, \text{film}}$ can be derived according to the ideal gas equation as follows

$$c_{f, \text{film}} = \frac{P_s}{R_m T_f} \quad (3.12)$$

where P_s is the fuel saturated vapor pressure; T_f is the fuel film temperature which is assumed to be the pre-chamber gas temperature; and R_m is the molar gas constant. The saturated fuel vapor pressure can be predicted by the Clausius-Clapeyron equation as

$$P_s = P_{s0} e^{\frac{\Delta H}{R_m T_f}} \quad (3.13)$$

where P_{s0} is the fuel saturated vapor pressure constant; and ΔH is the fuel molar enthalpy of vaporization. According to Eqns. (3.11)-(3.13), the fuel film vaporization rate can be derived as

$$\dot{m}_{f, \text{evap}}^{\text{pre}} = \frac{m_{f, \text{film}}^{\text{pre}}}{\delta_f \rho_f} M_f h_m \frac{P_{s0}}{R_m T_f} e^{\frac{\Delta H}{R_m T_f}} \quad (3.14)$$

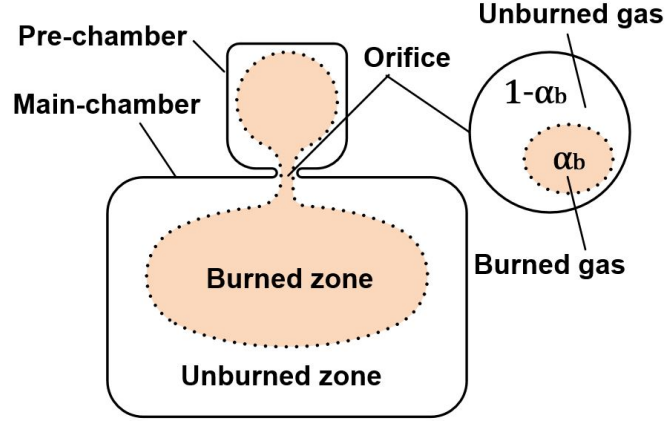


Figure 3.4: Two-zone combustion model. α_b : area fraction for burned gas

where δ_f is the fuel film thickness and ρ_f is the density of the liquid fuel.

After ignition, the pre-chamber is divided into two zones. Correspondingly, the fuel vaporization flow is also divided into two parts: one to the burned zone and the other to the unburned zone; see Fig. 3.3. It is assumed that the mass of the fuel film exposed to the burned zone is $v_b^{pre} m_{f, film}^{pre}$, where v_b^{pre} is the volume fraction of the burned gas in the pre-chamber. Therefore, the fuel vaporization rate to the burned zone can be calculated by replacing $m_{f, film}^{pre}$ with $v_b^{pre} m_{f, film}^{pre}$ in Eqn. (3.14) and using the burned zone temperature for T_f . The fuel vaporization rate to the unburned zone is calculated similarly.

3.5 Two-zone Combustion Model

After ignition, the two combustion chambers are divided into burned and unburned zones to improve the model accuracy. The following assumptions are made in the two-zone combustion model:

1. The gas mixture in each zone is homogeneous.
2. After entering the burned zone, the unburned gas burns immediately and releases the chemical energy inside the burned zone.
3. The heat transfer between the burned and unburned zones can be negligible.

4. The pressure of the gas mixture inside each combustion chamber is assumed to be evenly distributed through the burned and unburned zones.

The burned and unburned zones can be considered as control volumes. Besides the mass, enthalpy, and work exchange between the two zones in each chamber, there are also mass and enthalpy exchanges through the orifice connecting the two combustion chambers. When both the unburned and burned zones are present in the two chambers, the gas in the burned (or unburned) zone of one chamber are assumed to enter the burned (or unburned) zone of another chamber as shown in Fig. 2.3. Before the ignition of the main-chamber, all the gas from the main-chamber is considered as unburned gas. After all the unburned gas in the pre-chamber becomes burned gas, all the gas coming from the main-chamber goes into the burned zone in the pre-chamber. The energy balance equation of the burned zone is shown in Eqn. (3.15). The following equations in this subsection considered the case when both burned and unburned zones are present, and the variables in these equations are for the pre-chamber, if not specified.

$$\begin{aligned} \frac{d(m_b u_b)}{dt} + P \frac{dV_b}{dt} + v_b \dot{Q}_{ht} = \\ \dot{Q}_{ch} + \dot{m}_{u-b} h_u - \dot{m}_{tur,b} h_b \end{aligned} \quad (3.15)$$

The energy balance equation of the unburned zone can be expressed by

$$\begin{aligned} \frac{d(m_u u_u)}{dt} + P \frac{dV_u}{dt} + (1 - v_b) \dot{Q}_{ht} = \\ - \dot{m}_{u-b} h_u - \dot{m}_{tur,u} h_u \end{aligned} \quad (3.16)$$

The masses of burned and unburned gases are calculated based on the following mass conservation law.

$$\begin{aligned} \frac{dm_b}{dt} &= -\dot{m}_{tur,b} + \dot{m}_{u-b} \\ \frac{dm_u}{dt} &= -\dot{m}_{tur,u} - \dot{m}_{u-b} \end{aligned} \quad (3.17)$$

For the above three equations, Q_{ht} is the heat transfer to the chamber wall; Q_{ch} is the chemical energy released by combustion; subscripts b and u represent properties in burned and unburned

zones, respectively; v_b is the volume fraction of the burned zone; \dot{m}_{u-b} is the mass transfer rate from the unburned zone to the burned zone and it will be discussed in the next section. The gas flowing through the orifice contains both burned gas, $\dot{m}_{tur,b}$, and unburned gas, $\dot{m}_{tur,u}$. Correspondingly, the area of the orifice is also divided into two parts: one for the burned gas and the other for the unburned gas, see Fig. 2.3. The two mass flow rates are calculated by the following equations when the pressure in the pre-chamber is greater than that in the main-chamber.

$$\begin{aligned}\dot{m}_{tur,b} &= \alpha_b C_{d,tur} A_{v,tur} \frac{P_{pre}}{\sqrt{RT_b}} \psi \left(\frac{P_{main}}{P_{pre}} \right) \\ \dot{m}_{tur,u} &= (1 - \alpha_b) C_{d,tur} A_{v,tur} \frac{P_{pre}}{\sqrt{RT_u}} \psi \left(\frac{P_{main}}{P_{pre}} \right)\end{aligned}\quad (3.18)$$

Similar results can be obtained when the pressure in the main-chamber is greater than that in the pre-chamber.

The coefficient α_b in Eqn. (3.18) is calculated based on the volume fraction of the burned gas v_b . Assuming that all the burned and unburned gas was evenly distributed in the combustion chambers, α_b would be always equal to v_b . However, in reality, α_b depends on the combustion chamber structure. For the current TJI engine setup, the spark plug is located at the top of the pre-chamber; see Fig. 3.1. As a result, the combustion in the pre-chamber is initiated at the top of the chamber. Therefore, the burned gas is mainly located at the top of the pre-chamber at the early stage of the combustion, which makes it hard for the burned gas to escape through the orifice to the main-chamber. Consequently, the fraction of the burned gas flowing to the main-chamber is much smaller than the burned gas fraction inside the pre-chamber when the gas flow direction is from the pre-chamber to the main-chamber. This is why α_b is smaller than v_b in the pre-chamber when $P_{pre} > P_{main}$. When $P_{pre} < P_{main}$, the gas flow changes its direction and α_b will be determined by the burned gas fraction in the main-chamber. Since the combustion in the main-chamber is initiated at the end of the turbulent jet (far away from orifice)[24], the orifice is surrounded by the gas with high concentration of unburned gas. Therefore, α_b is smaller than v_b in the main-chamber. This is the main reason why the two-zone combustion model is used. To simulate this relationship between α_b and v_b , the value of α_b is calculated by Eqn. (3.19).

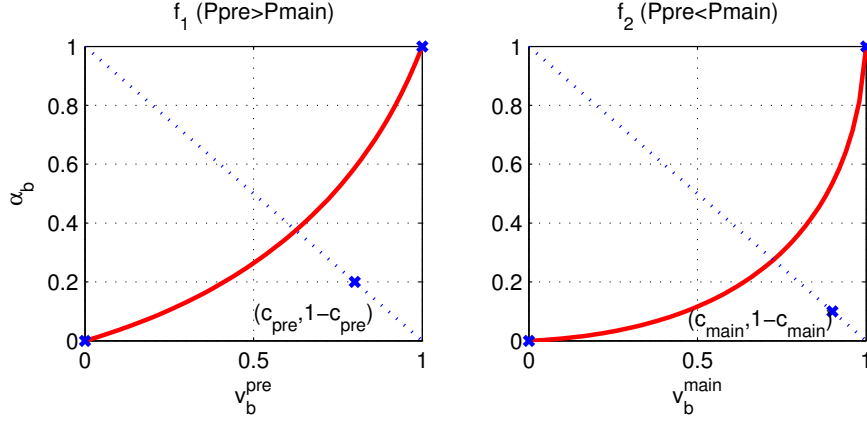


Figure 3.5: The value of α_b in the two cases.

$$\alpha_b = \begin{cases} f_1(v_b^{pre}, c_{pre}) & P_{pre} > P_{main} \\ f_2(v_b^{main}, c_{main}) & P_{pre} < P_{main} \end{cases} \quad (3.19)$$

where the two functions, f_1 and f_2 , are approximated by the second-degree Bézier curves [19], to simplify the calibration process. Each curve is defined by three control points: (0,0) and (1,1) in both curves; and $(c_{pre}, 1 - c_{pre})$ in f_1 , $(c_{main}, 1 - c_{main})$ in f_2 ; see Fig. 2.4. The Bézier curve guarantees $\alpha_b \in [0, 1]$ as long as $c_{pre} \in [0, 1]$ and $c_{main} \in [0, 1]$. When c_{pre} and c_{main} are larger than 0.5, α_b is smaller than v_b during combustion; as shown in Fig. 2.4. The values of c_{pre} and c_{main} are experimentally determined.

The main-chamber is also divided into two zones after ignition. Different from the two-zone combustion model in a conventional SI engine, the combustion model of the main-chamber needs to consider the gas flow through the orifice, especially the unburned fuel from the pre-chamber. The governing equations for the main-chamber are very similar to those of the pre-chamber model presented in this subsection and thus are omitted here. The major difference is that the total volume of the main-chamber is varying.

3.5.1 Pre-chamber combustion rate calculation

The fuel inside the pre-chamber is composed of two parts: vaporized fuel and liquid fuel on the chamber wall. During combustion, the fuel film continues vaporizing into the gas mixture inside the chamber. Therefore, the combustion process is more complicated than that in the main-chamber. After the spark is discharged, the burned zone is created. As the flame front propagates inside the pre-chamber, the fuel in the unburned zone burns and the unburned gas becomes burned gas. It is assumed that all the fuel in the unburned zone burns completely during this process. As a result of combustion, the temperature inside the pre-chamber increases and the fuel vaporization rate also goes up. Because the AFR in the pre-chamber before combustion is close to stoichiometry, there is usually no or little oxygen left inside the burned zone. Therefore, the concentration of the unburned fuel in the burned zone keeps increasing. As all the unburned gas is burned, the pressure in the pre-chamber starts dropping. At this point, the combustion in the main-chamber has already started and the pressure increases rapidly. When the pressure in the main-chamber is greater than that in the pre-chamber, the gas with high concentration of air from the main-chamber enters the pre-chamber burned zone. Then the unburned fuel reacts with the air and the pressure in the pre-chamber increases and becomes the same or even higher than the pressure in the main-chamber.

The mass transfer rate of the gas from the unburned zone to the burned zone is obtained from the Wiebe function[21]:

$$x_b = 1 - \exp \left[-a \left(\frac{t - t_{ign}}{\Delta t_d} \right)^{m+1} \right] \quad (3.20)$$

where x_b is the mass fraction of the burned gas; the coefficients, a and m , are chosen to be 6.908 and 2, respectively; t_{ign} is the start of ignition; and Δt_d is the burn duration that is a function of the AFR right before ignition.

The mass transfer rate of the gas from unburned to burned zone, \dot{m}_{u-b} , can be calculated by:

$$\dot{m}_{u-b} = \frac{m_u}{1 - x_b} \frac{dx_b}{dt} \quad (3.21)$$

where m_u is the mass of the unburned gas. Because the total mass inside the pre-chamber is changing during the combustion, \dot{m}_{u-b} cannot be calculated directly by the total mass.

The rate of chemical energy release in Eqn. (3.15) can be obtained by the following relationship.

$$\dot{Q}_{ch} = \eta_{pre} Q_{LHV} \alpha_{f,u}^{pre} \dot{m}_{u-b} \quad (3.22)$$

where the combustion efficiency η_{pre} is experimentally determined; Q_{LHV} is the lower heating value of the fuel; and $\alpha_{f,u}^{pre}$ is the mass fraction of the fuel in the unburned zone of pre-chamber.

The fuel combustion rate in the burned zone is determined not only by the fuel amount but also by the air amount and other in-cylinder properties, such as the gas temperature. It is not trustworthy to use a conventional Wiebe function to predict the chemical energy release rate. Therefore, a chemical kinetics based model is used to calculate the rate of reaction [25].

$$\frac{d[C_8H_{18}]}{dt} = -A \exp(-E_A/R_u T) [C_8H_{18}]^m [O_2]^n \quad (3.23)$$

where $[C_8H_{18}]$ and $[O_2]$ are the molar concentrations of the fuel and oxygen; A is the pre-exponential factor; and E_A/R_u is the activation temperature. m and n are chosen to be 0.25 and 1.5, respectively. Then the chemical energy release rate can be calculated.

3.5.2 Main-chamber combustion rate calculation

During the TJI engine combustion process, both gas properties in the main-chamber and the turbulent jets from pre-chamber determine the rate of combustion in the main-chamber. The reason is that the turbulent jets are able to create multiple and distributed ignition sites that increase the overall flame front area in the main-chamber. At the same time, the turbulence intensity in the main-chamber is also increased by the turbulent jets and thus the flame front propagation speed goes up. After the turbulent jets disappear, the rate of combustion reduces to a relatively low level, which is mainly determined by the gas properties in the main-chamber. To describe the increment of the combustion rate in the main-chamber caused by the turbulent jets, the term 'intensity' of the turbulent jet is introduced.

Because the turbulent jets are able to change the rate of combustion in the main-chamber, the conventional single-Wiebe function is not suitable for our combustion model. Using multi-Wiebe function is a possible approach for calculating the mass fraction burned. However, this approach requires all the associated parameters to be determined before ignition occurs, which requires significant calibration effort and is not able to model the interactions between the two combustion chambers. Therefore, adjusting the rate of combustion according to the turbulent jet intensity during the combustion process is preferred for the TJI combustion model. Correspondingly, a new parameter-varying Wiebe function is proposed and used in this chapter; see Eqn. (3.24).

$$\begin{cases} x'_b(t) = 1 - \exp \left\{ -a \left[\frac{t - t_{ign_b}(t)}{\Delta t_d} \right]^{m+1} \right\} \\ t_{ign_b}(t) = t_0 - \int_{t_0}^t [b(t) - 1] dt \end{cases} \quad (3.24)$$

where t_0 is the start of ignition; t_0 and Δt_d are determined by the spark timing and the AFR in the main-chamber. The coefficient a and m are chosen to be 6.908 and 2, respectively.

If a , m , and Δt_d are the same in Eqns. (2.17) and (2.18), it can be proved that for any given $t_{ign_b} = t_{ign}$

$$\frac{dx'_b}{dt} = \frac{dx_b}{dt} \cdot b(t). \quad (3.25)$$

In other words, the rate of combustion calculated by the parameter-varying Wiebe function is $b(t)$ times larger than that calculated by the conventional Wiebe function. Therefore, the parameter $b(t)$ is actually the mathematical expression of the intensity of the turbulent jets. Moreover, $b(t)$ can be changed at any time during the combustion process. As a result, the parameter-varying Wiebe function makes it possible for the combustion model to adjust the rate of combustion by making $b(t)$ as a function of some characteristics of the turbulent jets. According to the available experimental results, it is found that the rate of combustion in the main-chamber is highly related to the mass flow rate of the turbulent jets from the pre-chamber. So, it is assumed that the intensity of the turbulent jet can be linked to its mass flow rate. Although this is a simple assumption, it

provides a good match between the simulated and experimental results. Other more complex models can also be developed to calculate the intensity of the turbulent jets more accurately. However, this method is still a preferred one due to its simplicity that is very important for a control-oriented model. Since the influence of the turbulent jets to the combustion in the main-chamber is also delayed, $b(t)$ is modeled to be proportional to the mass flow rate of the turbulent jets with the first order dynamics; see Eqn. (3.26). An offset is used such that $b(t) = 1$ when the flow rate of the turbulent jets is zero.

$$\begin{aligned}
 b(t) &= \beta \cdot [(\dot{m}_{tur}^+ * f_l)(t)] + 1 \\
 (\dot{m}_{tur}^+ * f_l)(t) &= \int_0^t \dot{m}_{tur}^+(\tau) f_l(t - \tau) d\tau
 \end{aligned}
 \tag{3.26}$$

where ”*” denotes the convolution operator and \dot{m}_{tur}^+ and f_l are defined as follows

$$\begin{aligned}
 \dot{m}_{tur}^+ &= \begin{cases} \dot{m}_{tur} & \dot{m}_{tur} \geq 0 \\ 0 & \dot{m}_{tur} < 0 \end{cases} \\
 f_l(t) &= \omega_c e^{-\omega_c t} u(t)
 \end{aligned}
 \tag{3.27}$$

where $u(t)$ denotes the unit step function. The convolution of \dot{m}_{tur}^+ with the exponential decay function f_l represents the first order dynamics and is used to emulate the time delay. To be more specific, f_l is the time response of a low-pass filter with a cutoff frequency of ω_c . The parameters β and ω_c are experimentally determined. $b(t)$ equals to one when $\dot{m}_{tur} \leq 0$, which means that the combustion rate will not be altered if there is no turbulent jets from the pre-chamber.

3.6 Model Calibration and Validation

To calibrate and validate the developed model, experiments were conducted on the single cylinder optical TJI engine, shown in Fig. 3.6, at MSU. The intake and exhaust valve timings are fixed and shown in Fig. 3.2. The crank shaft is connected to the dynamometer. Two Kistler pressure sensors are mounted in the two combustion chambers for capturing both chamber pressures. The

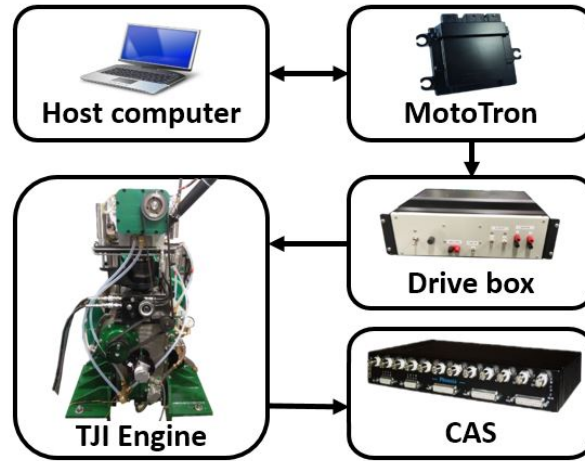


Figure 3.6: TJI engine at MSU.

pressure and other signals coming from the sensors are conditioned and recorded by a Phoenix Combustion Analysis System (CAS) provided by the A&D Technology.

To calibrate the model, experiments were conducted at three different engine speeds. At each engine speed, four different engine load conditions were used during the experiment. Upon calibration, the model was then validated by a set of experiments with different operational conditions shown in Fig. 3.7, where the y-axis is the indicated mean effective pressure (IMEP). For the current TJI engine, the maximum achievable air-fuel equivalence ratio, λ , is about 2 with stable combustion. Note that the criterion of stable combustion is the coefficient of variation of IMEP to be less than 3%. The data points around the dash-dot line in Fig. 3.7 corresponds to the engine operational condition with wide open throttle (WOT) and $\lambda \approx 2$. Above the dash-dot line, the engine runs with WOT and $\lambda < 2$. Below the dash-dot line, the amount of air flowing into the cylinder needs to be reduced by closing the throttle to obtain a stable combustion. Besides the validation data shown in Fig. 3.7, other experimental data with different pre-chamber fuel injection amounts are used to further validate the model. Since the engine is an optical single-cylinder engine, the maximum engine speed is limited by its rotational balancing. Therefore, the maximum engine speed is limited to 2000 rpm in the experiments.

The model is calibrated using the following steps. First, the discharge coefficients, $C_{d,int}$,

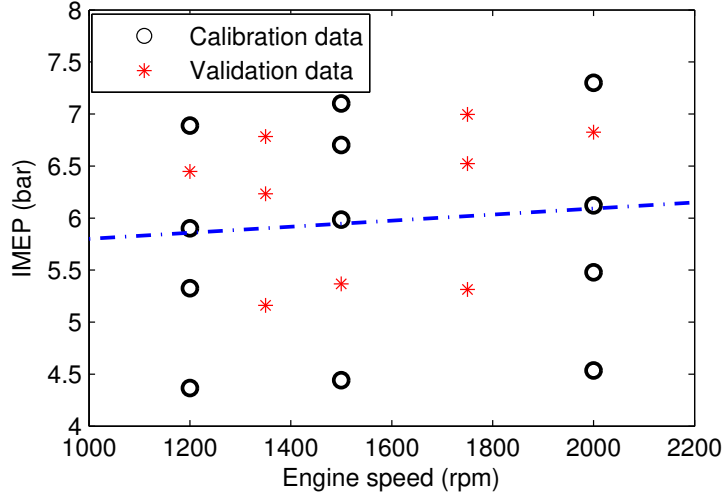


Figure 3.7: Experiment matrix.

$C_{d,exh}$ and $C_{d,tur}$, in Eqns. (2.1) and (2.3) are calibrated by matching the simulated pressure traces with several experimental pressure traces obtained by motoring the engine. Second, the heat transfer coefficient, q , in Eqn. (3.6) is calibrated using the similar method stated in [18]. This method first calculates the net heat release (NHR) rate by an inverse thermodynamic calculation and then calibrates the heat transfer model by assuming that the heat transfer is dominant where the NHR rate becomes negative from the end of combustion to EVO. Note that NHR includes both the chemical energy and heat transfer to the chamber wall. Third, parameters, c_{pre} in Eqn. (2.12), k in Eqn. (3.9), and Δt_d in Eqn. (2.17), are calibrated by matching the pre-chamber pressure during the early stage of combustion (-25 to 0 deg ACTDC in Fig. 3.8). Then, parameters, c_{main} in Eqn. (2.12), δ_f in Eqn. (3.14), A and E_A/R_u in Eqn. (3.23), are adjusted according to the pre-chamber pressure in the later stage of the combustion. After the parameters in the pre-chamber model are calibrated, the main-chamber parameters can be calibrated by matching the main-chamber simulated pressure curve to be the same as the experimental one. Table. 3.2 shows all the model calibration parameters. Most of these parameters are constant within the entire engine operational range. Some of them are functions of other parameters, like engine speed and intake manifold pressure, P_{int} . These functions are implemented by look-up tables.

Table 3.2: Calibration Parameters

Parameter	Symbol	Function of/Value(if constant)	Unit
Intake valve discharge coefficient	$C_{d,int}$	0.9	
Exhaust valve discharge coefficient	$C_{d,exh}$	0.9	
Pre-chamber orifice discharge coefficient	$C_{d,tur}$	0.85	
Heat transfer coefficient	q	389	
Thickness of the fuel film	δ_f	0.03	<i>mm</i>
Bézier curve coefficients	c_{pre}, c_{main}	0.8, 0.9	
Portion of fuel injected on pre-chamber wall	k	0.4	
Pre-chamber Wiebe function coefficient	Δt_d	engine speed, P_{int} , λ_{pre}	<i>ms</i>
Pre-chamber combustion efficiency	η_{pre}	engine speed, P_{int} , λ_{pre}	
Pre-exponential factor	A	$1.7 \cdot 10^{13}$	$(mol/cm^3)^{1-m-n}/s$
Activation temperature	E_A/R_u	engine speed, P_{int}	<i>K</i>
Main-chamber Wiebe function coefficient	Δt_d	engine speed, P_{int} , λ_{main}	<i>ms</i>
Coefficient of parameter-varying Wiebe function	β	engine speed, P_{int} , λ_{main}	
Coefficient of parameter-varying Wiebe function	ω_c	10000	<i>rad/s</i>

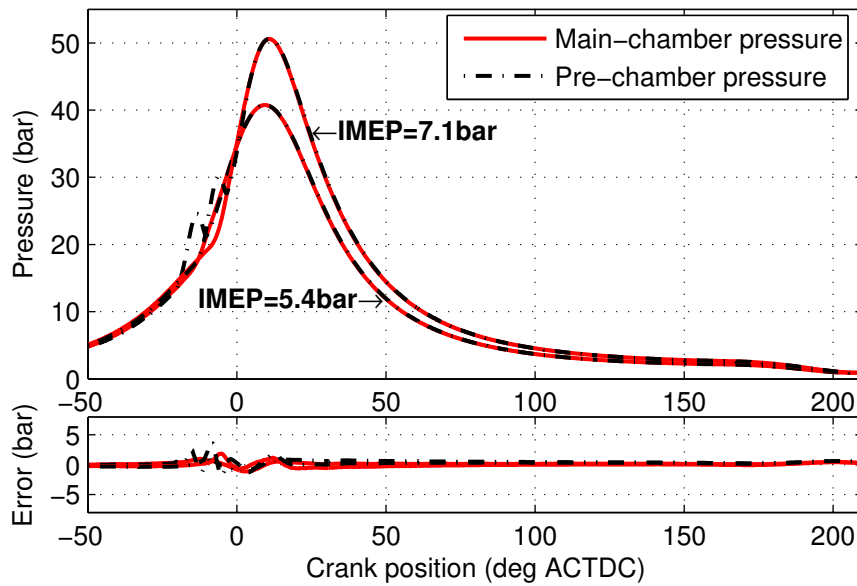


Figure 3.8: Pressure traces obtained at 1500 rpm.

Fig. 3.8 shows the simulation results at 1500 rpm with IMEP of 5.4 and 7.1 bar. These two operational conditions are marked in Fig. 3.7, where one is used for calibration and the other for model validation. The upper plot in Fig. 3.8 shows the pressure traces in the two combustion chambers obtained from the developed TJI engine model. The bottom plot shows the simulation errors. The error is always less than 1.8 bar and the relative error is less than 8%. This demonstrates that the developed TJI engine model is capable of capturing the TJI engine combustion characteristics.

Fig. 3.9 shows the heat release rates in the two combustion chambers during combustion. The upper plot shows the main-chamber NHR rates obtained from simulation (dashed line) and experiment (solid line). The experimental NHR is calculated from an inverse thermodynamic calculation [18, 22] based on the experimental pressure data. The dash-dot line is the coefficient $b(t)$ in Eqn. (3.24). The bottom plot shows the chemical energy release (CER) rates in the pre-chamber. The solid line is the CER from the fuel that vaporized immediately after injection. The dashed line is the CER coming from the fuel vaporized from the fuel film. This part of CER cannot increase rapidly before the main-chamber pressure is greater than the pre-chamber pressure, because the vaporized fuel in the burned zone in pre-chamber burns rapidly only after a large amount of air is

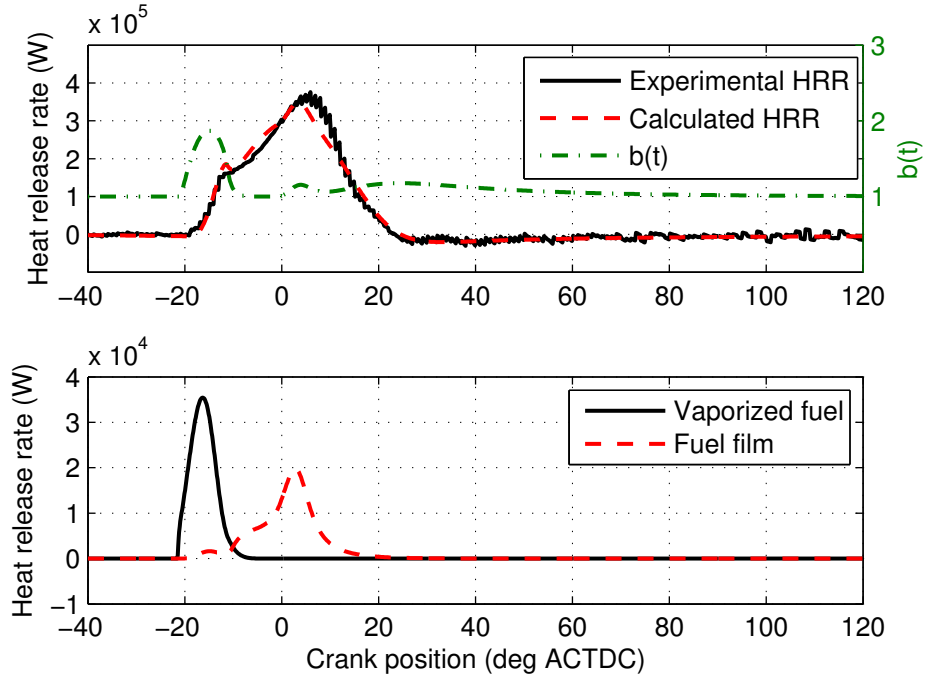


Figure 3.9: Heat release rates in two chambers.

pushed into the pre-chamber from the main-chamber. It can also be found that the main-chamber NHR rate is increased by the turbulent jets during the early stage (-20 to -10 deg ACTDC) and later stage (0 to 10 deg ACTDC) of the combustion, where $b(t) > 1$. And these turbulent jets are caused by the high CER rate in the pre-chamber at the corresponding two stages. In other words, without the pre-chamber fuel vaporization model, the main-chamber NHR rate in the simulation cannot match the experiment results. This confirms the necessity of the pre-chamber fuel vaporization model.

Fig. 3.10 presents the value of coefficient α_b in Eqn. (2.12); see the solid line. There are two switch points around -11 and 0 deg ACTDC on this line, corresponding to the two points when the mass flow between the two chambers changes its direction. The mass flow rate, \dot{m}_{tur} , is shown as the light colored dash-dot line. α_b is always smaller than the corresponding burned zone volume fraction, v_b , in the pre-chamber or in the main-chamber. This is consistent with the discussion in Section 3.5 that the burned gas is hard to flow through the orifice between the two chambers.

Fig. 3.11 shows the simulation results with different pre-chamber fuel injection amounts. In

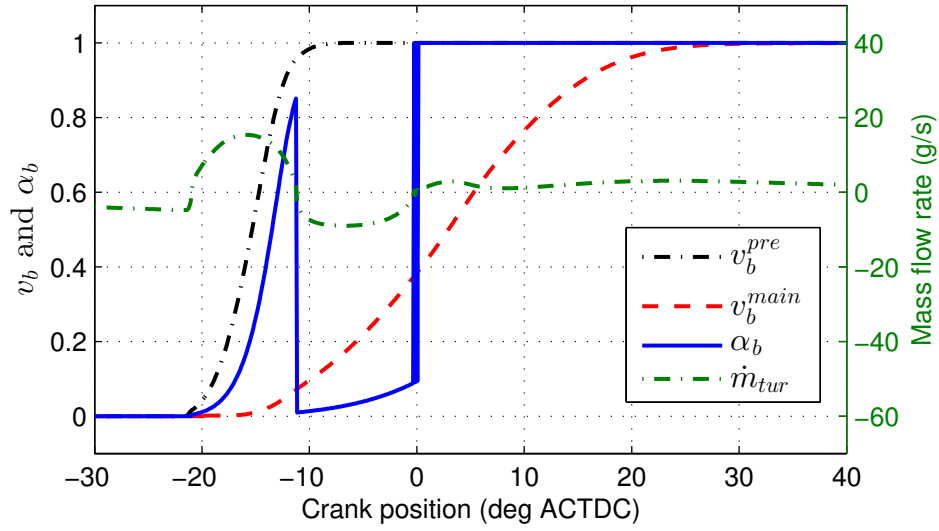


Figure 3.10: The value of α_b and other related parameters during simulation.

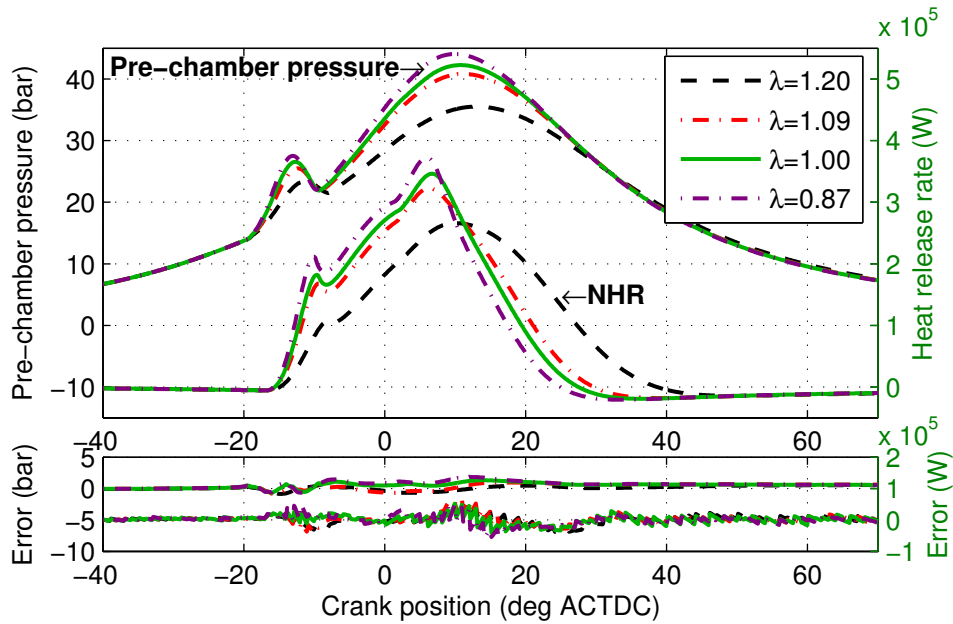


Figure 3.11: Pre-chamber pressure traces and main-chamber heat release rates for different pre-chamber λ .

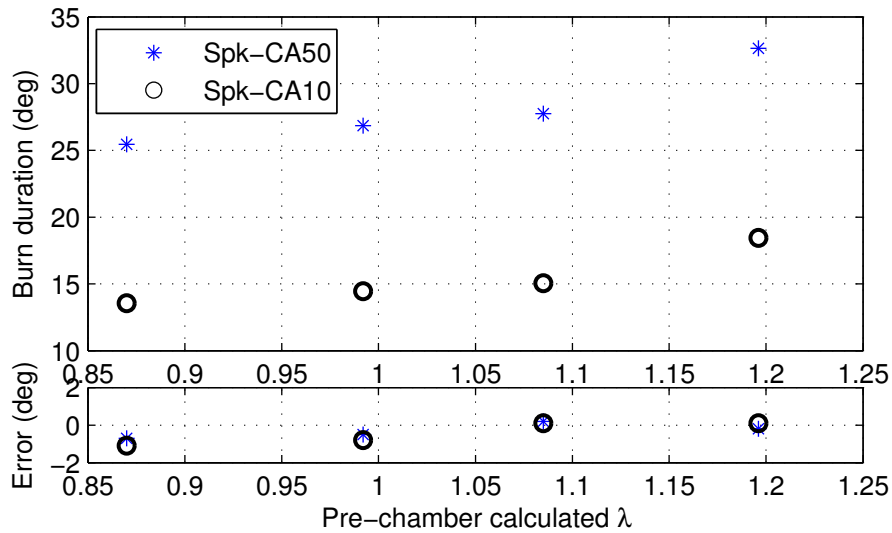


Figure 3.12: Main-chamber burn duration with the same main-chamber properties and different pre-chamber λ .

the upper plot, it can be found that the pre-chamber pressure rise is high for the case with rich pre-chamber AFR. High pressure rise generates the turbulent jets with large energy. Correspondingly, the NHR rate is also high for the case with small pre-chamber λ . This means that the main-chamber burn rate increases as the pre-chamber fuel injection quantity is increased. As the pre-chamber λ becomes smaller than 1, adding more fuel will not increase the main-chamber burn rate much since the pre-chamber is already very rich. This phenomenon can be shown more clearly in Fig. 3.12. The upper plot presents how the main-chamber burn duration from spark timing (Spk) to CA50, the crank angle when 50% of fuel is burned, is affected by the pre-chamber λ . The bottom plots in Fig. 3.11 and 3.12 show the simulation errors for each operational conditions. It can be found that the errors are within a fairly small range, which indicates the developed TJI engine model is able to simulate this unique phenomenon for the TJI combustion. This is very important because it means that the model has the potential to be used for developing the corresponding model-based control strategies using pre-chamber fuel injection to optimize the main-chamber combustion.

Fig. 3.13 compares the IMEPs obtained from the TJI engine model and those from the experiments with the validation operational conditions shown in Fig. 3.7. The two dash-dot lines on each side of the data points show where the 5% error is. All of the IMEPs calculated by the model match

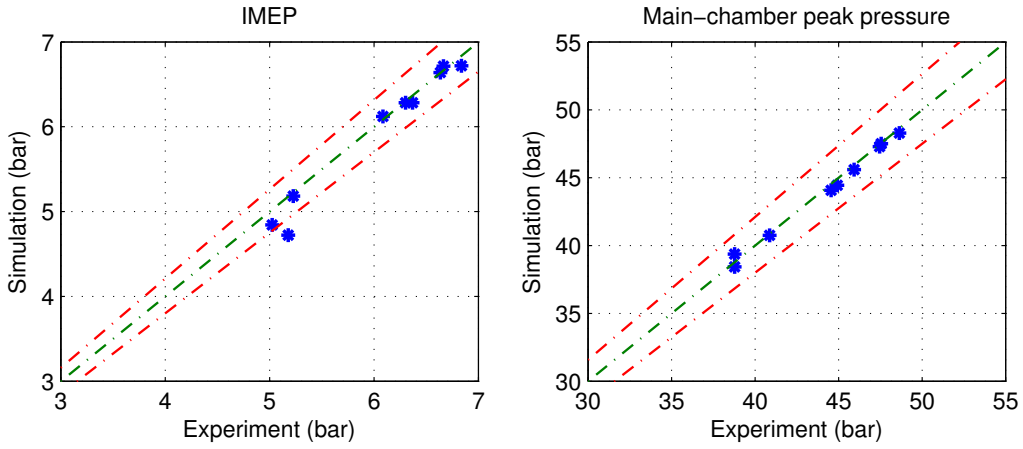


Figure 3.13: IMEP comparison between simulation and experimental results.

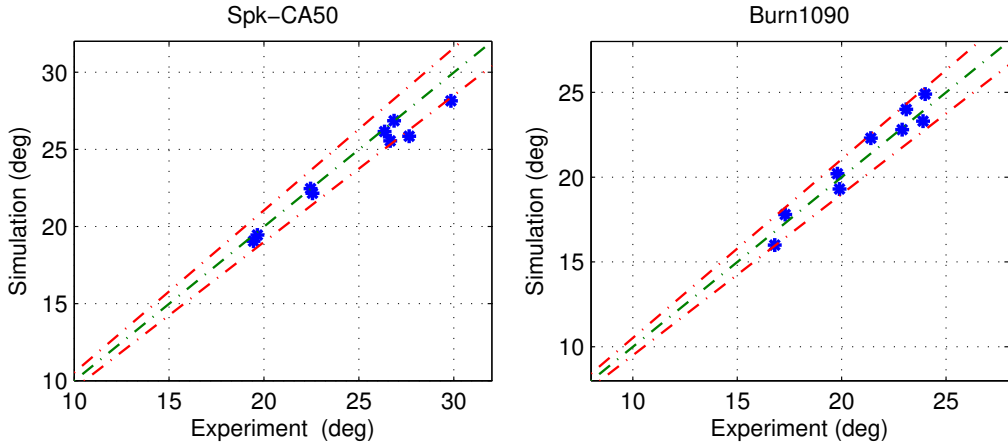


Figure 3.14: Spk-CA50 comparison between simulation and experimental results.

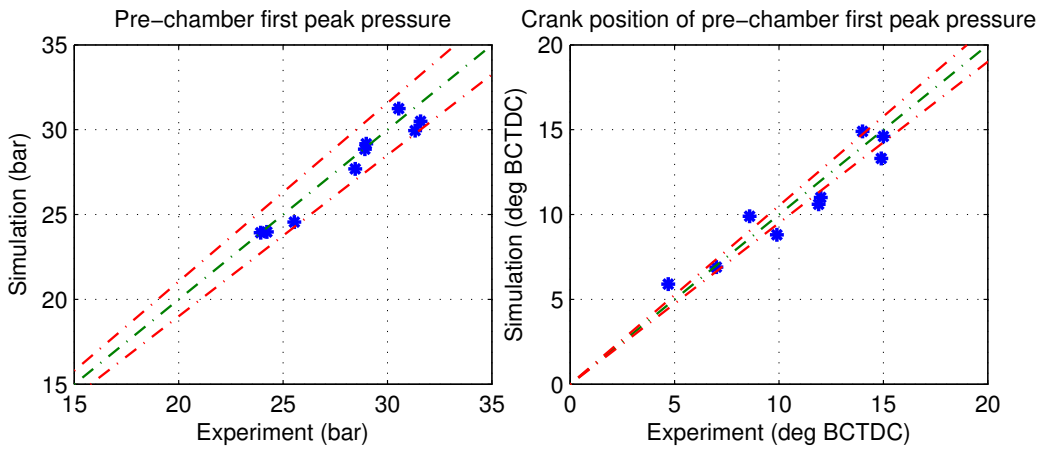


Figure 3.15: Pre-chamber first peak pressures and their crank positions.

the experimental results very well. To further validate the model, other pressure related variables of the main-chamber calculated by the model are compared with experimental results, including the burn duration from Spk to CA50, 10-90% burn duration (Burn1090) and peak pressure. Finally, Fig. 3.15 compares the experimental and simulation results of the first peak pressures in the pre-chamber (around 12 deg BCTDC in Fig. 3.11) and their points of occurrence (in crank position). It is seen that the TJI engine model is able to reproduce the experimental results very well.

3.7 Conclusions

A control-oriented combustion model is proposed for a single cylinder turbulent jet ignition (TJI) engine using liquid fuel for both combustion chambers. Several techniques are used to keep the developed model simple enough for real-time simulations with satisfactory accuracy. The model was calibrated using experimental data at engine speeds between 1200 and 2000 rpm with indicated mean effective pressure between 4.2 to 7.2 bar, and then, the calibrated model is validated using a set of data different from that used for calibration. The simulation and experimental results show a fairly good agreement. The simulation results also shows the effectiveness of the fuel vaporization model and the combustion model based on the proposed parameter-varying Wiebe function that models the coupling combustion effect between the pre- and main-chambers. In conclusion, the developed model is able to capture the TJI combustion characteristics in both chambers, especially the interaction between them. This indicates that the developed model can be used for developing the TJI engine control strategies that optimize both pre- and main-chamber control variables. Future work is to further validate and calibrate the model over the entire metal engine operational range.

CHAPTER 4

OPTIMAL COMBUSTION PHASING MODELING AND CONTROL OF A TURBULENT JET IGNITION ENGINE

4.1 Introduction

In recent years, improving the thermal efficiency of internal combustion (IC) engines becomes increasingly important for powertrain researchers and engineers [26]. According to the analysis based on 2015 EPA certification data, a further 30% reduction in fuel consumption is required for gasoline engines to meet the US 2025 GHG regulations, if the improvement is originated solely from IC engines [27].

TJI combustion is a promising combustion technology that is able to achieve low engine out emissions and high thermal efficiency. The application of the TJI combustion technology ranges from engines for passage cars to commercial vehicles, such as delivering trucks, and stationary power generator, with a thermal efficiency improvement of more than 25 percent[27]. Moreover, the TJI technology was even used in Ferrari's Formula One racing car [28]. The history of TJI engines can be traced back to the 1940s [14]. The TJI system mainly consists of three parts: a large main-chamber, a small pre-chamber (a few percent of main-chamber volume), and a single- or multi-orifice nozzle connecting the two combustion chambers. Once the pre-chamber is ignited, the pressure difference between the two sides of the nozzle drives the hot reacting products into the main-chamber. The hot reacting products from the pre-chamber are called turbulent jets. Since the turbulent jets contain significantly large ignition energy, the main-chamber can be ignited under ultra lean conditions. There are two major advantages for lean combustion. The first is the improvement of engine thermal efficiency. It is achieved by increasing the specific heat ratio of the air-fuel mixture inside the main-chamber with extra air [14]. Lean combustion can also reduce the NO_x (nitrogen oxides) formation due to the low combustion temperature [14]. Therefore, lean or diluted combustion attracts more researchers' attention as the regulations on NO_x emissions

become increasingly stringent [29].

Another factor that directly affects the engine thermal efficiency is the combustion phase [30]. Among several critical combustion phasing locations of interest, CA50 (crank location when 50% of fuel is burned) is of primary interest, and thus, is widely used for combustion phasing analysis and control [31]. The ignition timing associated with the most efficient combustion is called maximum break torque (MBT) timing that can be achieved by regulating the CA50 location to its optimum. Once the CA50 is far away from that location, the efficiency decreases and the combustion also becomes less stable, leading to high coefficient of variation (COV) of the indicated mean effective pressure (IMEP). Therefore, combustion phasing control is important for both conventional spark ignition (SI) and TJI engines.

Different methods have been used for combustion phasing control. Generally, these methods can be divided into two groups. The first focuses on finding the optimal combustion phase. For example, [32–34] use the extreme seeking control method to find the optimal spark timing and reference [35] uses an adaptive optimal control method similar to extreme seeking. The second group mainly focuses on combustion phase detection and use it for optimal combustion phase control. In reference [31], a combustion phasing model is developed based on an artificial neural network and used for closed loop control, reference [36] uses an adaptive control method based on a radial basis function network, and reference [37] utilizes the hypothesis test for combustion phasing control. Reference [38] developed an ionization based closed-loop combustion phase detection and control strategy. In this research, the optimal CA50 values under different engine operational conditions are derived from the developed engine model and is regulated at its optimal value through feedforward and feedback control. Different combustion phasing control methods have been developed for a various IC engines, but not for TJI engines. For TJI engines, besides spark timing, pre-chamber control variables can also affect the combustion phasing in the main-chamber. This makes the open-loop map-based controller less accurate, because the main-chamber combustion phasing is subject to the characteristics of turbulent jets from the pre-chamber. Therefore, model-based feedforward and feedback control are preferable. The increased number of control variables

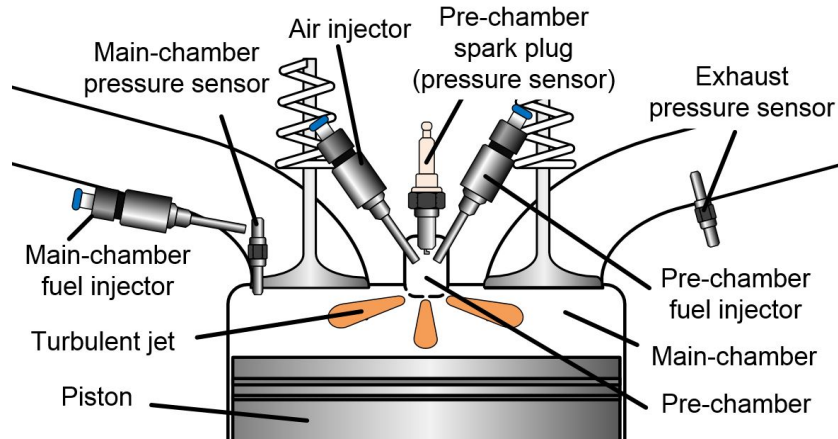


Figure 4.1: TJI engine architecture

makes the control problem more complicated, but they provide the additional degree of freedoms in control to improve the closed-loop system performance, which will be shown in the controller validation section of this chapter.

4.2 Target Engine Description and Specifications

Fig. 4.1 shows the basic architecture of the single cylinder Dual-Mode TJI (DM-TJI) engine studied in this paper. Each cylinder has two combustion chambers, pre and main ones. The pre-chamber is located on top of the main-chamber. Two chambers are connected through six small orifices between them. The engine has two fuel injectors, one for pre-chamber (see Fig. 3.1) and one for main-chamber in the intake port. A distinctive feature of this DM-TJI engine is the inclusion of an air injector in the pre-chamber. The air injector is located at the opposite side of the pre-chamber fuel injector. When air injector is turned on, the pressurized air is injected against the fuel jets to reduce the amount of fuel deposited on the pre-chamber wall. More importantly, the air injector is also used to control the air-to-fuel ratio (AFR) in the pre-chamber to be close to stoichiometry and to improve the pre-chamber combustion characteristics, especially under heavy exhaust-gas-recirculation. For TJI engines, the combustion is firstly initiated in the pre-chamber by the spark plug, and then the hot reacting products in the pre-chamber are pushed into the main-chamber through the connecting orifices between two chambers and ignite the lean mixture in the

main-chamber. The engine specifications are listed in Table 3.1. Both chambers use EPA LEV-II liquid gasoline.

4.3 Nonlinear State-Space TJI Engine Model

During engine operation, the combustion in the current engine cycle is influenced by the residual gas from the previous cycle. For the TJI engine discussed in this article, the fuel film left from the previous cycle on the pre-chamber also influences the combustion during the current cycle. These are the sources of the engine cycle-to-cycle dynamics. The states of the state-space engine model thus need to describe the properties of the residual gas in both chambers and the fuel film on the pre-chamber wall. Fig. 4.2 shows how the state-space engine model is developed. The whole engine cycle is divided into several different stages for each state. The state-space equations can be obtained by combining the governing equations of each stage. The details of the governing equations for each stage is presented in the next subsections.

4.3.1 Main-chamber state-space model

The major assumptions for developing the main-chamber state-space model are:

1. Because the combustion in the main-chamber is always lean, it is assumed that there is no unburned fuel left after the combustion.
2. The intake and exhaust manifold pressures, P_{Int} and P_{Exh} are assumed to be equal to the main-chamber pressures at IVC and EVC, P_{EVC}^{main} and P_{IVC}^{main} , respectively.
3. The mass of the gas inside the main-chamber is assumed to be constant when both the intake and exhaust valves are closed.

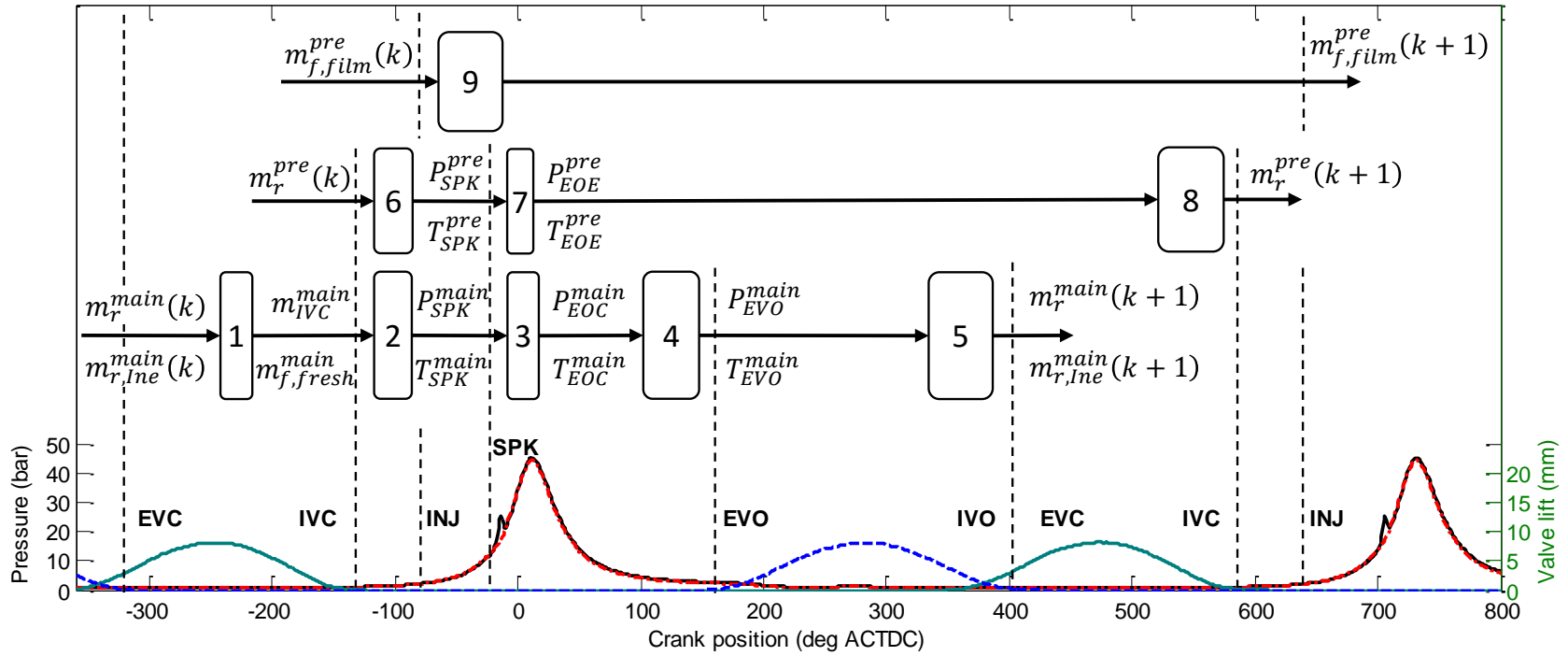


Figure 4.2: State-space TJI engine model architecture.

According to the above two assumptions, the properties of the residual gas in the main-chamber can be fully described by the following two states:

1. The mass of inert gas left from last cycle at EVC: $m_{r,Ine}^{main}(k)$. Here, k represents the engine cycle index.
2. The mass of residual gas left from last cycle at EVC: $m_r^{main}(k)$

From EVC to IVC, the volume occupied by residual gas changes a little due to the pressure change from P_{EVC}^{main} to P_{IVC}^{main} .

$$V_r^{main}(k) = V_{EVC}^{main} \left(\frac{P_{EVC}^{main}(k)}{P_{IVC}^{main}(k)} \right)^{1/n} \quad (4.1)$$

where V_{EVC}^{main} is the main-chamber volumes at EVC and IVC, respectively; n is the polytropic index.

The volume of the fresh air-fuel mixture flowing into the main-chamber then can be calculated accordingly:

$$V_{fresh}^{main}(k) = V_{IVC}^{main} - V_{EVC}^{main} \left(\frac{P_{EVC}^{main}(k)}{P_{IVC}^{main}(k)} \right)^{1/n} \quad (4.2)$$

The mass of the fresh air-fuel mixture and the average in-cylinder temperature can be calculated by ideal gas law:

$$m_{fresh}^{main}(k) = \frac{P_{IVC}^{main}(k) V_{fresh}^{main}(k)}{RT_{Int}(k)} \quad (4.3)$$

$$T_{IVC}^{main}(k) = \frac{P_{IVC}^{main}(k) V_{IVC}^{main}}{m_{IVC}^{main}(k) R} \quad (4.4)$$

where R is the gas constant and m_{IVC}^{main} is the total mass inside the main-chamber at IVC:

$$m_{IVC}^{main}(k) = m_r^{main}(k) + m_{fresh}^{main}(k) \quad (4.5)$$

The mass of the fresh fuel flowing into the main-chamber can be calculated based on intake manifold AFR, ϕ_{Int} :

$$m_{f,fresh}^{main}(k) = m_{fresh}^{main}(k) \frac{1}{\phi_{Int}(k) + 1} \quad (4.6)$$

During the compression, combustion and expansion processes, the mass of the gas inside the main-chamber is a constant. The temperature during combustion can be simplified to be a combination of polytropic process and heat release process [39]. Therefore, the temperature at end of combustion (EOC) can be represented by:

$$T_{EOC}^{main}(k) = T_{IVC}^{main}(k) \left(\frac{V_{IVC}^{main}}{V_{EOC}^{main}(k)} \right)^{n-1} + \frac{Q_{LHV} m_{f,fresh}^{main}(k)}{m_{IVC}^{main}(k) C_v} \quad (4.7)$$

And P_{EOC}^{main} can be calculated based on ideal gas law.

The crank angle position at EOC, θ_{EOC} , can be obtained by first substituting $x_b(\theta_{EOC}) = 0.9$ into the first equation in Eqn. (3.24):

$$\frac{\theta_{EOC} - \theta_{ign_b}}{\Delta\theta_d} = \left(-\frac{\ln(0.1)}{a} \right)^{\frac{1}{m+1}} = Sol \quad (4.8)$$

Then by using the second equation in Eqn. (3.24) and Eqn. (3.26), θ_{EOC} can be calculated by:

$$\begin{aligned} \theta_{EOC} &= \theta_{ign} + \Delta\theta_d \cdot Sol - \int_{\theta_{ign}}^{\theta_{EOC}} \beta \dot{m}_{tur}(\theta) d\theta \\ &= \theta_{ign} + \Delta\theta_d \cdot Sol - \beta m_{tur} \end{aligned} \quad (4.9)$$

where θ_0 can be approximated by spark timing, and the total mass of the turbulent jet during combustion, m_{tur} , will be calculated in the next subsection.

After combustion, the total mass of the inert gas can be calculated by:

$$m_{EOC,Ine}^{main}(k) = m_{r,Ine}^{main}(k) + m_{f,fresh}^{main}(k)(1 + AFRs) \quad (4.10)$$

where $AFRs$ is the stoichiometric AFR. After the combustion, the gas in the main-chamber polytropically expands to EVO:

$$T_{EVO}^{main}(k) = T_{EOC}^{main}(k) \left(\frac{V_{EOC}^{main}(k)}{V_{EVO}^{main}} \right)^{n-1} \quad (4.11)$$

And P_{EVO}^{main} can be calculated by the ideal gas law. After EVO, the gas in the main-chamber expands until its pressure is equal to the exhaust manifold pressure.

$$T_{EVC}^{main}(k) = \left(\frac{P_{EVC}^{main}(k)}{P_{EVO}^{main}(k)} \right)^{\frac{n-1}{n}} T_{EVO}^{main}(k) \quad (4.12)$$

where P_{EVC}^{main} can be approximated by P_{Exh} .

P_{IVO}^{main} can be approximated by P_{Exh} . Then the mass of residual gas in the main-chamber can be calculated by:

$$m_{IVO}^{main}(k+1) = \frac{P_{Exh}(k+1)V_{IVO}^{main}}{R\left[\left(\frac{P_{IVO}^{main}(k)}{P_{EVO}^{main}(k)}\right)^{\frac{n-1}{n}} T_{EVO}^{main}(k)\right]} \quad (4.13)$$

From IVO to EVC, part of the gas in the exhaust manifold flows back into the engine cylinder due to the pressure difference between intake and exhaust manifolds. This part of the residual gas is calculated based on the widely used Fox model[40].

$$m_{backflow}^{main}(k+1) = C_1 \frac{OF}{\Omega} \left(\frac{P_{Int}}{P_{Exh}}\right)^{-0.87} \sqrt{|P_{Int} - P_{Exh}|} m_{IVC}^{main}(k+1) \quad (4.14)$$

Since $m_{IVC}^{main}(k+1)$ cannot be determined without knowing the mass of residual gas, its value is approximated by

$$m_{IVC}^{main}(k+1) = \frac{P_{IVC}^{main}(k+1)V_{IVC}^{main}}{RT_{Int}(k+1)} \quad (4.15)$$

Then the mass of residual gas left for next cycle can be calculated by:

$$m_r^{main}(k+1) = \frac{P_{EVC}^{main}(k+1)V_{EVC}^{main}}{RT_{EVC}^{main}(k)} \quad (4.16)$$

The content in the residual gas is the same as that at EOC. Therefore, the inert gas left for the next cycle can be calculated by:

$$m_{r,Ine}^{main}(k+1) = m_r^{main}(k+1) \frac{m_{EOC,Ine}^{main}(k)}{m_{IVC}^{main}(k)} \quad (4.17)$$

4.3.2 Pre-chamber state-space model

In the pre-chamber, the AFR of the air-fuel mixture is always kept close to or richer than stoichiometry. Therefore, there is usually no air left after combustion in the pre-chamber. There might be some vaporized fuel left in the residual gas inside the pre-chamber, but its amount is very small

compared with the fuel amount from vaporization and injection. The mass of the fuel film on the pre-chamber wall is also very important because it determines how much fuel will vaporize into the gas mixture before ignition. As a result, the states selected for pre-chamber are:

1. The mass of inert gas left from last cycle at IVC: $m_r^{pre}(k)$.
2. The mass of fuel film on the pre-chamber wall at IVC: $m_{f,film}^{pre}(k)$

Before IVC, the gas flow through the orifice connecting the two chambers mainly goes from the pre-chamber to the main-chamber. Therefore, the gas mixture in the pre-chamber is mainly the residual gas left from last cycle. At IVC, it is assumed that:

$$P_{IVC}^{pre} = P_{IVC}^{main} = P_{Int} \quad (4.18)$$

where P_{IVC}^{pre} is the pre-chamber pressure at IVC.

During the compression stroke, the residual gas in pre-chamber is compressed from P_{IVC}^{pre} , V^{pre} to P_{SPK}^{pre} , $V_{r,SPK}^{pre}$. Here, it is assumed that P_{SPK}^{pre} is the same as P_{SPK}^{main} . The mass of the residual gas m_r^{pre} keep unchanged.

$$V_{r,SPK}^{pre}(k) = \left(\frac{P_{Int}(k)}{P_{SPK}^{main}(k)} \right)^{1/n} V^{pre} \quad (4.19)$$

where the subscript SPK denotes the properties at spark timing and V^{pre} is the pre-chamber volume. Then T_{r-SPK}^{pre} can be obtained from ideal gas law.

The volume and mass of the gas coming from the main-chamber at SPK can be then calculated by the following equations:

$$V_{main,SPK}^{pre}(k) = V^{pre} - V_{r,SPK}^{pre}(k) - V_{inj}^{pre}(k) \quad (4.20)$$

where V_{inj}^{pre} is the total volume of the injected air and vaporized fuel. And $m_{main,SPK}^{pre}$ can be then calculated.

The average temperature in pre-chamber at SPK is:

$$T_{SPK}^{pre}(k) = \frac{P_{SPK}^{pre}(k)V^{pre}}{m_{SPK}^{pre}(k)R} \quad (4.21)$$

$$m_{SPK}^{pre}(k) = m_{inj}^{pre}(k) + m_r^{pre}(k) + m_{main,SPK}^{pre}(k) \quad (4.22)$$

where m_{inj}^{pre} is the total mass of the injected air and vaporized fuel in pre-chamber.

The combustion in the pre-chamber is very fast, so a constant volume combustion is used to approximate the combustion process:

$$T_{EOC}^{pre}(k) = T_{SPK}^{pre}(k) + \frac{m_{fuel,vap}^{pre}(k) \cdot Q_{LHV}}{m_{SPK}^{pre}(k) C_v} \quad (4.23)$$

$$P_{EOC}^{pre}(k) = \frac{m_{SPK}^{pre}(k) R T_{EOC}^{pre}(k)}{V^{pre}} \quad (4.24)$$

where $m_{fuel,vap}^{pre}$ is the total vaporized fuel in the pre-chamber.

Then the gas in the pre-chamber expands until its pressure is similar to the main-chamber pressure. This time is defined as end of expansion (EOE).

$$T_{EOE}^{pre}(k) = \left(\frac{P_{EOE}^{main}(k)}{P_{EOC}^{pre}(k)} \right)^{\frac{n-1}{n}} T_{EOC}^{pre}(k) \quad (4.25)$$

If SPK is controlled around the optimum value, P_{EOE}^{main} can be approximated by the pressure at top dead center when motoring the engine. Then the mass at EOE, m_{EOE}^{pre} can be calculated by ideal gas law. The mass flow rate of the turbulent jet after EOE is usually very small, so m_{tur} in Eqn. (4.9) can be calculated by:

$$m_{tur}(k) = m_{SPK}^{pre}(k) - m_{EOE}^{pre}(k) \quad (4.26)$$

After EOE, it is assumed that all the gas pushed into pre-chamber does not mix with the gas in pre-chamber and then was pushed out as main-chamber pressure decrease. Therefore, the gas in the pre-chamber is first polytropically compressed and then expands to IVC.

$$T_{IVC}^{pre}(k+1) = \left(\frac{P_{IVC}^{main}(k+1)}{P_{EOC}^{pre}(k)} \right)^{\frac{n-1}{n}} T_{EOC}^{pre}(k) \quad (4.27)$$

The mass of the residual gas can then be calculated based on the ideal gas law.

$$m_r^{pre}(k+1) = \frac{P_{Int}(k+1) V^{pre}}{R T_{IVC}^{pre}(k+1)} \quad (4.28)$$

The fuel film on the pre-chamber wall keeps vaporizing during the entire engine cycle. The vaporization rate is shown in Eqn. (3.14). The mass of the fuel film after pre-chamber fuel injection can be expressed by:

$$\dot{m}_{f, \text{film}}^{\text{pre}}(t) = -\frac{m_{f, \text{film}}^{\text{pre}}(t)}{\delta_f \rho_f} M_f h_m \frac{P_{s0}}{R_m T_f(t)} e^{-\frac{\Delta H}{R_m T_f(t)}} \quad (4.29)$$

Here, $T_f(t)$ is approximated by $a_t(T_{EOC}^{\text{pre}} + T_{IVC}^{\text{pre}})$, where a_t is a calibration parameter. The initial value of $m_{f, \text{film}}^{\text{pre}}(t)$, that is the fuel film mass right after the fuel injection, is:

$$m_{f, \text{film}}^{\text{pre}}(0) = m_{f, \text{film}}^{\text{pre}}(k) + m_{inj, w}^{\text{pre}}(k) \quad (4.30)$$

where $m_{f, \text{film}}^{\text{pre}}(k)$ is the fuel film mass right before the fuel injection in engine cycle k , and $m_{inj, w}^{\text{pre}}(k)$ is the mass of the injected fuel shooting on the wall.

Then, the mass of the fuel film right before fuel injection during the next engine cycle can be calculated by solving Eqn. (4.29).

$$m_{f, \text{film}}^{\text{pre}}(k+1) = \left[m_{f, \text{film}}^{\text{pre}}(k) + m_{inj, w}^{\text{pre}}(k) \right] e^{-a_{vap} \Delta t(\Omega)} \quad (4.31)$$

where $\Delta t(\Omega)$ is the time duration of each engine cycle, Ω is engine speed, and a_{vap} is:

$$a_{vap} = \frac{M_f h_{m, ss}}{\delta_f \rho_f} \frac{P_{s0}}{R_m T_f} e^{-\frac{\Delta H}{R_m T_f}} \quad (4.32)$$

where $h_{m, ss}$ replaced h_m in Eqn. (4.29) as a calibration parameter in the state-space model.

4.3.3 CA50 calculation

The parameter, $\Delta\theta_d$, in Eqn. (4.9) is mainly determined by the main-chamber gas properties. According to the experiment results, $\Delta\theta_d$ can be approximated by a linear function of P_{Int} , Ω , λ and x_{CSP}^{main} , where λ is the normalized air-fuel ratio in the main-chamber and x_{CSP}^{main} is the main-chamber CSP mass fraction at IVC. Then, θ_{CA50} can be finally obtained by

$$\begin{aligned} \theta_{CA50} = & \theta_{SPK} + \Delta\theta_0 + a(P_{Int} - P_{Int0}) + b(\Omega - \Omega_0) \\ & + c(\lambda - \lambda_0) + d(x_{CSP}^{\text{main}} - x_{CSP0}^{\text{main}}) + e(m_{tur} - m_{tur0}) \end{aligned} \quad (4.33)$$

where the parameters, P_{Int0} , Ω_0 , λ_0 , x_{CSP0}^{main} , and m_{tur0} , represent the nominal operational values.

A linear least-square fitting process is used to determine the unknown parameters, $\Delta\theta_0$, a , b , c , d and e , in Eqn. 4.33. Here, the following vectors are defined: $P = [\Delta\theta_{d0}, a, b, c, d, e]^T$ is the parameter vector; $y_j = [\theta_{CA50} - \theta_{ign}]$; and $x_j = [1, P_{Int} - P_{Int0}, \Omega - \Omega_0, \lambda - \lambda_0, x_{CSP}^{main} - x_{CSP0}^{main}, m_{tur} - m_{tur0}]^T$. and the least-square method calculates the parameter vector that minimize the following expression using N data points.

$$\sum_{j=1}^N (y_j - x_j * P)^2 \quad (4.34)$$

where j is data point index. The solution of the problem is

$$P = (X^T * X)^{-1} X^T * Y \quad (4.35)$$

where the rows of X and Y are x_j^T and y_j respectively. Then the parameters, $\Delta\theta_{d0}$, a , b , c , d and e , can be obtained.

Considering all the equations above, we finally got the nonlinear state-space equation in the following form.

$$\begin{aligned} x(k+1) &= f[x(k), u(k)] \\ y(k) &= h[x(k), u(k)] \end{aligned} \quad (4.36)$$

where the function f and h are shown in the Appendix A, $x(k)$ is the state vector; $u(k)$ is the control input vector; and $y(k)$ is the output vector defined below.

$$\begin{aligned} x(k) &= [m_r^{pre}(k), m_{f, film}^{pre}(k), m_r^{main}(k), m_{r, CSP}^{main}(k)]^T \\ u(k) &= [\theta_{SPK}(k), m_{inj, fuel}^{pre}(k), m_{inj, air}^{pre}(k), m_{fuel}^{main}(k), P_{Int}, \Omega(k)]^T \\ y(k) &= [\theta_{CA50}(k)]. \end{aligned} \quad (4.37)$$

where Ω is engine speed.

4.4 Controller Development

It can be found that the burn duration in the main-chamber is determined by the gas properties in both combustion chambers. In other words, the CA50 can be controlled by spark timing and other

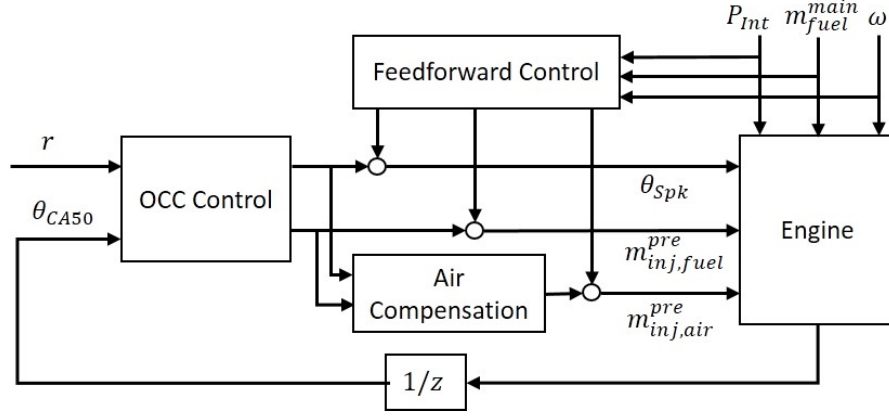


Figure 4.3: Control system architecture.

variables in the pre-chamber. In this paper, three variables are used to control the main-chamber CA50. They are spark timing, θ_{SPK} ; pre-chamber fuel and air injection amounts, $m_{inj,fuel}^{pre}$ and $m_{inj,air}^{pre}$. The other parameters, $m_{fuel}^{main}(k)$, $P_{Int}(k)$ and $\Omega(k)$, are considered as disturbances. Fig. 4.3 shows the basic architecture of the control system. The feedforward controller is a model-based controller. The feedback controller uses output constraint control method to regulate the CA50 to the desired value. The main-chamber AFR is controlled by the main-chamber fuel injector using a map-based feedforward control as a function of intake manifold pressure.

4.4.1 Feedforward control

The feedforward controller calculates the value of pre-chamber air and fuel injection amounts and spark timing based on $m_{fuel}^{main}(k)$, $P_{Int}(k)$ and $\Omega(k)$. The pre-chamber air injection quantity is determined by a pre-calibrated map. The pre-chamber fuel injection quantity and spark timing is obtained by solving

$$\begin{cases} \lambda_{SPK}^{pre} = 1 \\ \theta_{CA50} = \theta_{CA50,desired} \end{cases} \quad (4.38)$$

where λ_{SPK}^{pre} is the normalized air-fuel ratio in the pre-chamber at spark timing. The detailed expression of these equations can be easily obtained based on the discussion in Section III, as

follows

$$\left\{ \begin{aligned} & \frac{\frac{m_{IVC}^{main} - m_{fuel}^{main} - m_{r,CSP}^{main}}{m_{IVC}^{main}} m_{main,SPK}^{pre} + m_{inj,air}^{pre}}{\varphi_s} = \\ & \frac{m_{fuel}^{main}}{m_{IVC}^{main}} m_{main,SPK}^{pre} + (1-k)m_{inj,fuel}^{pre} + \dot{m}_{f,vap}^{pre} \Delta\theta_{SPK} \\ & + (m_{f,fil}^{pre} + m_{inj,w}^{pre}) [1 - \exp(-a_{vap} \Delta\theta_{SPK0})] \\ & \theta_{CA50}^{desired} = \theta_{SPK} + \Delta\theta_0 + a(P_{Int} - P_{Int0}) + b(\Omega - \Omega_0) \\ & + c(\lambda - \lambda_0) + d(x_{CSP}^{main} - x_{CSP0}^{main}) - e\{m_{tur0} - m_{Spk}^{pre} [1 \\ & - (\frac{P_{EOE}^{pre} V^{pre}}{R})^{\frac{1}{n}} (m_{Spk}^{pre} T_{Spk}^{pre} + \frac{m_{fuel,vap}^{pre} Q_{LHV}}{C_v})^{-\frac{1}{n}}]\} \end{aligned} \right. \quad (4.39)$$

where

$$m_{SPK}^{pre} = m_r^{pre} + m_{inj}^{pre} + m_{main,SPK}^{pre} \quad (4.40)$$

Since Eqn. (4.38) is a highly nonlinear equation of $m_{inj,fuel}^{pre}$ and θ_{SPK} , it is difficult to solve the equations analytically. Numerical methods can be used, but the computational effort would be too large for real time engine control. By investigating Eqn. (4.38), it can be found that there are only two highly nonlinear terms that are functions of the two unknown variables. The other terms can be determined once the feedforward control inputs and $m_{inj,air}^{pre}$ are given. The two terms are

$$\left\{ \begin{aligned} & m_{main,SPK}^{pre} = f_1(P_{Int}, m_{inj,air}^{pre}, \theta_{SPK}) \\ & (m_{Spk}^{pre} T_{Spk}^{pre} + \frac{m_{fuel,vap}^{pre} Q_{LHV}}{C_v})^{-\frac{1}{n}} = f_2(P_{Int}, m_{inj,air}^{pre}, m_r^{pre}, m_{inj,fuel}^{pre}, \theta_{SPK}) \end{aligned} \right. \quad (4.41)$$

since the expression of f_1 and f_2 can be easily derived based on results in Section III, thus will not be shown here. Then, $m_{inj,fuel}^{pre}$ and θ_{SPK} can be solved for any desired θ_{CA50} by replacing the two terms with their linear approximation

$$\left\{ \begin{aligned} & f_1 = \frac{\partial f_1}{\partial \theta_{SPK}} (\theta_{SPK} - \theta_{SPK0}) + f_1(\theta_{SPK0}) \\ & f_2 = \frac{\partial f_2}{\partial \theta_{SPK}} (\theta_{SPK} - \theta_{SPK0}) + \frac{\partial f_2}{\partial m_{inj,fuel}^{pre}} (m_{inj,fuel}^{pre} - m_{inj,fuel0}^{pre}) + f_2(m_{inj,fuel0}^{pre}, \theta_{SPK0}) \end{aligned} \right. \quad (4.42)$$

The values of m_r^{pre} and m_{CSP}^{main} come from the state estimator in the feedback controller.

The pre-chamber AFR needs to be maintained around the stoichiometry for good ignitability and stable combustion in the pre-chamber. For the same main-chamber condition, the AFR in the pre-chamber is determined by all three control inputs, but only two are independent. If two of them are given, the remaining one can be calculated according to the first equation in Eqn. (4.38). As a result, $m_{inj,air}^{pre}$ is not used by feedback controller but calculated based on the other two controller outputs, θ_{SPK} and $m_{inj,fuel}^{pre}$, in the 'Air Compensation' block of Fig. 4.3.

4.4.2 Output covariance constraint control

The nonlinear state-space engine model was first linearized by Matlab around the operational condition with IMEP=6 bar, $\lambda=1.85$, and $\Omega=1500$ rpm. The linearized TJI engine model can be expressed as

$$\begin{aligned}\tilde{x}(k+1) &= \tilde{A}\tilde{x}(k) + \tilde{B}\tilde{u}(k) + \tilde{G}\tilde{w}(k) \\ \tilde{y}(k) &= \tilde{C}\tilde{x}(k) + \tilde{D}\tilde{u}(k) + \tilde{H}\tilde{w}(k) + \tilde{v}(k)\end{aligned}\tag{4.43}$$

where $\tilde{u}(k) = [\tilde{\theta}_{SPK}(k), \tilde{m}_{inj,fuel}^{pre}(k)]^T$ is the control input; and $\tilde{w}(k) = [\tilde{m}_{fuel}^{main}(k), \tilde{P}_{Int}(k), \tilde{\Omega}(k)]^T$ is considered as disturbance. The parameter with the overhead tilde denotes the deviation of the corresponding parameter from its reference value, for example, $x(k) = x_0(k) + \tilde{x}(k)$, given $x_0(k)$ the reference value around which the model is linearized.

For the current control hardware, the value of CA50 needs one engine cycle to compute and transmit to the engine controller. Therefore, the measured CA50 is delayed by one engine cycle, resulting one more state,

$$x_d(k+1) = \tilde{y}(k),\tag{4.44}$$

Accordingly, the actual plant model is

$$\begin{aligned}x_p(k+1) &= A_px_p(k) + B_pu(k) + G_pw_p(k) \\ y_p(k) &= C_px_p(k) + v_p(k)\end{aligned}\tag{4.45}$$

where

$$\begin{aligned} A_p &= \begin{bmatrix} \tilde{A} & 0^{4 \times 1} \\ \tilde{C} & 0 \end{bmatrix}, B_p = \begin{bmatrix} \tilde{B} \\ \tilde{D} \end{bmatrix}, \\ G_p &= \begin{bmatrix} \tilde{G} & 0^{4 \times 1} \\ \tilde{H} & 1 \end{bmatrix}, C_p = \begin{bmatrix} 0^{1 \times 4} & 1 \end{bmatrix} \end{aligned} \quad (4.46)$$

and the augmented state vector and the disturbance input vector are

$$x_p(k) = \begin{bmatrix} \tilde{x}(k) \\ x_d(k) \end{bmatrix}, w_p(k) = \begin{bmatrix} \tilde{w}(k) \\ \tilde{v}(k) \end{bmatrix}. \quad (4.47)$$

The controller is designed so that the CA50 tracks the desired value $r(k)$. The tracking error is defined as

$$e(k) = r(k) - y_p(k). \quad (4.48)$$

To eliminate the steady-state tracking error, an integral action is introduced by defining the integration of the tracking error as

$$e_i(k+1) = e_i(k) + T_s e(k). \quad (4.49)$$

For simplicity, T_s is set to 1. The augmented state vector $x_i(k) = \begin{bmatrix} x_p(k), e_i(k) \end{bmatrix}^T$ leads the following augmented state equation

$$\begin{aligned} x_i(k+1) &= A_i x_i(k) + B_i u_i(k) + d r(k) + G_i w_i(k) \\ y_i(k) &= C_i x_i(k) \\ z_i(k) &= M_i x_i(k) + v_i(k) \end{aligned} \quad (4.50)$$

where

$$\begin{aligned} A_i &= \begin{bmatrix} A_p & 0^{5 \times 1} \\ -C_p & 1 \end{bmatrix}, B_i = \begin{bmatrix} B_p \\ 0 \end{bmatrix}, d = \begin{bmatrix} 0^{5 \times 1} \\ 1 \end{bmatrix} \\ G_i &= \begin{bmatrix} G & 0^{5 \times 1} \\ 0 & 1 \end{bmatrix}, C_i = \begin{bmatrix} 0^{1 \times 5} & 1 \\ C_p & 0 \end{bmatrix} \end{aligned} \quad (4.51)$$

and the vector $z_i(k)$ is the noisy measurements of $y_i(k)$. Therefore, $M_i = C_i$.

Suppose that the plant is controlled by a strictly proper output feedback stabilizing control law given by

$$\begin{aligned}x_c(k+1) &= A_c x_c(k) + F z_i(k) \\ u_i(k) &= K_c x_c(k) + K_r r(k)\end{aligned}\tag{4.52}$$

Then, the closed-loop system becomes

$$\begin{aligned}x(k+1) &= Ax(k) + D_r r(k) + Dw(k) \\ y_i(k) &= Cx(k) \\ u_i(k) &= C_u x(k) + K_r r(k)\end{aligned}\tag{4.53}$$

where $x(k) = \begin{bmatrix} x_i(k) \\ x_c(k) \end{bmatrix}$, $w(k) = \begin{bmatrix} w_i(k) \\ v_i(k) \end{bmatrix}$. The closed-loop system matrices A , C , D , and D_r can be easily obtained based upon the above equations.

Consider the closed-loop system above. Let W_i and V_i denote positive symmetric matrices with dimension compatible to the process noise w_i and v_i . Defined $W = \text{block diag} \begin{bmatrix} W_i & V_i \end{bmatrix}$ and X the closed-loop controllability Gramian from the weighted disturbance input $W^{-1/2}w$. Since A is stable, X is the positive semi-definite solution of the following Lyapunov equation

$$X = AXA^T + DWD^T.\tag{4.54}$$

Rewrite the performance output vector y_i into $y_i := \begin{bmatrix} y_1 \\ y_2 \end{bmatrix}$, where $y_j = C_j x$ for $j = 1, 2$.

Then, the OCC problem is to find a output feedback controller for the plant that minimizes the OCC cost

$$J_{OCC} = \text{trace } RC_u X C_u^T, R > 0,\tag{4.55}$$

subject to the output covariance constraints

$$Y_j = C_j X C_j^T < \bar{Y}_j, j = 1, 2,\tag{4.56}$$

where $\bar{Y}_j > 0$ ($j = 1, 2$) are given.

The OCC problem is actually a linear quadratic (LQ) control problem with a special choice of output-weighting matrix Q . The value of Q is obtained by the iteration algorithm proposed in [41].

According to [42] and [41], the feedback controller is in the following form.

$$\begin{aligned}x_c(k+1) &= (A_i + B_i K_c - F M_p) x_c(k) + F z_i(k) \\ u_i(k) &= K_c x_c(k) + K_r r(k)\end{aligned}\tag{4.57}$$

Note that

$$F = A_i K M_i^T (V + M_i K M_i^T)^{-1},\tag{4.58}$$

where K is the solution to the algebraic Riccati equation

$$K = A_i [K - K M_i^T (V_i + M_i K M_i^T)^{-1} M_i K] A_i^T + D_i W_i D_i^T;\tag{4.59}$$

control gain K_c is provided by

$$K_c = -(R + B_i^T S B_i)^{-1} B_i^T S A_i,\tag{4.60}$$

where S is the solution to the algebraic Riccati equation

$$S = A_i^T [S - S B_i (B_i^T S B_i + R)^{-1} B_i^T S] A_i + C_i^T Q C_i;\tag{4.61}$$

and

$$K_r = (B_i^T S B_i + R)^{-1} B_i^T F_1,\tag{4.62}$$

where

$$F_1 = -[I - A_i^T + A_i^T S F_3 F_2]^{-1} A_i^T S F_3 F_2 d\tag{4.63}$$

and

$$F_2 = B_i^T R^{-1} B_i, \quad F_3 = (I + F_2 S)^{-1}.\tag{4.64}$$

The OCC problem has several different interpretations. In a stochastic point of view, first assume that w_i and v_i are uncorrelated zero-mean white noises with intensity matrices $W_i > 0$ and $V_i > 0$. Let E be the expectation operator and define $E_\infty[\cdot] := \lim_{k \rightarrow \infty} E[\cdot]$, it is easy to see that OCC problem is to minimize $E_\infty[u_i(k) R u_i^T(k)]$ subject to the OCCs $Y_j := E_\infty[y_j(k) y_j^T(k)] < \bar{Y}_j$, $j = 1, 2$. These constraints may be interpreted as constraints on the variance of the performance variables or lower bounds on the residence time of the performance variables [43].

In a deterministic point of view, first define ℓ_∞ and ℓ_2 norms as follows

$$\begin{aligned} \|y_j\|_\infty^2 &:= \sup_{k \geq 0} y_j^T(k) y_j(k) \\ \|w\|_2^2 &:= \sum_{k=0}^{\infty} w^T(k) w(k) \end{aligned}, \quad (4.65)$$

and the ℓ_2 disturbance set

$$\mathcal{W} := \left\{ w \in \mathbb{R}^{n_w} \text{ s.t. } \|W^{-1/2} w\|_2^2 \leq 1 \right\}, \quad (4.66)$$

where $W > 0$ is a real symmetric matrix. Then, for any $w \in \mathcal{W}$, the following inequalities hold

$$\begin{aligned} \|y_j\|_\infty^2 &\leq [Y_j], \quad j = 1, 2, \\ \|u_j\|_\infty^2 &\leq [C_u X C_u^T]_{jj}, \quad j = 1, 2. \end{aligned} \quad (4.67)$$

where $[\cdot]_{jj}$ is the j th diagonal entry. Moreover, [44] and [45] show that the above bounds are the least upper bounds that hold for any arbitrary signal $w \in \mathcal{W}$.

In other word, if the control weighting matrix is defined as $R := \text{diag}[r_1, r_2 \dots r_{n_u}]$, where n_u is the dimension of u (in this paper, $n_u = 2$), the OCC problem is to minimize the sum of the worst-case ℓ_∞ norms on the control signals given by

$$J_{OCC} = \sum_{j=1}^{n_u} r_j \left\{ \sup_{w \in \mathcal{W}} \|u_j\|_\infty^2 \right\} \quad (4.68)$$

subject to the constraints on the worst-case ℓ_∞ norms on the performance variables of the form

$$\sup_{w \in \mathcal{W}} \|y_j\|_\infty^2 \leq \bar{Y}_j, \quad j = 1, 2. \quad (4.69)$$

Note that the corresponding cost function of the LQ controller is defined as

$$J = \sum_{k=0}^{\infty} [y_i(k)^T Q y_i(k) + u_i(k)^T R u_i(k)] \quad (4.70)$$

4.4.3 Baseline controllers

To verify the performance of designed controllers, several different baseline controllers were also designed. The first kind of baseline controller is proportional and integral (PI) controller.

$$G_{PI}(z) = K_P + \frac{K_I}{z-1} \quad (4.71)$$

Table 4.1: PI controller parameters

	P Gain	I Gain
Ziegler-Nichols	0.427	0.128
Modified Ziegler-Nichols	0.188	0.090
Tyreus-Luyben	0.293	0.033

The proportional and integral gains ("P" and "I") of the PI controller are determined by three different methods: Ziegler-Nichols (ZN), Modified Ziegler-Nichols (MZN) and Tyreus-Luyben (TL), see references [46] and [47]. Their values are shown in Table. 4.1. PI controllers use only spark timing, θ_{Spk} , to control the CA50. An OCC baseline controller is also developed only using θ_{Spk} as the controller output. The pre-chamber fuel and air injection amounts are determined by the feedforward controller.

4.5 Experimental Validation

4.5.1 Model validation

Experiments were conducted using the single cylinder DM-TJI engine described in Section II. A TMAP (temperature and manifold air pressure) sensor is mounted in the intake manifold to measure the pressure and temperature. Two Kistler pressure sensors are used to measure the main-chamber and exhaust manifold pressures. Another Kistler pressure sensor integrated with the spark plug is used to measure the pre-chamber pressure; see Fig. 3.1. The exhaust λ is obtained by an ECM lambda meter, and the CA50 is calculated by the combustion analysis system from A&D technology in real time. The experimental data used to calibrate and validate the model are shown in Fig. 4.4. The engine speed ranges from 1200 to 2000 rpm; and IMEP (indicated mean value pressure) ranges from 4.5 to 7.2 bar. The pre-chamber fuel injection amount varies from 0.7 to 1.35 mg.

Direct measurement of the four states in the state-space model is not possible on the TJI engine. In the authors' previous research, [48] and [49], a crank-angle-resolved (CAR) TJI engine model was developed. It is able to calculate all the relevant parameters for every crank angle degree.

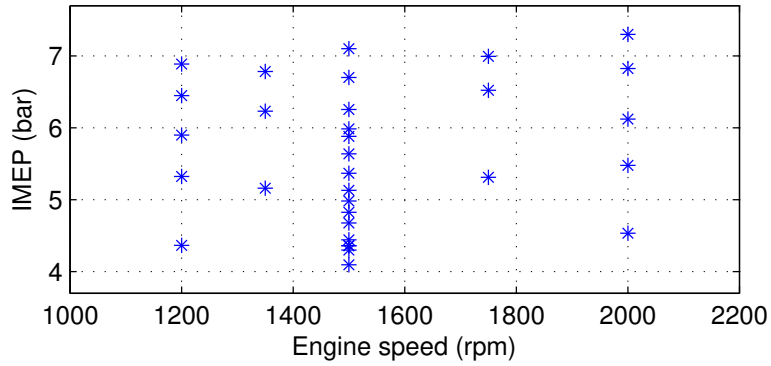


Figure 4.4: Experimental matrix.

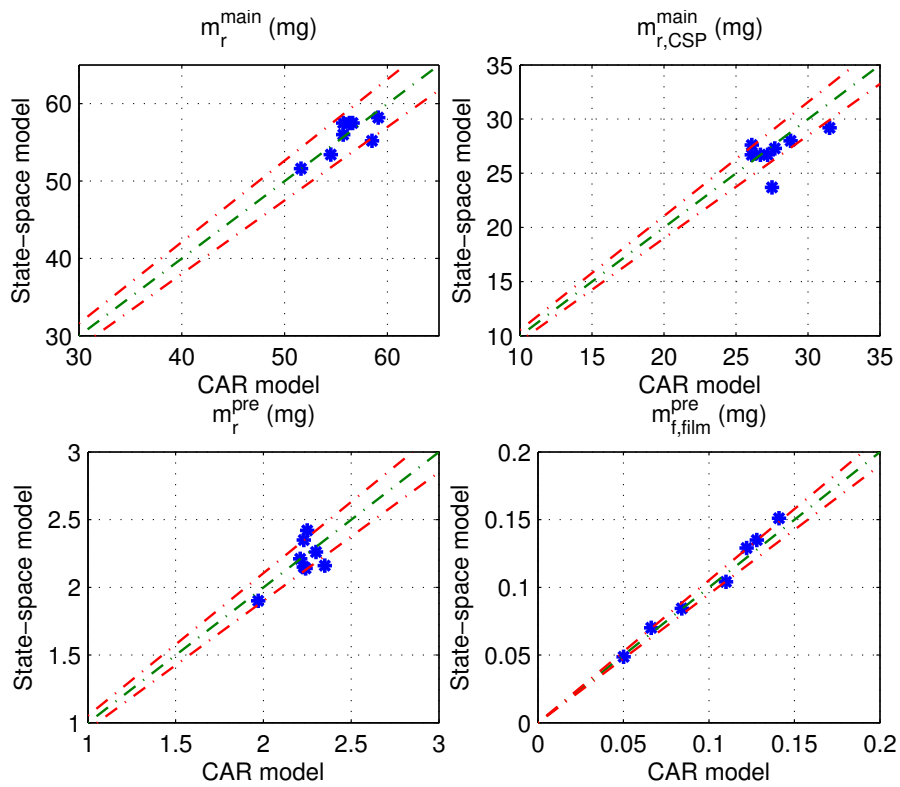


Figure 4.5: State-space engine model validation.

Since the CAR engine model was calibrated and validated by the experimental data under different steady-state operational conditions, the state-space model can be validated by the simulation results of the CAR engine model. The simulation results are shown in Fig. 4.5.

Fig. 4.5 compares the values of the four states calculated from the state-space engine model and those from the CAR engine model at different operational conditions. The two dash-dot lines

on each side of the data points show the 5% error bound. All of the four states calculated by the state-space model match the CAR model very well.

The calculated CA50 values are compared with the experiment results in Fig. 4.6. This figure also shows how CA50 is influenced by different variables. The upper-left plot compares the experimental and calculated CA50 under five different operational conditions. These conditions differ from each other mainly by their main-chamber λ . The other parameters, P_{Int} , Ω , x_{CSP}^{main} , and m_{tur} in Eqn. (4.33) remain unchanged or within small variations. The upper-right and bottom-left plots are obtained similarly by mainly changing P_{Int} and m_{tur} , respectively. However, varying one parameter while maintaining other parameters unchanged is challenging during the experiment. For example, all the parameters, except Ω , will be changed when changing P_{Int} . This is why the simulation points cannot form a straight line in the upper-right plot. However, the trend of the curve is evident: increasing P_{Int} leads to reduced burn duration. The last plot compares CA50 values for all the experimental conditions. The dash-dot line shows the 10% error bound.

Fig. 4.7 shows the CA50 values when the pre-chamber fuel injection amount changes from 1.9 mg to 1.1 mg. The experimental CA50 data have a lot of noise, so it is hard to see the transient response of CA50 from a single set of experimental data. Therefore, the experimental data in Fig. 4.7 are obtained by averaging the results of 14 identical experiments. It can be seen that the CA50 does not reach its steady-state value immediately after reducing the pre-chamber fuel injection. This is caused by the fuel vaporization from the fuel film on the pre-chamber wall.

4.5.2 Controller validation

In the experiment, the controller is implemented into the MotoTron controller shown in Fig. 4.8. The pressure and other signals from the engine are captured by the Phoenix AM module from A&D Technology. The Phoenix RT module calculates the CA50 in real-time and sends it to MotoTron controller through the CAN bus.

Fig. 4.9 compares the experimental results when the controller is turned on and off. When the OCC controller is turned on, CA50 is adjusted close to the optimal value. The standard deviation

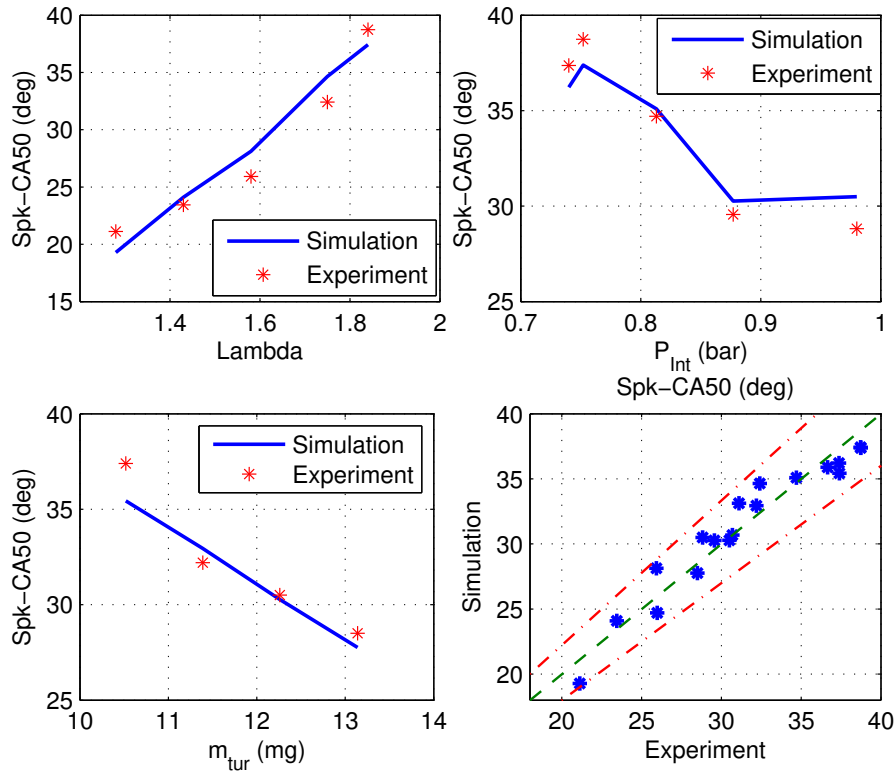


Figure 4.6: Comparison between experimental and calculated CA50 under different operational conditions.

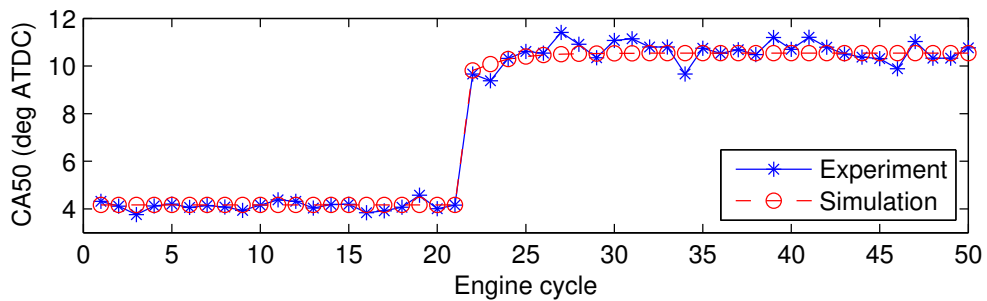


Figure 4.7: Comparison between experimental and calculated CA50 when pre-chamber fuel is changed.

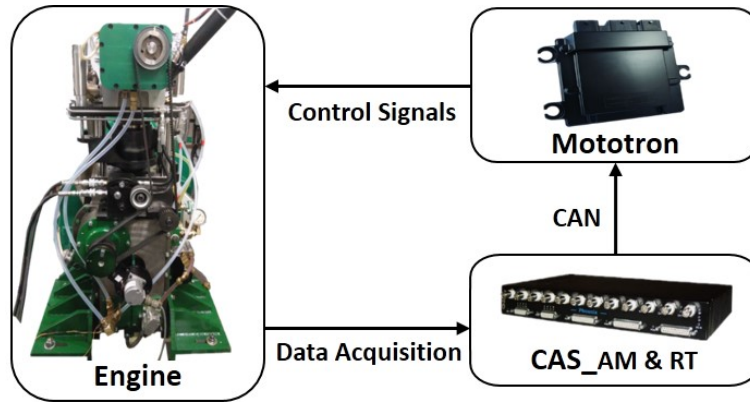


Figure 4.8: Test bench structure.

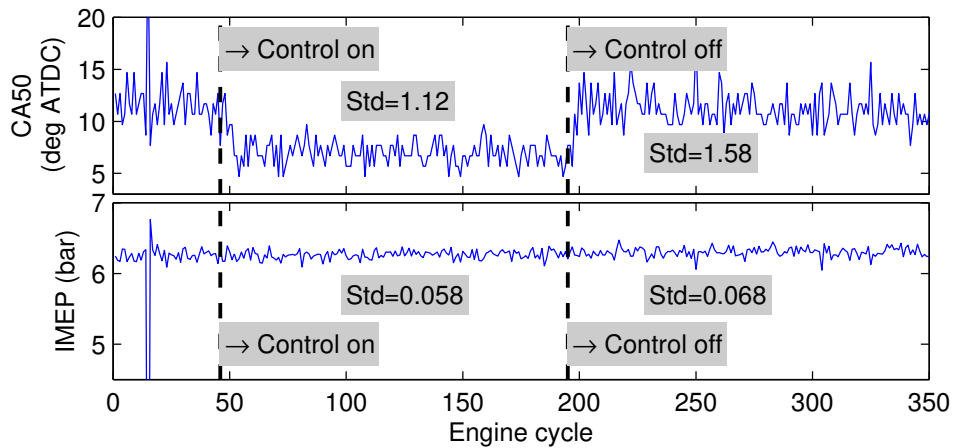


Figure 4.9: Experimental results with controller on and off.

(S.D.) of CA50 is reduced from 1.58 to 1.12 deg after the controller is turned on. The S.D. of IMEP is also reduced accordingly. This indicates that the combustion phasing controller is able to improve the combustion stability by regulating the CA50 close to its optimal value.

The OCC controller is compared with the PI baseline controllers in Fig. 4.10. The settling times for the MZN and TL PI controllers are very long compared with the OCC controller. Since the ZN controller has higher PI gains than these of MZN and TL controllers, the settling time is improved. However, The high gain results in large steady state CA50 variations. This is because the PI controller is not model-based and does not consider the engine cycle-to-cycle dynamics, disturbances and measurement noises. However, OCC controller utilizes all the plant information, and thus, has better performance.

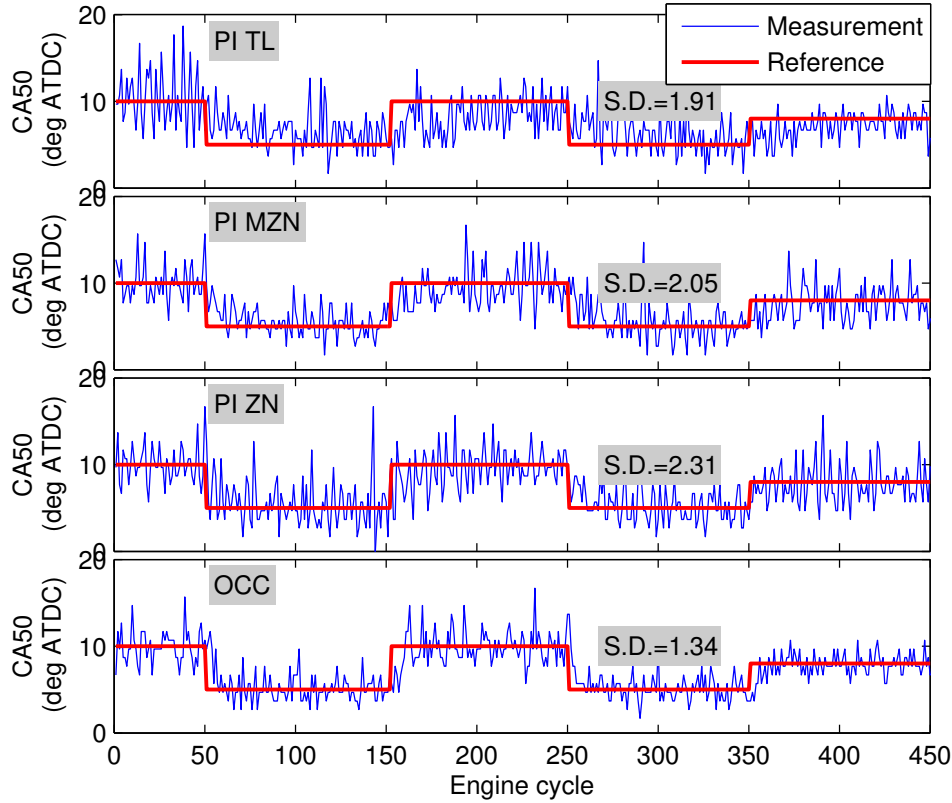


Figure 4.10: Experimental results of OCC and PI controllers.

In Fig. 4.11, the OCC controller is compared with the OCC baseline controller, which does not use pre-chamber fuel injection amount, $m_{inj,fuel}^{pre}$, as the control input. The CA50 takes a longer time to track the desired value. Although it takes a similar number of engine cycles to track the desired CA50 for both cases, the combustion is less stable when only using spark timing as the control input, which can be observed from the standard deviation of CA50 in Fig. 4.11. The reason is quite obvious. Since $m_{inj,fuel}^{pre}$ is not used for closed loop control, the controller relies only on adjusting spark timing to track the desired CA50. This is why the variation of spark timing of the baseline OCC controller is much larger than the proposed OCC controller; see the bottom plot in Fig. 4.11. To achieve similar settling time, the baseline OCC controller needs a larger controller gain than the proposed OCC controller, resulting in significant CA50 variations. It should also be noted that the OCC baseline controller has better performance than other PI controllers. This further demonstrates the benefit of using the model-based OCC control scheme.

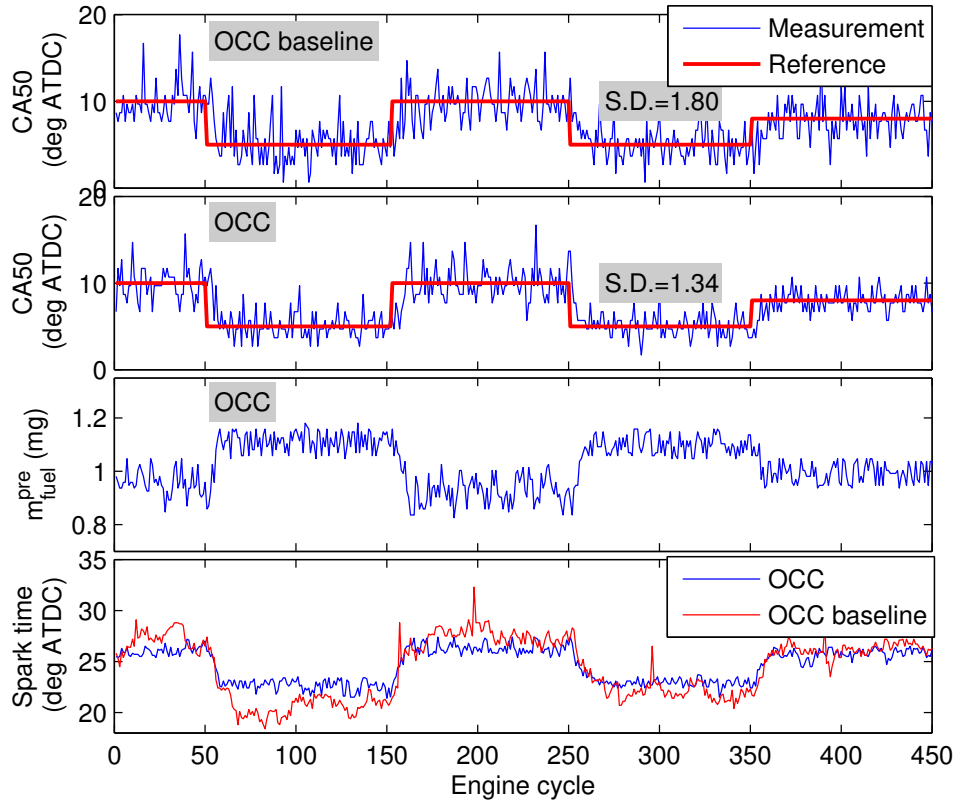


Figure 4.11: Experimental results of OCC controllers with and without using pre-chamber fuel.

Finally, Fig. 4.12 shows the experiment results under different operational conditions (engine speed: 1200 and 2000 rpm; IMEP: 6.5 and 4.55 bar). Overall, the OCC controller is able to track the desired CA50 within 10 engine cycles. Fig. 4.13 compared the standard deviations of the CA50 with different controllers discussed in this paper. The proposed and baseline OCC controllers have overall lower S.D. values than the PID controllers. The proposed OCC controller has much lower value than the baseline OCC controller because of utilization of pre-chamber fuel as a control input.

4.6 Conclusions

In this chapter, a cycle-by-cycle state-space TJI engine model is first developed and validated using both experimental data and high fidelity model. The validation results show that the CA50 (crank location when 50% fuel is burned) modeling error is less than 10%. An OCC (output co-

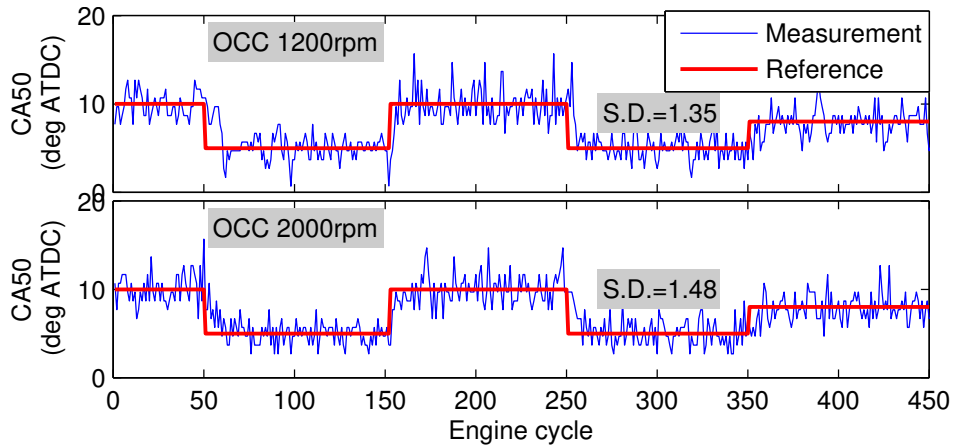


Figure 4.12: Experimental results of OCC controllers under different conditions.

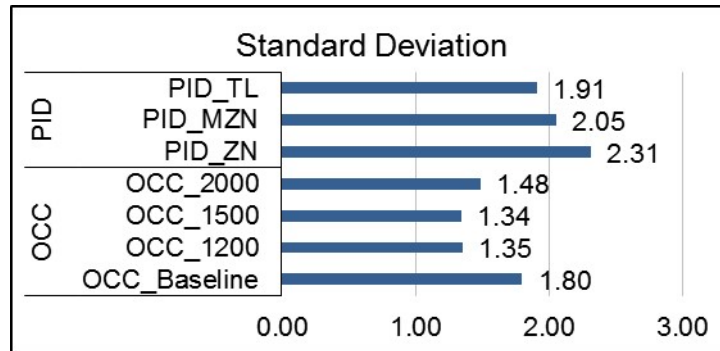


Figure 4.13: Standard deviation of CA50 with different controllers.

variance constraint) combustion phasing controller is developed based on the statespace engine model. The controller uses both spark timing and pre-chamber fuel quantity as the control inputs. Experimental results show that the proposed OCC controller has better performance than the baseline controllers with a minimal improvement of over 22% for CA50 standard deviation. This demonstrates that utilizing multiple pre-chamber control variables and OCC control scheme is able to improve the combustion phasing control performance. The future work is to study if further performance improvement can be achieved by utilizing linear-parameter-varying (LPV) control based on an LPV model that captures the engine dynamics accurately.

CHAPTER 5

CONCLUSIONS AND FUTURE WORK

5.1 Conclusions

In this dissertation, a control-oriented TJI combustion model is firstly developed for a rapid compression machine (RCM) configured for TJI combustion, and then, the RCM model was extended to a TJI combustion model for the Dual-Mode (DM) TJI engine at Michigan State University. To achieve stable combustion with high thermal efficiency and low engine-out emissions, an optimal combustion phasing controller is developed for the DM-TJI engine. The conclusions are summarized as follows.

- A newly proposed parameter-varying Wiebe combustion model is used to link the combustion processes in both pre- and main-combustion chambers. The developed model can be calibrated using a simple and systematic calibration procedure based on the experimental data. The model validation process shows a good agreement between the model and experimental pressure traces, which indicates that the developed model is capable of accurately capturing the TJI combustion dynamics. The validation results also indicate that the model is able to predict the combustion process that is not used to calibrate the model parameters. This shows that the developed model has the potential to be used for studying TJI combustion engines and developing the associated control strategies.
- The TJI engine model was calibrated using experimental data at engine speeds between 1200 and 2000 rpm with indicated mean effective pressure between 4.2 to 7.2 bar, and then, the calibrated model is validated using a set of data different from that used for calibration. The simulation and experimental results show a fairly good agreement. The simulation results also shows the effectiveness of the fuel vaporization model and the combustion model based on the proposed parameter-varying Wiebe function that models the coupling combustion

effect between the pre- and main-chambers. The relative modeling error of the simulated pressure curves is less than 8%. For most of the other pressure related variables, like indicated mean effective pressure and main-chamber burn duration, the relative errors are within 5%.

- The cycle-by-cycle state-space TJI engine model is developed and validated using both experimental data and high fidelity model. The validation results show that the CA50 (crank location when 50% fuel is burned) modeling error is less than 10%. An OCC (output covariance constraint) combustion phasing controller is developed based on the state-space engine model. The controller uses both spark timing and pre-chamber fuel quantity as the control inputs. Experimental results show that the proposed OCC controller has better performance than the baseline controllers with a minimal improvement of over 22% for CA50 standard deviation. This demonstrates that utilizing multiple pre-chamber control variables and OCC control scheme is able to improve the combustion phasing control performance.

5.2 Recommendations for Future Work

Currently, the parameter-varying Wiebe function only uses the mass flow rate of turbulent jets to regulate the main-chamber burn rate. The modeling error increases as operational conditions become far away from the nominal condition. Other properties of the turbulent jet should be studied and used for main-chamber burn rate calculation. Possible properties include: turbulence, temperature, kinetic/internal energy, etc.

In this research, the engine model used for control design is linearized around single operational condition. Although the simulation results under different operational conditions showed similar performance, further study need to be conducted to see if further performance improvement can be achieved by linear-parameter-varying (LPV) control based on LPV model that captures the engine dynamics accurately.

For the current TJI engine, pre-chamber combustion is not optimized through feedback control. In the future, the pre-chamber pressure can be studied and used as the feedback signal. Ionization

signal is another good candidate. It is beneficial to study whether ionization signal could give more information about the pre-chamber combustion and thus used for feedback combustion optimization.

In the future, engine subsystems, such as variable valve timing actuator and supercharger, will be added and the control system will evolve correspondingly. Especially, main-chamber AFR/EGR should be controlled so that maximum dilution rate should be achieved while maintaining a stable combustion.

APPENDICES

APPENDIX A

NONLINEAR STATE-SPACE MODEL

$$m_r^{main}(k+1) = P_{EVC}^{main}(k+1) V_{EVC}^{main} P_{EVC}^{main}(k+1)^{\frac{1}{n}-1} R^{-\frac{1}{n}} V_{EOC}^{main}(k)^{\frac{1}{n}-1} m_{IVC}^{main}(k) \left[\frac{P_{IVC}^{main}(k) V_{IVC}^{main}}{R} \left(\frac{V_{IVC}^{main}}{V_{EOC}^{main}(k)} \right)^{n-1} + \frac{QLHV m_{fuel}^{main}(k)}{C_v} \right]^{-\frac{1}{n}} \quad (A.1)$$

$$m_{r,Ine}^{main}(k+1) = P_{EVC}^{main}(k+1) V_{EVC}^{main} P_{EVC}^{main}(k+1)^{\frac{1}{n}-1} R^{-\frac{1}{n}} V_{EOC}^{main}(k)^{\frac{1}{n}-1} \left[\frac{P_{IVC}^{main}(k) V_{IVC}^{main}}{R} \left(\frac{V_{IVC}^{main}}{V_{EOC}^{main}(k)} \right)^{n-1} + \frac{QLHV m_{fuel}^{main}(k)}{C_v} \right]^{-\frac{1}{n}} \left[m_{r,Ine}^{main}(k) + m_{fuel}^{main}(k) (1 + AFRs) \right] \quad (A.2)$$

$$m_r^{pre}(k+1) = P_{IVC}^{main}(k+1)^{\frac{1}{n}} V^{pre \frac{1}{n}} \left(P_{SPK}^{pre}(k) V^{pre} + \frac{QLHV R}{C_v} m_{fuel,vap}^{pre}(k) \right)^{-\frac{1}{n}} \left\{ m_{inj}^{pre}(k) + m_r^{pre}(k) + \frac{m_{IVC}^{pre}(k)}{V_{SPK}^{main}(k)} \left[V^{pre} - \frac{V_{SPK}^{main}(k)}{V_{IVC}^{main}} V^{pre} - \frac{R}{P_{SPK}^{pre}(k)} \left(m_{inj,fuel}^{pre}(k) T_{inj,fuel}^{pre}(k) + m_{inj,air}^{pre}(k) T_{inj,air}^{pre}(k) \right) \right] \right\} \quad (A.3)$$

$$m_{f,filn}^{pre}(k+1) = \left[m_{f,filn}^{pre}(k+1) + m_{inj,wall}^{pre}(k) \right] \exp \Delta t \left[-\frac{M_f h_{m,ss}}{\delta_f \rho_f} \frac{P_{s0}}{R_m T_f} \exp \left(\frac{\Delta H}{R_m T_f} \right) \right] \quad (A.4)$$

where:

$$m_{IVC}^{main}(k) = m_r^{main}(k) + \frac{P_{IVC}^{main}(k)}{RT_{Int}^{main}(k)} \left[V_{IVC}^{main} - V_{EVC}^{main} \left(\frac{P_{EVC}^{main}(k)}{P_{IVC}^{main}(k)} \right)^{\frac{1}{n}} \right] \quad (A.5)$$

$$V_{EOC}^{main}(k) = f \left[\theta_{SPK} + 0.5 * \Delta \theta_0 \left(\frac{P_{Int}}{P_{Int0}} \right)^a \left(\frac{rpm}{rpm_0} \right)^b \left(\frac{\lambda}{\lambda_0} \right)^c \left(\frac{m_{Ine}}{m_{Ine0}} \right)^d - \beta m_{tur} \right] = f \left[\theta_{SPK} + 0.5 * \Delta \theta_0 \left(\frac{P_{Int}}{P_{Int0}} \right)^a \left(\frac{rpm}{rpm_0} \right)^b \left(\frac{\lambda}{\lambda_0} \right)^c \left(\frac{m_{Ine}}{m_{Ine0}} \right)^d - \beta m_{tur} \right] \quad (A.6)$$

$$\lambda = \frac{m_{IVC}^{main}(k) - m_{fuel}^{main}(k) - m_{r,Ine}^{main}(k)}{m_{fuel}^{main}(k)} = \frac{m_{fresh}^{main}(k) - m_{fuel}^{main}(k) + m_r^{main}(k) - m_{r,Ine}^{main}(k)}{m_{fuel}^{main}(k)} = m_{fuel}^{main}(k)^{-1} \left\{ \frac{P_{IVC}^{main}(k)}{RT_{Int}^{main}(k)} \left[V_{IVC}^{main} - V_{EVC}^{main} \left(\frac{P_{EVC}^{main}(k)}{P_{IVC}^{main}(k)} \right)^{\frac{1}{n}} \right] - m_{fuel}^{main}(k) + m_r^{main}(k) - m_{r,Ine}^{main}(k) \right\} \quad (A.7)$$

$$m_{tur} = \left\{ 1 - P_{EOE}^{pre}(k)^{\frac{1}{n}} V^{pre \frac{1}{n}} \left(P_{SPK}^{pre}(k) V^{pre} + \frac{QLHV R}{C_v} m_{fuel,vap}^{pre}(k) \right)^{-\frac{1}{n}} \right\} \left\{ m_{inj}^{pre}(k) + m_r^{pre}(k) + \frac{m_{IVC}^{pre}(k)}{V_{SPK}^{main}(k)} \left[V^{pre} - \frac{V_{SPK}^{main}(k)}{V_{IVC}^{main}} V^{pre} - \frac{R}{P_{SPK}^{pre}(k)} \left(m_{inj,fuel}^{pre}(k) T_{inj,fuel}^{pre}(k) + m_{inj,air}^{pre}(k) T_{inj,air}^{pre}(k) \right) \right] \right\} \quad (A.8)$$

$$P_{SPK}^{pre}(k) = P_{SPK}^{main}(k) = P_{IVC}^{main}(k) \left(\frac{V_{IVC}^{main}}{V_{SPK}^{main}(k)} \right)^n \quad (A.9)$$

$$T_{IVC}^{pre}(k+1) = R^{-1} P_{IVC}^{main}(k+1)^{1-\frac{1}{n}} V^{pre} 1^{-\frac{1}{n}} \left(P_{SPK}^{pre}(k) V^{pre} + \frac{QLHVR}{C_v} m_{fuel,vap}^{pre}(k) \right)^{\frac{1}{n}} \left\{ m_{inj}^{pre}(k) + m_r^{pre}(k) + \frac{m_{IVC}^{pre}(k)}{V_{SPK}^{main}(k)} \left[V^{pre} - \frac{V_{SPK}^{main}(k)}{V_{IVC}^{main}} V^{pre} - \frac{R}{P_{SPK}^{pre}(k)} \left(m_{inj,fuel}^{pre}(k) T_{inj,fuel}^{pre}(k) + m_{inj,air}^{pre}(k) T_{inj,air}^{pre}(k) \right) \right] \right\}^{-1} \quad (A.10)$$

$$T_{EOC}^{pre}(k) = \left(\frac{P_{SPK}^{pre}(k) V^{pre}}{R} + \frac{QLHV m_{fuel,vap}^{pre}(k)}{C_v} \right) \left\{ m_{inj}^{pre}(k) + m_r^{pre}(k) + \frac{m_{IVC}^{pre}(k)}{V_{SPK}^{main}(k)} \left[V^{pre} - \frac{V_{SPK}^{main}(k)}{V_{IVC}^{main}} V^{pre} - \frac{R}{P_{SPK}^{pre}(k)} \left(m_{inj,fuel}^{pre}(k) T_{inj,fuel}^{pre}(k) + m_{inj,air}^{pre}(k) T_{inj,air}^{pre}(k) \right) \right] \right\}^{-1} \quad (A.11)$$

APPENDIX B

ENGINE MODEL PARAMETERS

Table B.1: Parameters for Combustion Phase Model

Symbol	Eqn.	Value	Symbol	Eqn.	Value
C_1	(4.14)	0.85	b	(4.33)	0.00105 s
OF	(4.14)	1.20 deg/m	c	(4.33)	17 deg
δ_f	(3.14)	0.03 mm	d	(4.33)	-660 deg
a	(4.33)	-60.9 deg/bar	e	(4.33)	-3.06 deg/mg

BIBLIOGRAPHY

BIBLIOGRAPHY

- [1] Lino Guzzella and Christopher Onder. *Introduction to modeling and control of internal combustion engine systems*. Springer Science & Business Media, 2009.
- [2] Benjamin Ellies, Charles Schenk, and Paul Dekraker. Benchmarking and hardware-in-the-loop operation of a 2014 mazda skyactiv 2.0 i 13: 1 compression ratio engine. Technical report, SAE Technical Paper, 2016.
- [3] Reese R. Progress (and challenges) along the path to 2025. In *Engine Research Center 2015 Symposium*. University of Wisconsin, Madison, 2015.
- [4] Timothy Johnson. Vehicular emissions in review. *SAE International Journal of Engines*, 9 (2016-01-0919):1258–1275, 2016.
- [5] Neil Fraser, Hugh Blaxill, Grant Lumsden, and Michael Bassett. Challenges for increased efficiency through gasoline engine downsizing. *SAE International Journal of Engines*, 2 (2009-01-1053):991–1008, 2009.
- [6] Shupeng Zhang, Guoming Zhu, and Zongxuan Sun. A control-oriented charge mixing and two-zone hcci combustion model. *IEEE transactions on vehicular technology*, 63(3):1079–1090, 2014.
- [7] Xiaojian Yang and Guoming Zhu. SI and HCCI combustion mode transition control of an HCCI capable SI engine. *Control Systems Technology, IEEE Transactions on*, 21(5):1558–1569, Sept 2013. ISSN 1063-6536. doi: 10.1109/TCST.2012.2201719.
- [8] Rudolf H Stanglmaier and Charles E Roberts. Homogeneous Charge Compression Ignition (HCCI): Benefits, Compromises, and Future Engine Applications. Technical report, SAE Technical Paper, 1999.
- [9] LA Gussak, Michael C Turkish, and Donald C Siegla. High chemical activity of incomplete combustion products and a method of prechamber torch ignition for avalanche activation of combustion in internal combustion engines. Technical report, SAE Technical Paper, 1975.
- [10] Elisa Toulson, Andrew Huisjen, Xuefei Chen, Cody Squibb, Guoming Zhu, Harold Schock, and William P Attard. Visualization of Propane and Natural Gas Spark Ignition and Turbulent Jet Ignition Combustion. Technical report, SAE Technical Paper, 2012.
- [11] William P Attard, Neil Fraser, Patrick Parsons, and Elisa Toulson. A turbulent jet ignition pre-chamber combustion system for large fuel economy improvements in a modern vehicle powertrain. *SAE International Journal of Engines*, 3(2010-01-1457):20–37, 2010.
- [12] Michael C Turkish. 3-Valve Stratified Charge Engines: Evolvement, Analysis and Progresion. Technical report, SAE Technical Paper, 1974.

- [13] Tasuku Date, Shizuo Yagi, Akira Ishizuya, and Isao Fujii. Research and Development of the Honda CVCC engine. Technical report, SAE Technical Paper, 1974.
- [14] Elisa Toulson, Harold J Schock, and William P Attard. A review of pre-chamber initiated jet ignition combustion systems. Technical report, SAE Technical Paper, 2010.
- [15] Ruitao Song, Gerald Gentz, Guoming Zhu, Elisa Toulson, and Harold Schock. A control-oriented jet ignition combustion model for an si engine. In *ASME 2015 Dynamic Systems and Control Conference*, pages V001T11A001–V001T11A001. American Society of Mechanical Engineers, 2015.
- [16] Elisa Toulson, Harry C Watson, and William P Attard. Modeling alternative prechamber fuels in jet assisted ignition of gasoline and lpg. Technical report, SAE Technical Paper, 2009.
- [17] A Ghorbani, G Steinhilber, D Markus, and U Maas. Numerical investigation of ignition in a transient turbulent jet by means of a pdf method. *Combustion Science and Technology*, 186 (10-11):1582–1596, 2014.
- [18] M. Canova, R. Garcin, S. Midlam-Mohler, Y. Guezennec, and G. Rizzoni. A control-oriented model of combustion process in a hcci diesel engine. In *American Control Conference, 2005. Proceedings of the 2005*, pages 4446–4451 vol. 7, June 2005. doi: 10.1109/ACC.2005.1470696.
- [19] Michael E Mortenson. *Mathematics for computer graphics applications*. Industrial Press Inc., 1999.
- [20] John B Heywood. *Internal combustion engine fundamentals*, volume 930. Mcgraw-hill New York, 1988.
- [21] JI Ghojel. Review of the development and applications of the wiebe function: a tribute to the contribution of ivan wiebe to engine research. *International Journal of Engine Research*, 11 (4):297–312, 2010.
- [22] Hua Zhao and Nicos Ladommatos. Engine combustion instrumentation and diagnostics. *Warrendale, PA: Society of Automotive Engineers, 2001. 842*, 2001.
- [23] Erik Hellström, Anna Stefanopoulou, and Li Jiang. A linear least-squares algorithm for double-wiebe functions applied to spark-assisted compression ignition. *Journal of Engineering for Gas Turbines and Power*, 136(9):091514, 2014.
- [24] Asghar Ghorbani, Gerd Steinhilber, Detlef Markus, and Ulrich Maas. Ignition by transient hot turbulent jets: An investigation of ignition mechanisms by means of a pdf/redim method. *Proceedings of the Combustion Institute*, 35(2):2191–2198, 2015.
- [25] Stephen R Turns et al. *An introduction to combustion*, volume 287. McGraw-hill New York, 1996.
- [26] Yanjun Huang, Amir Khajepour, Tianjun Zhu, and Haitao Ding. A supervisory energy-saving controller for a novel anti-idling system of service vehicles. *IEEE/ASME Transactions on Mechatronics*, 22(2):1037–1046, 2017.

- [27] Ravi Teja Vedula, Ruitao Song, Thomas Stuecken, Guoming G Zhu, and Harold Schock. Thermal efficiency of a dual-mode turbulent jet ignition engine under lean and near-stoichiometric operation. *International Journal of Engine Research*, page 1468087417699979, 2017.
- [28] Nicolas Carpentiers. Turbulent Jet Ignition: In the antechamber of F1 power. <http://en.f1i.com/magazine/76167-tji-antechamber-f1-power.html>, 2016.
- [29] Hui Zhang and Junmin Wang. Adaptive sliding-mode observer design for a selective catalytic reduction system of ground-vehicle diesel engines. *IEEE/ASME Transactions on Mechatronics*, 21(4):2027–2038, 2016.
- [30] Enrico Corti and Claudio Forte. Spark advance real-time optimization based on combustion analysis. *Journal of Engineering for Gas Turbines and Power*, 133(9):092804, 2011.
- [31] Baitao Xiao. Adaptive model based combustion phasing control for multi fuel spark ignition engines. *Proquest Dissertations and Theses*, 2013.
- [32] Peter G Scotson and Peter E Wellstead. Self-tuning optimization of spark ignition automotive engines. *IEEE Control Systems Magazine*, 10(3):94–101, 1990.
- [33] Ibrahim Haskara, Guoming G Zhu, and Jim Winkelman. Multivariable egr/spark timing control for ic engines via extremum seeking. In *American Control Conference, 2006*, pages 6–pp. IEEE, 2006.
- [34] Enrico Corti, Claudio Forte, Giorgio Mancini, and Davide Moro. Automatic combustion phase calibration with extremum seeking approach. *Journal of Engineering for Gas Turbines and Power*, 136(9):091402, 2014.
- [35] Qilun Zhu, Robert Prucka, Shu Wang, Michael Prucka, and Hussein Dourra. Model-based optimal combustion phasing control strategy for spark ignition engines. *SAE International Journal of Engines*, 9(2016-01-0818):1170–1179, 2016.
- [36] Maru Yoon, Kangyoon Lee, and Myoungcho Sunwoo. A method for combustion phasing control using cylinder pressure measurement in a crdi diesel engine. *Mechatronics*, 17(9):469–479, 2007.
- [37] Jinwu Gao, Yuhu Wu, and Tielong Shen. Combustion phase control of si gasoline engines using hypothesis test. *IFAC-PapersOnLine*, 48(15):153–158, 2015.
- [38] Guoming G Zhu, Ibrahim Haskara, and Jim Winkelman. Closed-loop ignition timing control for si engines using ionization current feedback. *IEEE transactions on control systems technology*, 15(3):416–427, 2007.
- [39] Shupeng Zhang, Guoming Zhu, and Zongxuan Sun. A control-oriented charge mixing and two-zone hcci combustion model. *IEEE transactions on vehicular technology*, 63(3):1079–1090, 2014.
- [40] Jonathan W Fox, Wai K Cheng, and John B Heywood. A model for predicting residual gas fraction in spark-ignition engines. Technical report, SAE Technical Paper, 1993.

- [41] Guoming Zhu, MA Rotea, and R Skelton. A convergent algorithm for the output covariance constraint control problem. *SIAM Journal on Control and Optimization*, 35(1):341–361, 1997.
- [42] Xuefei Chen, Yueyun Wang, Ibrahim Haskara, and Guoming Zhu. Optimal air-to-fuel ratio tracking control with adaptive biofuel content estimation for Int regeneration. *IEEE Transactions on Control Systems Technology*, 22(2):428–439, 2014.
- [43] SM Meerkov and T Runolfsson. Output residence time control. *IEEE Transactions on Automatic Control*, 34(11):1171–1176, 1989.
- [44] G Zhu, M Corless, and R Skelton. Robustness properties of covariance controllers. In *Proceedings of Allerton Conference, Monticello, IL*, 1989.
- [45] G Zhu and R Skelton. Mixed l_2 and l_∞ problems by weight selection in quadratic optimal control. *International Journal of Control*, 53(5):1161–1176, 1991.
- [46] Michael L Luyben and William L Luyben. *Essentials of process control*. McGraw-Hill,, 1997.
- [47] Chang C Hang, Karl Johan Åström, and Weng Khuen Ho. Refinements of the ziegler nichols tuning formula. In *IEE Proceedings D Control Theory and Applications*, 1991.
- [48] Ruitao Song, Gerald Gentz, Guoming Zhu, Elisa Toulson, and Harald Schock. A control-oriented model of turbulent jet ignition combustion in a rapid compression machine. *Proceedings of the Institution of Mechanical Engineers, Part D: Journal of Automobile Engineering*, page 0954407016670303, 2016.
- [49] Ruitao Song and Guoming G Zhu. Control-oriented crank-resolved and state-space models for a gasoline turbulent jet ignition engine. In *American Control Conference (ACC), 2017*. IEEE, 2017.